CENTRO DE INVESTIGACIÓN Y DE ESTUDIOS AVANZADOS
DEL INSTITUTO POLITÉCNICO NACIONAL

UNIDAD ZACATENCO
DEPARTAMENTO DE FÍSICA

"Bicapa y monocapa de grafeno en campos magnéticos generados por supersimetría"

Tesis que presenta

Juan Domingo García Muñoz

para obtener el Grado de

Doctor en Ciencias

en la Especialidad de

Física

Directores de tesis: Dr. David José Fernández Cabrera

Ciudad de México Febrero, 2022

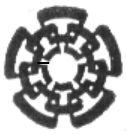

CENTER FOR RESEARCH AND ADVANCED STUDIES OF THE NATIONAL POLYTECHNIC INSTITUTE

PHYSICS DEPARTMENT

"Bilayer and monolayer graphene in magnetic fields generated by supersymmetry"

by

Juan Domingo García Muñoz

In order to obtain the

Doctor of Science

degree, speciality in

Physics

Advisor: Ph. D. David José Fernández Cabrera

Mexico City February, 2022

Agradecimientos

- A mi padre Raúl García Jimenez y a mi madre María Irma Muñoz Magón por otorgarme el don de la vida.
- A mi hija Jimena y a mi compañera de vida Erika por ser la fuente y el soporte de mi vida.
- A toda la familia García y a la familia Vega por cada momento compartido conmigo.
- A las familias Flores y Vicente por su amistad durante tanto tiempo.
- A todas las increíbles personas que he conocido a lo largo de todos estos años en la institución y en el departamento de física, en especial al equipo de baloncesto y a mis compañeros de maestría y doctorado con los que viví grandes momentos.
- A Rosemary y a Mariana que siempre fueron pacientes y me ayudaron mucho en los siempre extenuantes trámites burocráticos.
- A mi asesor David José Fernández Cabrera por sus enseñanzas, consejos y todo el apoyo que me ha brindado sin el cual este trabajo no hubiese sido posible. A Daniel cuya colaboración en la investigación fue de vital importancia.
- Al Departamento de física del CINVESTAV por haberme brindado la oportunidad de realizar mis estudios de doctorado en su seno.
- Al CONACyT por el apoyo económico número 487715 que me fue otorgado durante mis estudios de doctorado y al proyecto FORDECYT-PRONACES/61533/2020.

Contents

List of Figures

Resumen

En la primera parte de esta tesis se resuelve el hamiltoniano efectivo de la bicapa de grafeno interactuando con campos magnéticos ortogonales a la superficie de este material. La mecánica cuántica supersimétrica de segundo orden es usada para transformar el correspondiente problema de valores propios en dos ecuaciones estacionarias unidimensionales de Schrödinger entrelazadas cuyos potenciales se determinan eligiendo una o dos soluciones semilla. Funciones propias analíticas exactas, así como los valores propios de energía asociados son encontrados. Se muestra que para algunos perfiles magnéticos un subconjunto de tales niveles de energía estarán doblemente degenerados. Varios tipos de campos magnéticos son abordados, generados a partir de potenciales socios supersimétricos invariantes y no invariantes de forma. Se muestran las densidades y corrientes de probabilidad para algunos de los estados ligados del hamiltoniano efectivo.

En la segunda parte de esta tesis, asumiendo que un campo magnético complejo es aplicado, el hamiltoniano no hermítico de la monocapa de grafeno es estudiado. En este caso la mecánica cuántica supersimétrica de primer orden se requiere para transformar el problema inicial en un sistema de dos ecuaciones estacionarias unidimensionales de Schrödinger entrelazadas cuyos potenciales socios SUSY complejos invariantes de forma son directamente calculados a través del superpotencial. Soluciones analíticas para los estados ligados son obtenidas para varios perfiles magnéticos y algunas cantidades físicas, como las densidades y corrientes de probabilidad para los primeros estados ligados, son mostradas. Finalmente, una analogía con el grafeno deformado no uniformemente nos permite asociar la parte no hermítica del hamiltoniano con una rotación de *pseudo-spin*. Se formula también una posible interpretación clásica de la naturaleza compleja del campo magnético.

Abstract

In the first part of this thesis the effective Hamiltonian for bilayer graphene interacting with magnetic fields orthogonal to the graphene surface is solved. The second-order supersymmetric quantum mechanics is used to transform the associated eigenvalue problem into two intertwined one-dimensional stationary Schrödinger equations whose potentials are determined by choosing either one or two seed solutions. Exact analytic eigenfunctions and its associated energy eigenvalues are found. It is shown that for some magnetic profiles a subset of such energy levels will be doubly degenerate. Several kinds of magnetic fields are addressed, generated either from shape-invariant or non-shape-invariant supersymmetric partner potentials. The probability and current densities for some bound states of the effective Hamiltonian are shown.

In the second part of this thesis, assuming complex magnetic field is applied, the monolayer graphene non-hermitian Hamiltonian is studied. In this case the first-order supersymmetric quantum mechanics is required to transform the initial problem into a system of two intertwined one-dimensional stationary Schrödinger equations whose complex shape-invariant SUSY partner potentials are directly calculated via the superpotential. Analytic solutions for the bound states are obtained for several magnetic profiles, and some physical quantities as probability and current densities for the first bound states are displayed. Finally, an analogy with the non-uniformly strained graphene allows us to associate the non-hermitian part of the Hamiltonian with a *pseudo-spin* rotation. A possible classical interpretation of the complex nature of the magnetic field is formulated.

Introduction

Life as we know it is based on carbon, whose chemical properties allow the existence of the so-called allotropes; one of such forms of carbon is diamond, that has the highest hardness. Another very important allotrope is the material known as graphene, which is a single layer of carbon atoms arranged in a hexagonal two-dimensional lattice, while many stacked graphene layers form the compound that we call graphite.

The thinness material ever known is graphene, which was isolated for the first time by Geim and Novoselov in 2004 [Novoselov et al., 2004]. In the middle of the 20th century the name graphene was not used, but a few graphene layers were observed in 1948 by Ruess and Vogt [Ruess and Vogt, 1948]. The term graphene was used for the first time by Hanns-Peter Boehm, and then this name reemerged in the literature at the end of the 20th century with the works of Saito, Wang, among others [Saito et al., 1992; Wang et al., 2000]. The theoretical description of graphene was first addressed by Wallace in 1947 [Wallace, 1947]. However, the theory of this material in terms of a massless Dirac equation would be carried out separately by Semenoff and by DiVincenzo and Mele in 1984 [DiVincenzo and Mele, 1984; Semenoff, 1984]. Graphene has a lot of interesting properties, in particular its electronic properties have been widely analysed. For example, the integer quantum Hall effect is due to the existence of the electronic Landau levels at the Dirac point of a graphene layer placed in an external magnetic field [Gusynin and Sharapov, 2005; Novoselov et al., 2005; Zhang et al., 2005]. At low energies this effect indicates the presence of massless chiral quasiparticles with a linear dispersion relation in the case of a single layer, also known as monolayer graphene. In addition, it is possible to have two stacked graphene layers, material which is called bilayer graphene, and the most common arrangement in nature is the AB form or Bernal staking [Katsnelson, 2011]. For bilayer graphene the chiral quasiparticles are massive, with a parabolic dispersion relation, and its description is not ruled by the Dirac-Weyl equation (as in monolayer) but rather by an equation of second degree in the momentum.

The task of finding solutions to the equations describing the monolayer and bilayer graphene is not easy, but in the free case there exist exact analytic solutions[McCann and Koshino, 2013]. Moreover, an important paper supplying this kind of solutions for monolayer graphene interacting with external magnetic fields is [Kuru et al., 2009]. In that work the key idea is to use the first-order supersymmetric quantum mechanics (SUSY QM) to transform the eigenvalue problem for the Dirac-Weyl Hamiltonian describing the monolayer graphene in the magnetic field into two intertwined one-dimensional stationary Schrödinger equations whose potentials are shape-invariant.

Let us note that supersymetric quantum mechanics (SUSY QM) is a technique that intertwines two Hamiltonians by means of a differential operator. This method has natural links with Darboux transformation and factorization method [Andrianov et al., 1984; Nieto, 1984; Sukumar, 1985;

Sukumar, 1985a,b, 1986, 1987]. The latter is an algebraic technique designed to deal with exactly solvable potentials in non-relativistic quantum mechanics. Dirac was the first person who worked out on this technique [Dirac, 1958]. Later on, Schrödinger addressed the subject for different physical systems [Schrödinger, 1940, 1941]. Subsequently, Infeld and Hull gave a wide classification of the potentials which are solvable through factorization [Infeld and Hull, 1951], and Witten introduced the idea of isospectral pairs or supersymmetric partners [Witten, 1981]. It is worth noting Mielnik's contribution, who generalized the standard factorization of the harmonic oscillator to find more general supersymmetric partners of this potential for a given factorization energy [Mielnik, 1984]. The SUSY QM algorithm has been successfully applied to many quantum systems; a collection of different works on the subject can be seen in [Aref'eva et al., 2004]. It is important to mention that nowadays this algorithm is of common use to address solvable potentials and to obtain new supersymmetric partners, as well as the corresponding eigenfunctions. In particular, we are going to apply the first and the second-order supersymmetric quantum mechanics, which have been thoroughly studied in [Fernandez and Fernandez-Garcia, 2005].

In this thesis we will use in the first place the second-order SUSY QM to find exact analytic solutions for the effective Hamiltonian of an electron in bilayer graphene placed in external magnetic fields. Since this method depends on the choice of two parameters, the so-called factorization energies, we have a wide range of possibilities. We limit ourselves to select them as the energy levels of an auxiliary solvable initial Hamiltonian, then we get its corresponding SUSY partner, the eigenvectors and eigenvalues of the original problem and the associated magnetic profile. Analogously, through the first-order SUSY QM we will work the effective Hamiltonian for monolayer graphene but considering a complex magnetic field, whose nature is supposed to be non-physical. However, in the literature examples of complex quantities can be found that at first glance do not seem to be physical but at the end, its real and imaginary parts acquire some physical interpretation, such as complex refractive indexes [Hecht, 2002; Wang et al., 2008], Lee-Yang zeros [Peng et al., 2015], among others. Thus, we will try to give an interpretation of the complex magnetic field based on an analogy with the non-uniformly strained graphene.

In order to carry out the aforementioned work, this thesis is divided in six chapters: in the first one a brief overview of graphene theory is given, in particular the process for deriving the effective Hamiltonians that describes the monolayer and bilayer graphene and the modifications induced by a magnetic field orthogonal to the graphene surface; in the second chapter, the first and second-order supersymmetric quantum mechanics are described, and some examples of this algorithm applied to the harmonic oscillator are shown; in the third chapter, we apply the second-order SUSY QM to the effective Hamiltonian for bilayer, getting the auxiliary shape-invariant potentials, and three specific examples are addressed: the shifted harmonic oscillator, the trigonometric Rosen-Morse potential and the Eckart potential; chapter four deals with a first approximation to non-shape-invariant potentials that results of applying the SUSY algorithm to bilayer graphene, and two examples (the oscillator and the trigonometric Rose-Morse potential) are explored; in chapter five we continue the analysis of non-shape-invariant potentials but employing the so-called confluent algorithm of SUSY QM once again to the harmonic oscillator and the trigonometric Rosen-Morse potential; finally, in chapter six we develop the first-order supersymmetric quantum mechanics by assuming that the SUSY partner potentials are complex. Then this technique is used to find solutions for monolayer graphene in a complex magnetic field and three examples are worked: constant magnetic field, trigonometric singular well and exponentially decaying field. This thesis ends up with our conclusions and the future outlook of this research line.

Chapter 1

A brief overview of graphene

The most spread image of graphene is what we call monolayer graphene, i.e., a two dimensional hexagonal lattice of carbon atoms, see Figure 1.1. This hexagonal lattice is divided into two triangular sublattices, A and B, such that an atom in the sublattice A is surrounded by three atoms from sublattice B and vice versa [Katsnelson, 2011]. The distance to these nearest-neighbours is given by the norm of the following three vectors (see Figure 1.2)

$$\boldsymbol{\delta}_1 = \frac{a}{2}\left(\frac{1}{\sqrt{3}}, 1\right),\ \boldsymbol{\delta}_2 = \frac{a}{2}\left(\frac{1}{\sqrt{3}}, -1\right),\ \boldsymbol{\delta}_3 = a\left(-\frac{1}{\sqrt{3}}, 0\right). \tag{1.1}$$

A conventional unit cell is generated by the primitive lattice vectors

$$\mathbf{a}_1 = \frac{a}{2}(\sqrt{3}, 1),\ \ \mathbf{a}_2 = \frac{a}{2}(\sqrt{3}, -1), \tag{1.2}$$

where $a \approx 2.46$ Å is the distance between two adjacent unit cells. Note that a is different from the length between adjacent carbon atoms $a_l = a/\sqrt{3} \approx 1.42$ Å[McCann and Koshino, 2013]. In the study of crystal structures the reciprocal lattice plays an important role, and graphene is not the exception. The reciprocal lattice vectors fulfil

$$\mathbf{a}_1 \cdot \mathbf{b}_1 = \mathbf{a}_2 \cdot \mathbf{b}_2 = 2\pi,\ \ \mathbf{a}_1 \cdot \mathbf{b}_2 = \mathbf{a}_2 \cdot \mathbf{b}_1 = 0, \tag{1.3}$$

thus they are given by

$$\mathbf{b}_1 = \frac{2\pi}{a}\left(\frac{1}{\sqrt{3}}, 1\right),\ \ \mathbf{b}_2 = \frac{2\pi}{a}\left(\frac{1}{\sqrt{3}}, -1\right). \tag{1.4}$$

Section 1.1

Tight-binding model

The tight-binding model provides a way to identify the Hamiltonian $\mathcal{H}$ that describes graphene [Ashcroft and Mermin, 1976; Katsnelson, 2011; McCann and Koshino, 2013; Raza, 2012; Saito et al., 1998]. The main idea is to find the matrix elements of $\mathcal{H}$ from the Bloch functions $\phi(\mathbf{k}, \mathbf{r})$, with $\mathbf{k}$ being the wave vector and $\mathbf{r}$ the vector position.

Let us begin by introducing some important concepts. A unit cell is invariant under translations of the primitive lattice vectors, in the sense that another unit cell in the lattice is achieved from the vectors $\mathbf{a}_1'$ and $\mathbf{a}_2'$ which are expressed in terms of $\mathbf{a}_1$ and $\mathbf{a}_2$ in the form

$$\mathbf{a}_j' = n_{j1}\mathbf{a}_1 + n_{j2}\mathbf{a}_2, \quad j = 1, 2, \tag{1.1.1}$$

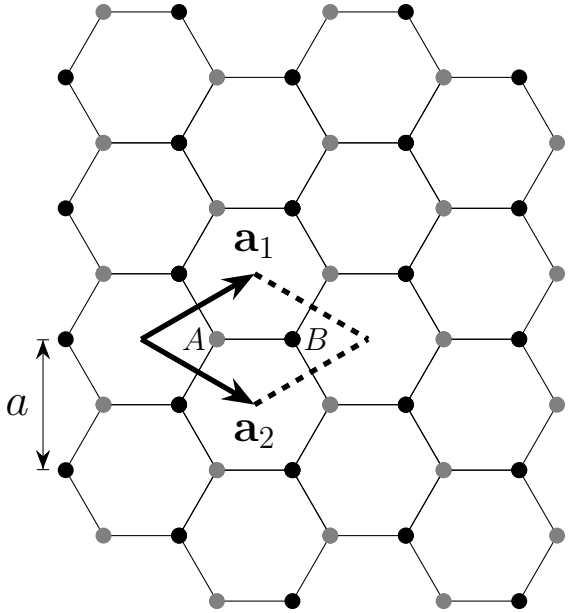

Figure 1.1: Lattice structure of monolayer graphene. The atoms in sublattices A and B are represented as gray and black circles, respectively. The lattice constant a, the primitive lattice vectors $\mathbf{a}_1$ and $\mathbf{a}_2$, as well as the associated unit cell are drawn.

where n_{ij} are integers [Ashcroft and Mermin, 1976]. This implies that there are graphene wave functions ϕ having to fulfil the same translational symmetry. Mathematically speaking, the previous condition is contained in the Bloch theorem

$$T_{\mathbf{a}_j}\phi = e^{i\mathbf{k}\cdot\mathbf{a}_j}\phi. \tag{1.1.2}$$

Natural solutions of equation (1.1.2) are the plane waves, but concerning numerical calculations, experimental implementation, etcetera, they are difficult to work with since the fact that a generic graphene wave function would be an infinite linear combination of such wave functions. So, instead of plane waves we will work with the so-called Bloch functions

$$\phi(\mathbf{k},\mathbf{r}) = \frac{1}{\sqrt{N}}\sum_{\mathbf{R}}^{N} e^{i\mathbf{k}\cdot\mathbf{R}}\varphi_j(\mathbf{r}-\mathbf{R}), \quad j = 1,2,\ldots,n, \tag{1.1.3}$$

where N is the number of unit cells, $\mathbf{R}$ is the position of an atom and n is the number of orbital wave functions φ_j in an unit cell for fixed $\mathbf{k}$. The Bloch theorem is fulfilled by the functions defined in equation (1.1.3), i.e.,

$$\begin{aligned}\phi(\mathbf{k},\mathbf{r}+\boldsymbol{\rho}) &= \frac{1}{\sqrt{N}}\sum_{\mathbf{R}}^{N} e^{i\mathbf{k}\cdot\mathbf{R}}\varphi_j(\mathbf{r}+\boldsymbol{\rho}-\mathbf{R}) \\ &= \frac{1}{\sqrt{N}}\sum_{\mathbf{R}-\boldsymbol{\rho}}^{N} e^{i\mathbf{k}\cdot\boldsymbol{\rho}}e^{i\mathbf{k}\cdot(\mathbf{R}-\boldsymbol{\rho})}\varphi_j\left(\mathbf{r}-(\mathbf{R}-\boldsymbol{\rho})\right) \\ &= e^{i\mathbf{k}\cdot\boldsymbol{\rho}}\phi_j\left(\mathbf{k},\mathbf{r}\right).\end{aligned} \tag{1.1.4}$$

Therefore, the generic wave functions are linear combinations of the Bloch functions ϕ_j, thus taking the form

$$\Phi_{\mathrm{i}}(\mathbf{k},\mathbf{r}) = \sum_{j=1}^{n} C_{\mathrm{i}j}(\mathbf{k})\phi_j(\mathbf{k},\mathbf{r}), \quad \mathrm{i} = 1,\ldots,n, \tag{1.1.5}$$

with $C_{\mathrm{i}j}$ being coefficients to be determined. According to quantum mechanics, the energy eigenvalues E_j of the operator $\mathcal{H}$ can be calculated as the averages

$$E_j = \frac{\langle \Phi_j|\mathcal{H}|\Phi_j\rangle}{\langle \Phi_j|\Phi_j\rangle}. \tag{1.1.6}$$

Substituting equation (1.1.5) in (1.1.6), it is obtained that

$$E_j = \frac{\sum\limits_{l,m=1}^{n} \overline{C}_{jl}C_{jm}\langle\phi_l|\mathcal{H}|\phi_m\rangle}{\sum\limits_{l,m=1}^{n} \overline{C}_{jl}C_{jm}\langle\phi_l|\phi_m\rangle}, \tag{1.1.7}$$

where $\overline{z}$ denotes the complex conjugate of $z \in \mathbb{C}$. We need to optimize the coefficients $C_{\mathrm{i}j}$ to minimize the energy, i.e., a partial derivative of E_j with respect to $\overline{C}_{jl}$ is taken, which leads to

$$\frac{\partial E_j}{\partial \overline{C}_{jl}} = \frac{1}{\sum\limits_{l,m=1}^{n} \overline{C}_{jl}C_{jm}\langle\phi_l|\phi_m\rangle}\left(\sum_{m=1}^{n} C_{jm}\langle\phi_l|\mathcal{H}|\phi_m\rangle - E_j\sum_{m=1}^{n} C_{jm}\langle\phi_l|\phi_m\rangle\right). \tag{1.1.8}$$

This equation was reached by considering that $\partial\overline{C}_{jl}/\partial\overline{C}_{j,l'} = \delta_{l,l'}$ and taking into account equation (1.1.7). Now, making equation (1.1.8) equal to zero, it can be seen that the factor inside the parentheses must vanish, so that

$$\sum_{m=1}^{n} C_{jm}\langle\phi_l|\mathcal{H}|\phi_m\rangle = E_j\sum_{m=1}^{n} C_{jm}\langle\phi_l|\phi_m\rangle. \tag{1.1.9}$$

Since $\langle\phi_l|\mathcal{H}|\phi_m\rangle$ and $\langle\phi_l|\phi_m\rangle$ are matrix elements, we can define the $(n\times n)$-matrices

$$(\mathcal{H})_{\mathrm{i}j} = \langle\phi_{\mathrm{i}}|\mathcal{H}|\phi_j\rangle, \quad (\mathcal{S})_{\mathrm{i}j} = \langle\phi_{\mathrm{i}}|\phi_j\rangle, \tag{1.1.10}$$

which are called transfer and overlap integral matrices, respectively [Saito et al., 1998]. Then, because the index j is fixed in equation (1.1.9), the coefficients $C_{\mathrm{i}j}$ can be seen as column vectors

$$C_j = \begin{pmatrix} C_{j1} \\ C_{j2} \\ \vdots \\ C_{jn} \end{pmatrix}. \tag{1.1.11}$$

The last two equations allow us to rewrite equation (1.1.9) as follows

$$(\mathcal{H} - E_j\mathcal{S})\,C_j = 0. \tag{1.1.12}$$

It is worth noticing that this equation has a non-trivial solution if the determinant of $\mathcal{H} - E_j\mathcal{S}$ is equal to zero, otherwise there exists the inverse matrix $(\mathcal{H} - E_j\mathcal{S})^{-1}$ which when multiplying equation (1.1.12) leads to $C_j = 0$. Thus, we have arrived to the secular equation

$$\det\left[\mathcal{H} - E_j\mathcal{S}\right] = 0, \tag{1.1.13}$$

whose n solutions are the energy eigenvalues of $\mathcal{H}$. In the next two sections we will show how to determine the matrix elements of equation (1.1.10) and to solve the secular equation for graphene.

Section 1.2

Effective Hamiltonian for monolayer graphene

Observing Figure 1.1 we can see two atoms A and B inside each unit cell. For our purposes the number of orbitals taken into account is one per each atom, i.e., the conduction orbital. In a unit cell there will be two orbitals, thus $n = 2$ and the Bloch functions (1.1.3) reduce to

$$\phi_j(\mathbf{k}, \mathbf{r}) = \frac{1}{\sqrt{N}} \sum_{m=1}^{N} e^{i\mathbf{k}\cdot\mathbf{R}_{j,m}} \varphi_j(\mathbf{r} - \mathbf{R}_{j,m}), \quad j = A, B. \tag{1.2.1}$$

Let us calculate the matrix elements of the (2×2)-matrices $\mathcal{H}$ and $\mathcal{S}$. We begin with the diagonal elements

$$\langle\phi_j|\mathcal{H}|\phi_j\rangle = \frac{1}{N} \sum_{m,l=1}^{N} e^{i\mathbf{k}\cdot\left(\mathbf{R}_{j,l} - \mathbf{R}_{j,m}\right)} \left\langle \varphi_j\left(\mathbf{r} - \mathbf{R}_{j,m}\right) \middle| \mathcal{H} \middle| \varphi_j\left(\mathbf{r} - \mathbf{R}_{j,l}\right) \right\rangle. \tag{1.2.2}$$

In this equation the interaction among the jth-atom in the mth-unit cell and jth-atoms in the lth-unit cells is considered. However, we are using the so-called nearest-neighbour approximation, in other words, only self-interactions are taken into account, since the dominant contribution is due to them [Katsnelson, 2011]. Then, equation (1.2.2) is reduced to

$$\langle\phi_j|\mathcal{H}|\phi_j\rangle \approx \frac{1}{N} \sum_{m=1}^{N} \langle\varphi_j|\mathcal{H}|\varphi_j\rangle. \tag{1.2.3}$$

The average $\langle\varphi_j|\mathcal{H}|\varphi_j\rangle = \epsilon_j$ consists of the atomic energy of the free atom plus any graphene layer potential [Saito et al., 1998], so, the diagonal elements turn out to be

$$(\mathcal{H})_{jj} = \epsilon_j. \tag{1.2.4}$$

On the other hand, the off-diagonal elements $\mathcal{H}_{AB}$ are given by

$$\langle\phi_A|\mathcal{H}|\phi_B\rangle = \frac{1}{N} \sum_{m,l=1}^{N} e^{i\mathbf{k}\cdot\left(\mathbf{R}_{B,l} - \mathbf{R}_{A,m}\right)} \left\langle \varphi_A\left(\mathbf{r} - \mathbf{R}_{A,m}\right) \middle| \mathcal{H} \middle| \varphi_B\left(\mathbf{r} - \mathbf{R}_{B,l}\right) \right\rangle. \tag{1.2.5}$$

The previous equation takes into account interactions among a B-atom in the lth-unit cell and A-atoms in the mth-unit cells, but the principal contributions are due to the three nearest A-atoms, see

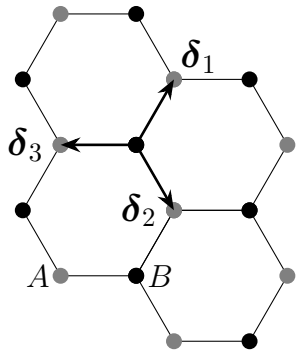

Figure 1.2: The nearest-neighbours for an atom B and its relative position vectors $\boldsymbol{\delta}_l$, whose norms are $|\boldsymbol{\delta}_l| = a_l \approx 1.42$ Å.

Figure 1.2 , whose relative position vectors $\boldsymbol{\delta}_l$ are written in equation (1.1). So, the off-diagonal elements reduce to

$$\begin{aligned}
\langle \phi_A|\mathcal{H}|\phi_B\rangle &\approx \frac{1}{N}\sum_{m=1}^{N}\sum_{l=1}^{3} e^{-i\mathbf{k}\cdot\boldsymbol{\delta}_l}\Big\langle \varphi_A\left(\mathbf{r}-\mathbf{R}_{B,l}-\boldsymbol{\delta}_l\right)\Big|\mathcal{H}\Big|\varphi_B\left(\mathbf{r}-\mathbf{R}_{B,l}\right)\Big\rangle \\
&= \frac{1}{N}\sum_{m=1}^{N}(-\gamma_0)\left[e^{i\frac{ak_x}{\sqrt{3}}}+e^{-i\frac{a}{2}\left(\frac{k_x}{\sqrt{3}}+k_y\right)}+e^{-i\frac{a}{2}\left(\frac{k_x}{\sqrt{3}}-k_y\right)}\right] \\
&= \frac{1}{N}\sum_{m=1}^{N}(-\gamma_0)\left[e^{i\frac{ak_x}{\sqrt{3}}}+2e^{-i\frac{a}{2}\frac{k_x}{\sqrt{3}}}\cos\left(\frac{a}{2}k_y\right)\right] \\
&= -\frac{1}{N}\sum_{m=1}^{N}\gamma_0 h\left(\mathbf{k}\right),
\end{aligned} \tag{1.2.6}$$

with $\gamma_0 = -\Big\langle \varphi_A\left(\mathbf{r}-\mathbf{R}_{\mathrm{B},l}-\boldsymbol{\delta}_l\right)\Big|\mathcal{H}\Big|\varphi_B\left(\mathbf{r}-\mathbf{R}_{B,l}\right)\Big\rangle$ being the so-called in-plane hopping parameter, which is a positive quantity whose negative value is the covalent bond energy between two adjacent carbon atoms. Meanwhile, $h\left(\mathbf{k}\right)$ is the sum of the phase factors $e^{-i\mathbf{k}\cdot\boldsymbol{\delta}_l}$ given by

$$h\left(\mathbf{k}\right) = e^{i\frac{ak_x}{\sqrt{3}}}+2e^{-i\frac{a}{2}\frac{k_x}{\sqrt{3}}}\cos\left(\frac{a}{2}k_y\right). \tag{1.2.7}$$

Therefore, the off-diagonal elements can be written as

$$\left(\mathcal{H}\right)_{AB} = -\gamma_0 h\left(\mathbf{k}\right). \tag{1.2.8}$$

In a similar way, the diagonal elements of $\mathcal{S}$ are

$$\begin{aligned}
\langle \phi_j|\mathcal{S}|\phi_j\rangle &= \frac{1}{N}\sum_{m,l=1}^{N} e^{i\mathbf{k}\cdot\left(\mathbf{R}_{j,l}-\mathbf{R}_{j,m}\right)}\Big\langle \varphi_j\left(\mathbf{r}-\mathbf{R}_{j,m}\right)\Big|\varphi_j\left(\mathbf{r}-\mathbf{R}_{j,l}\right)\Big\rangle \\
&\approx \frac{1}{N}\sum_{m=1}^{N}\langle\varphi_j|\varphi_j\rangle = 1,
\end{aligned} \tag{1.2.9}$$

while the off-diagonal elements become

$$\begin{aligned}\langle\phi_A|\mathcal{S}|\phi_B\rangle &= \frac{1}{N}\sum_{m,l=1}^{N} e^{i\vec{k}\cdot\left(\mathbf{R}_{B,l}-\mathbf{R}_{A,m}\right)}\left\langle\varphi_A\left(\mathbf{r}-\mathbf{R}_{A,m}\right)\middle|\varphi_B\left(\mathbf{r}-\mathbf{R}_{B,l}\right)\right\rangle \\ &\approx \frac{1}{N}\sum_{m=1}^{N}\sum_{l=1}^{3} e^{-i\mathbf{k}\cdot\boldsymbol{\delta}_l}\left\langle\varphi_A\left(\mathbf{r}-\mathbf{R}_{B,l}-\boldsymbol{\delta}_l\right)\middle|\varphi_B\left(\mathbf{r}-\mathbf{R}_{B,l}\right)\right\rangle \\ &= \frac{1}{N}\sum_{m=1}^{N} s_0\left[e^{i\frac{ak_x}{\sqrt{3}}}+2e^{-i\frac{a}{2}\frac{k_x}{\sqrt{3}}}\cos\left(\frac{a}{2}k_y\right)\right] \\ &= \frac{1}{N}\sum_{m=1}^{N} s_0 h\left(\mathbf{k}\right) = s_0 h\left(\mathbf{k}\right).\end{aligned} \tag{1.2.10}$$

The parameter $s_0 = \left\langle\varphi_A\left(\mathbf{r}-\mathbf{R}_{B,l}-\boldsymbol{\delta}_l\right)\middle|\varphi_B\left(\mathbf{r}-\mathbf{R}_{B,l}\right)\right\rangle$ is introduced to consider the possibility of a non-zero overlap between the orbitals of adjacent atoms.

Explicitly, the matrices $\mathcal{H}$ and $\mathcal{S}$ turn out to be

$$\mathcal{H} = \begin{pmatrix}\epsilon_A & -\gamma_0 h\left(\mathbf{k}\right)\\ -\gamma_0\overline{h}\left(\mathbf{k}\right) & \epsilon_B\end{pmatrix}, \quad \mathcal{S} = \begin{pmatrix}1 & s_0 h\left(\mathbf{k}\right)\\ s_0\overline{h}\left(\mathbf{k}\right) & 1\end{pmatrix}. \tag{1.2.11}$$

Now, we can solve the associated secular equation (1.1.13) given by

$$\det\left[\begin{pmatrix}\epsilon_A - E & -\left(\gamma_0 + Es_0\right)h\left(\mathbf{k}\right)\\ -\left(\gamma_0+Es_0\right)\overline{h}\left(\mathbf{k}\right) & \epsilon_B - E\end{pmatrix}\right] = 0. \tag{1.2.12}$$

This leads to a second degree equation for the energy

$$\left(1-s_0^2|h|^2\right)E^2 - \left(\epsilon_A+\epsilon_B+2\gamma_0 s_0|h|^2\right)E + \epsilon_A\epsilon_B - \gamma_0^2|h|^2 = 0, \tag{1.2.13}$$

whose solutions are

$$E_\pm = \frac{\epsilon_A+\epsilon_B+2\gamma_0 s_0|h|^2 \pm \sqrt{\left(\epsilon_A+\epsilon_B\right)^2 - 4\epsilon_A\epsilon_B + 4\left[\gamma_0^2 + s_0^2\epsilon_A\epsilon_B + \gamma_0 s_0\left(\epsilon_A+\epsilon_B\right)\right]|h|^2}}{2\left(1-s_0^2|h|^2\right)}. \tag{1.2.14}$$

Since ϵ_j is the sum of the atomic energy for the free atom plus any graphene layer potential, from now on we can consider them as the same for each carbon atom in the layer, i.e., $\epsilon_A = \epsilon_B = \epsilon$. Hence, the previous solutions reduce to

$$E_\pm = \frac{\epsilon \pm \gamma_0|h(\mathbf{k})|}{1 \mp s_0|h(\mathbf{k})|}. \tag{1.2.15}$$

The monolayer graphene energies $E_\pm$ depend on the wave vector $\mathbf{k}$, hence the importance of the reciprocal space emerges. In this space we can construct the so-called Brillouin zone from the corresponding reciprocal lattice vectors $\mathbf{b}_1$ and $\mathbf{b}_2$ of equation (1.4). Figure 1.3 shows the Brillouin zone for monolayer graphene, which is a hexagon whose vertexes are just the points where $h\left(\mathbf{k}\right)$ vanishes. These are called Dirac points, two of which turn out to be not equivalent (they cannot be

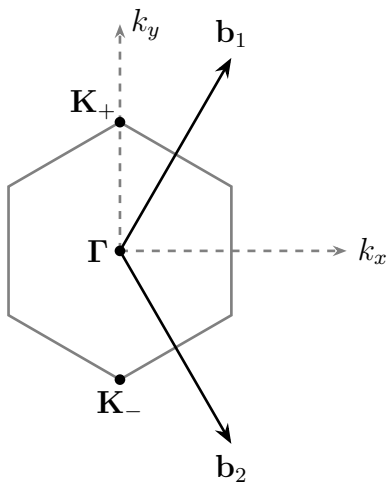

Figure 1.3: Reciprocal space. The Brillouin zone and the reciprocal lattice vectors $\mathbf{b}_1$ and $\mathbf{b}_2$ are shown. Some important points, such as the center $\mathbf{\Gamma}$ and the Dirac points $\mathbf{K}_\pm$, are drawn.

connected through a reciprocal lattice vector) and are labeled as $\mathbf{K}_\pm$. To obtain them all we have to do is to require equation (1.2.7) to be equal to zero. From that, it follows the system of equations

$$\begin{aligned} 1 + 2\cos\left(\frac{\sqrt{3}ak_x}{2}\right)\cos\left(\frac{ak_y}{2}\right) &= 0, \\ -2\sin\left(\frac{\sqrt{3}ak_x}{2}\right)\cos\left(\frac{ak_y}{2}\right) &= 0. \end{aligned} \tag{1.2.16}$$

Then, the components of the vector $\mathbf{k}$ must fulfil the conditions

$$k_x = \frac{2n\pi}{\sqrt{3}a}, \quad k_y = \frac{2}{a}\arccos\left(\frac{(-1)^{n+1}}{2}\right), \quad n \in \mathbb{Z}. \tag{1.2.17}$$

Despite there exist infinite values of k_x and k_y that solve equations (1.2.16), we retain only the solutions for $n = 0, 1$ since their corresponding points in the reciprocal space are the vertexes of the Brillouin zone, but some of them are connected by a reciprocal lattice vector. So, the two non-equivalent Dirac points are $\mathbf{K}_\pm = (0, \pm 4\pi/3a)$.

Intrinsic graphene is the ideal model of this material, with one hundred percent purity and non-stress in the layer. Monolayer, there is not any layer potential and we can think that the orbital energy is the ground energy level, which means to take $\epsilon = 0$. The values of the parameters γ_0 and s_0 often appear in the literature and they can differ depending on the authors; we take the values given by [Saito et al., 1998], namely, $\gamma_0 = 3.033$ eV and $s_0 = 0.129$. If we plot the energy (1.2.15) versus $\mathbf{k}$, in the nearest-neighbour approximation for intrinsic graphene we observe that close to the vertexes of the Brillouin zone the so-called Dirac cones appear, see Figure 1.4. In Figure 1.5 a transversal section of the previous figure is as well displayed. It can be seen that in the neighbourhood of the Dirac points the energy dispersion relation seems to be linear. This suggests to make an approximation around the points $\mathbf{K}_\pm$. Let us take the function $h(\mathbf{k})$ and expand it in

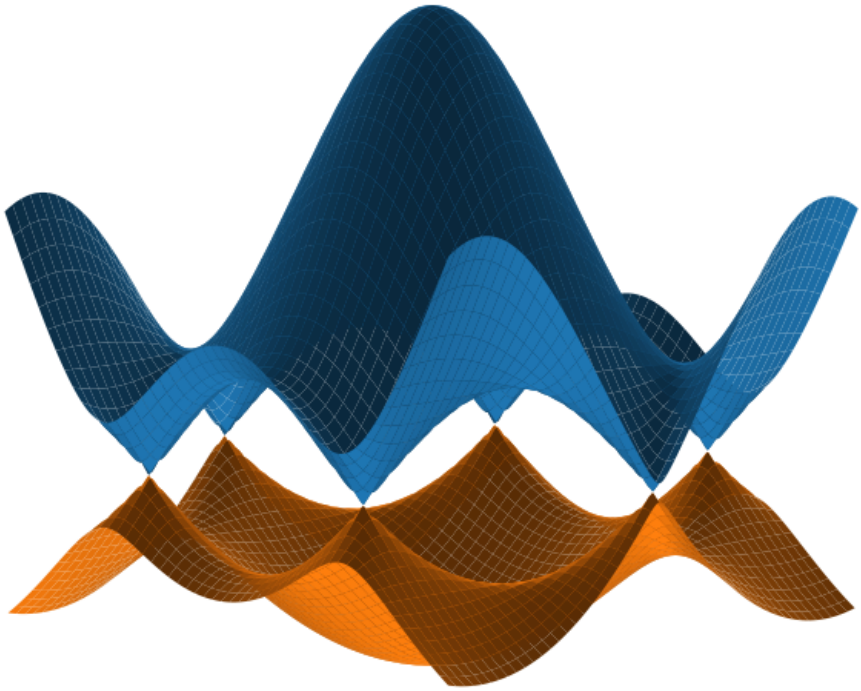

Figure 1.4: Monolayer graphene energies $E_{\pm}$. The Dirac cones are clearly displayed.

powers of $\mathbf{k}$, retaining only linear terms. Thus:

$$h\left(\mathbf{k}\right) \approx \frac{\sqrt{3}a}{2}\left[i\left(k_x - K_{-,x}\right) + \left(k_y - K_{-,y}\right)\right]. \tag{1.2.18}$$

Defining the momentum difference around the Dirac point $\mathbf{K}_-$, $\mathbf{p} = \hbar\left(\mathbf{k} - \mathbf{K}_-\right)$, the function $h\left(\mathbf{k}\right)$ can be written as

$$h\left(\mathbf{k}\right) \approx i\frac{\sqrt{3}a}{2\hbar}\left(p_x - ip_y\right). \tag{1.2.19}$$

Consequently, the matrix $\mathcal{H}$ in equation (1.2.11) acquires the form

$$\mathcal{H} \approx \begin{pmatrix} 0 & -iv_0\pi \\ iv_0\pi^{\dagger} & 0 \end{pmatrix}, \tag{1.2.20}$$

where $\pi = p_x - ip_y$ and $v_0 = \sqrt{3}\gamma_0 a/2\hbar$. The phase factors $e^{\pm i\pi/2}$ in the off-diagonal elements of $\mathcal{H}$ can be removed through a unitary transformation U given by

$$U = \begin{pmatrix} 1 & 0 \\ 0 & i \end{pmatrix}. \tag{1.2.21}$$

Thus, the effective Hamiltonian for monolayer graphene reduces to

$$H_m = v_0 \begin{pmatrix} 0 & \pi \\ \pi^{\dagger} & 0 \end{pmatrix}. \tag{1.2.22}$$

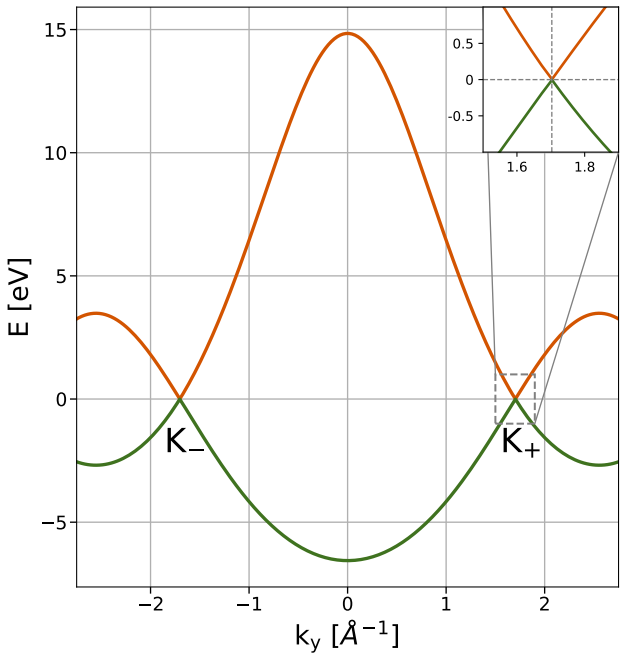

Figure 1.5: Energy spectrum as function of k_y for monolayer graphene. The Dirac points are indicated as $\mathbf{K}_{\pm}$.

It is worth noticing that, due to the low momentum (low energy) approximation, the quantity $s_0\,|h\,(\mathbf{k})|$ is negligible. Thus, the overlap matrix $\mathcal{S}$ in equation (1.2.11) can be replaced by the unit matrix, and the monolayer graphene energies (1.2.15) become

$$E_m = \pm v_0|\mathbf{p}|. \tag{1.2.23}$$

This approximation is valid for energies fulfilling $E \ll \gamma_0$, or equivalently for points in the reciprocal space such that $\sqrt{3}|\mathbf{p}|a/2\hbar \ll 1$. The positive energy is usually associated to electrons and the negative one to holes. Moreover, the linear dependence between the energy and the momentum and the lack of a mass factor means that electrons in monolayer graphene behave as massless chiral particles. We must also point out that if the expansion of $h\,(\mathbf{k})$ is done around the point $\mathbf{K}_+$, it is obtained the transposed matrix of $\mathcal{H}$ in equation (1.2.20), which tells us that the physical results we can get from the effective Hamiltonians derived around the Dirac points $\mathbf{K}_{\pm}$ are equivalent.

Section 1.3

Effective Hamiltonian for bilayer graphene

Bilayer graphene is formed by two coupled monolayers placed one on top of the other, such that the $B1$-atoms in the first layer are underneath the $A2$-atoms of the second layer, see Figure 1.6. The second layer is rotated $60°$ with respect to the first one, the distance between them being

3.48 Å [Razado-Colambo et al., 2018]. This configuration, known as *Bernal stacking*, is the most common in nature. As can be seen in Figure 1.7, the unit cell for bilayer grphene is built from the same primitive lattice vectors $\mathbf{a}_1$ and $\mathbf{a}_2$ of equation (1.2), but this time there are four atoms inside each cell. Then, the number of orbitals per unit cell (considering one orbital per atom) is $n = 4$ such that the integral and overlap matrices are now (4×4). Thus, in the nearest-neighbour approximation the diagonal elements of $\mathcal{H}$ are

$$\langle \phi_j | \mathcal{H} | \phi_j \rangle \approx \frac{1}{N} \sum_{l=1}^{N} \langle \varphi_j | \mathcal{H} | \varphi_j \rangle = \epsilon_j, \tag{1.3.1}$$

where $\epsilon_j = \langle \varphi_j | \mathcal{H} | \varphi_j \rangle$, $j = A1, A2, B1, B2$. Meanwhile, the off-diagonal elements describing the interaction in a same layer can be arranged as

$$\langle \phi_{A2} | \mathcal{H} | \phi_{B2} \rangle = \langle \phi_{A1} | \mathcal{H} | \phi_{B1} \rangle \approx \frac{1}{N} \sum_{m=1}^{N} -\gamma_0 \left[e^{i \frac{a k_x}{\sqrt{3}}} + 2 e^{-i \frac{a}{2} \frac{k_x}{\sqrt{3}}} \cos\left(\frac{a}{2} k_y \right) \right] = -\gamma_0 h(\mathbf{k}) . \tag{1.3.2}$$

On the other hand, the element representing the interaction between the $B1$ and the $A2$-atoms is

$$\langle \phi_{B1} | \mathcal{H} | \phi_{A2} \rangle \approx \frac{1}{N} \sum_{l=1}^{N} e^{i \mathbf{k} \cdot \boldsymbol{\delta}_{BA}} \left\langle \varphi_{B1}(\mathbf{r} - \mathbf{R}_{B1,l}) \middle| \mathcal{H} \middle| \varphi_{A2}(\mathbf{r} - \mathbf{R}_{B1,l} - \boldsymbol{\delta}_{BA}) \right\rangle = \gamma_1, \tag{1.3.3}$$

where we have used that the relative position vector $\boldsymbol{\delta}_{BA}$ is perpendicular to the graphene surface, so that $\mathbf{k} \cdot \boldsymbol{\delta}_{BA} = 0$. We have defined as well the hopping parameter $\gamma_1 = \langle \varphi_{B1} | \mathcal{H} | \varphi_{A2} \rangle$, a positive quantity whose value is 0.381 eV. Physically, the atoms that are exactly one above the other interact through a Van der Waals-like force [Geim and Grigorieva, 2013], with γ_1 being the energy due to this force.

Now, we calculate the matrix element corresponding to the interaction between the $A1$ and the $B2$-atoms. It is important to notice that the relative position vector $\boldsymbol{\delta}_{AB}$ has the in-plane and perpendicular components, but since $\mathbf{k}$ lies in the plane the scalar product $\mathbf{k} \cdot \boldsymbol{\delta}_{AB}$ keeps only the in-plane component of $\boldsymbol{\delta}_{AB}$. Since the distance between two carbon atoms in the graphene molecule is supposed to be fixed, and given the bilayer configuration in the *Bernal stacking*, the in-plane component of $\boldsymbol{\delta}_{AB}$ is the same as one of the in-plane relative position vectors $\boldsymbol{\delta}_l$. As there are three nearest-neighbour $B2$-atoms for each atom $A1$ we get

$$\begin{aligned} \langle \phi_{A1} | \mathcal{H} | \phi_{B2} \rangle &\approx \frac{1}{N} \sum_{m=1}^{N} \sum_{l=1}^{3} e^{i \mathbf{k} \cdot \boldsymbol{\delta}_l} \left\langle \varphi_{A1}(\mathbf{r} - \mathbf{R}_{A1,m}) \middle| \mathcal{H} \middle| \varphi_{B2}(\mathbf{r} - \mathbf{R}_{A1,m} - \boldsymbol{\delta}_{AB}) \right\rangle \\ &= \frac{1}{N} \sum_{m=1}^{N} -\gamma_3 \left[e^{-i \frac{a k_x}{\sqrt{3}}} + 2 e^{i \frac{a}{2} \frac{k_x}{\sqrt{3}}} \cos\left(\frac{a}{2} k_y \right) \right] \\ &= -\gamma_3 \overline{h}(\mathbf{k}) . \end{aligned} \tag{1.3.4}$$

The hopping parameter $\gamma_3 = -\langle \varphi_{A1} | \mathcal{H} | \varphi_{B2} \rangle$ is a weak interaction energy (compared to the covalent bond energy between carbon atoms) with value 0.38 eV [McCann and Koshino, 2013]. Analogously, the relative position vector $\boldsymbol{\delta}_{BB}$ has an in-plane component equal to the negative of

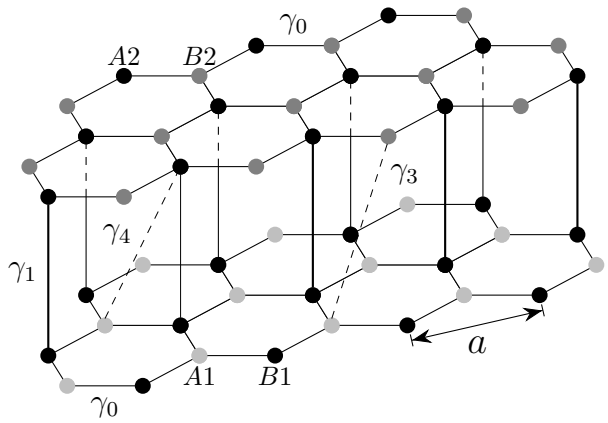

Figure 1.6: Structure of bilayer graphene. The $A2$ and $B2$-atoms are drawn as black and gray circles, respectively, while the $A1$ and $B1$-atoms are the light gray and black circles. It is shown the lattice constant a and the hopping parameters $\gamma_j,\ j = 0, 1, 3, 4$.

a vector $\boldsymbol{\delta}_l$. There are also three nearest-neighbour $B2$-atoms for each atom $B1$, so that

$$\begin{aligned}\langle\phi_{B1}|\mathcal{H}|\phi_{B2}\rangle &\approx \frac{1}{N}\sum_{m=1}^{N}\sum_{l=1}^{3} e^{-i\mathbf{k}\cdot\boldsymbol{\delta}_l}\Big\langle \varphi_{B1}\left(\mathbf{r}-\mathbf{R}_{B1,m}\right)\Big|\mathcal{H}\Big|\varphi_{B2}\left(\mathbf{r}-\mathbf{R}_{B1,m}-\boldsymbol{\delta}_{BB}\right)\Big\rangle \\ &= \frac{1}{N}\sum_{m=1}^{N}\gamma_4\left[e^{i\frac{ak_x}{\sqrt{3}}}+2e^{-i\frac{a}{2}\frac{k_x}{\sqrt{3}}}\cos\left(\frac{a}{2}k_y\right)\right] \\ &= \gamma_4 h\left(\mathbf{k}\right),\end{aligned} \tag{1.3.5}$$

where the hopping parameter $\gamma_4 = \langle\varphi_{B1}|\mathcal{H}|\varphi_{B2}\rangle$ is an interaction energy even smaller than γ_3, since its value is approximately 0.14 eV.

Finally, the vector $\boldsymbol{\delta}_{AA}$ has an in-plane component which is the same as the negative of an in-plane relative position vector $\boldsymbol{\delta}_l$, and there are also three nearest-neighbour $A2$-atoms for each atom $A1$. So, it is obtained that

$$\begin{aligned}\langle\phi_{A1}|\mathcal{H}|\phi_{A2}\rangle &\approx \frac{1}{N}\sum_{m=1}^{N}\sum_{l=1}^{3} e^{-i\mathbf{k}\cdot\boldsymbol{\delta}_l}\Big\langle \varphi_{A1}\left(\mathbf{r}-\mathbf{R}_{A1,m}\right)\Big|\mathcal{H}\Big|\varphi_{A2}\left(\mathbf{r}-\mathbf{R}_{A1,m}-\boldsymbol{\delta}_{AA}\right)\Big\rangle \\ &= \frac{1}{N}\sum_{m=1}^{N}\gamma_4\left[e^{i\frac{ak_x}{\sqrt{3}}}+2e^{-i\frac{a}{2}\frac{k_x}{\sqrt{3}}}\cos\left(\frac{a}{2}k_y\right)\right] \\ &= \gamma_4 h\left(\mathbf{k}\right).\end{aligned} \tag{1.3.6}$$

By collecting all the previous information, the Hamiltonian $\mathcal{H}$ for bilayer graphene becomes

$$\mathcal{H} = \begin{pmatrix} \epsilon_{A1} & -\gamma_0 h\left(\mathbf{k}\right) & \gamma_4 h\left(\mathbf{k}\right) & -\gamma_3\overline{h}\left(\mathbf{k}\right) \\ -\gamma_0\overline{h}\left(\mathbf{k}\right) & \epsilon_{B1} & \gamma_1 & \gamma_4 h\left(\mathbf{k}\right) \\ \gamma_4\overline{h}\left(\mathbf{k}\right) & \gamma_1 & \epsilon_{A2} & -\gamma_0 h\left(\mathbf{k}\right) \\ -\gamma_3 h\left(\mathbf{k}\right) & \gamma_4\overline{h}\left(\mathbf{k}\right) & -\gamma_0\overline{h}\left(\mathbf{k}\right) & \epsilon_{B2} \end{pmatrix}. \tag{1.3.7}$$

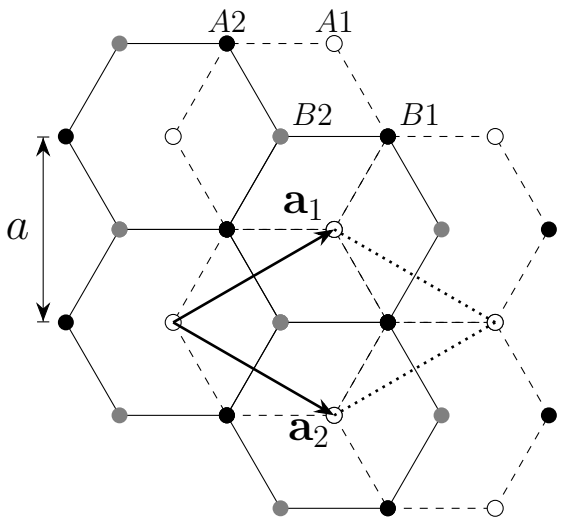

Figure 1.7: Top view of bilayer graphene. The unit cell and the primitive lattice vectors $\mathbf{a}_1$ and $\mathbf{a}_2$ are traced.

The elements of the overlap matrix $\mathcal{S}$ are calculated analogously to the components of the whole matrix $\mathcal{H}$ written above, just changing $\langle\varphi_{\mathrm{i}}|\mathcal{H}|\varphi_j\rangle$ by $\langle\varphi_{\mathrm{i}}|\varphi_j\rangle$ and the corresponding parameters γ_j by s_j. Thus we arrive at

$$\mathcal{S} = \begin{pmatrix} 1 & s_0 h\left(\mathbf{k}\right) & s_4 h\left(\mathbf{k}\right) & s_3 \overline{h}\left(\mathbf{k}\right) \\ s_0 \overline{h}\left(\mathbf{k}\right) & 1 & s_1 & s_4 h\left(\mathbf{k}\right) \\ s_4 \overline{h}\left(\mathbf{k}\right) & s_1 & 1 & s_0 h\left(\mathbf{k}\right) \\ s_3 h\left(\mathbf{k}\right) & s_4 \overline{h}\left(\mathbf{k}\right) & s_0 \overline{h}\left(\mathbf{k}\right) & 1 \end{pmatrix}. \tag{1.3.8}$$

So far we have just applied the nearest-neighbour approximation. Since the unit cell for bilayer graphene has the same primitive lattice vectors as the monolayer, the Brillouin zone is also the same (see Figure 1.3). Therefore, we can focus our attention on the Dirac points $\mathbf{K}_{\pm}$ and implement there the low momentum (low energy) approximation, where the quantities $s_j|h\left(\mathbf{k}\right)|$ are negligible, thus reducing the overlap matrix $\mathcal{S}$ to the (4×4) unit matrix. In Figure 1.8 we can see that close to the points $\mathbf{K}_{\pm}$ the band energies have a quadratic dependence on k_y, as we shall show analytically later on. From the four energy bands two of them do not touch each other, they are separated in the k_y-axis by a gap approximately equal to the hopping parameter γ_1. Such effect is a consequence of the interlayer coupling in the so-called dimer sites $B1$ and $A2$, and in the Hamiltonian (1.3.7) it is described by the matrix elements $(\mathcal{H})_{23}$ and $(\mathcal{H})_{32}$. The other two energy bands touch to each other at the point of zero energy, corresponding to the non-dimer sites $A1$ and $B2$ whose interaction is a low energy process since its associated matrix element $(\mathcal{H})_{14}$ (and the transposed element $(\mathcal{H})_{41}$) provides terms in the graphene energy containing the factor $\gamma_3|h\left(\mathbf{k}\right)| < \gamma_1$. This process is the one occupying our interest, and we shall determine an effective Hamiltonian describing it.

For the purpose of calculating the bilayer graphene energy it is suitable to take the matrix elements of $\mathcal{H}$ which are proportional to γ_3 or γ_4 as zero, and the approximate form of $h\left(\mathbf{k}\right)$ given in equation (1.2.19). These considerations for intrinsic graphene as well as the secular equation

(1.1.13) leads us to four energy bands given by

$$\begin{aligned} E_{\pm}^{(l)} &= \pm\frac{1}{2}\gamma_1\left(1-\sqrt{1+4\frac{v_0^2|\mathbf{p}|^2}{\gamma_1^2}}\right), \\ E_{\pm}^{(h)} &= \pm\frac{1}{2}\gamma_1\left(1+\sqrt{1+4\frac{v_0^2|\mathbf{p}|^2}{\gamma_1^2}}\right). \end{aligned} \tag{1.3.9}$$

As we mentioned before, when $|\mathbf{p}|=0$ the energy bands $E_{\pm}^{(h)}$ are equal to $\pm\gamma_1$ while $E_{\pm}^{(l)}$ vanish, the latter two being the ones corresponding to low energy processes. Considering that $2v_0|\mathbf{p}|/\gamma_1 \ll 1$, the electron energy bands take the form

$$E_b = \pm\frac{v_0^2|\mathbf{p}|^2}{\gamma_1} = \pm\frac{|\mathbf{p}|^2}{2m}, \tag{1.3.10}$$

with the electron effective mass being $m=\gamma_1/2v_0^2$. As it can be seen, the electrons in bilayer graphene behave as massive chiral particles.

On the other hand, if we take only the approximate form of $h\,(\mathbf{k})$, the matrix in equation (1.3.7) can be written as

$$\mathcal{H} = \begin{pmatrix} \epsilon_{A1} & -iv_0\pi & iv_4\pi & iv_3\pi^\dagger \\ iv_0\pi^\dagger & \epsilon_{B1} & \gamma_1 & iv_4\pi \\ -iv_4\pi^\dagger & \gamma_1 & \epsilon_{A2} & -iv_0\pi \\ -iv_3\pi & -iv_4\pi^\dagger & iv_0\pi^\dagger & \epsilon_{B2} \end{pmatrix}, \tag{1.3.11}$$

where we have defined $v_j=\sqrt{3}a\gamma_j/2\hbar$, $j=3,4$. In the same way as for monolayer graphene, it is possible to find a unitary transformation that cancels the phase factor $\pm i$ in the elements of the previous matrix. Its calculation is not hard, but it is tedious and it is not the aim of this work, thus we do not give its explicit expression. Then, the matrix $\mathcal{H}$ we shall work with is

$$\mathcal{H} = \begin{pmatrix} \epsilon_{A1} & v_0\pi & v_4\pi & v_3\pi^\dagger \\ v_0\pi^\dagger & \epsilon_{B1} & \gamma_1 & v_4\pi \\ v_4\pi^\dagger & \gamma_1 & \epsilon_{A2} & v_0\pi \\ v_3\pi & v_4\pi^\dagger & v_0\pi^\dagger & \epsilon_{B2} \end{pmatrix}. \tag{1.3.12}$$

It must be stressed that the previous matrix is written in the basis $A1, B1, A2, B2$. However, it is convenient to express it in the basis of non-dimer and dimer processes $A1, B2, A2, B1$, namely,

$$\mathcal{H} = \begin{pmatrix} h_l & u \\ u^\dagger & h_h \end{pmatrix}, \tag{1.3.13}$$

where the block components are given by

$$h_l = \begin{pmatrix} \epsilon_{A1} & v_3\pi^\dagger \\ v_3\pi & \epsilon_{B2} \end{pmatrix}, \quad h_h = \begin{pmatrix} \epsilon_{A2} & \gamma_1 \\ \gamma_1 & \epsilon_{B1} \end{pmatrix}, \quad u = \begin{pmatrix} v_4\pi & v_0\pi \\ v_0\pi^\dagger & v_4\pi^\dagger \end{pmatrix}. \tag{1.3.14}$$

The block matrix form (1.3.13) leads to an eigenvalue equation whose column eigenvectors are $(\theta_l,\ \theta_h)^T$. Explicitly, we obtain the following system of matrix equations

$$\begin{aligned} h_l\theta_l + u\theta_h &= E\theta_l, \\ u^\dagger\theta_l + h_h\theta_h &= E\theta_h. \end{aligned} \tag{1.3.15}$$

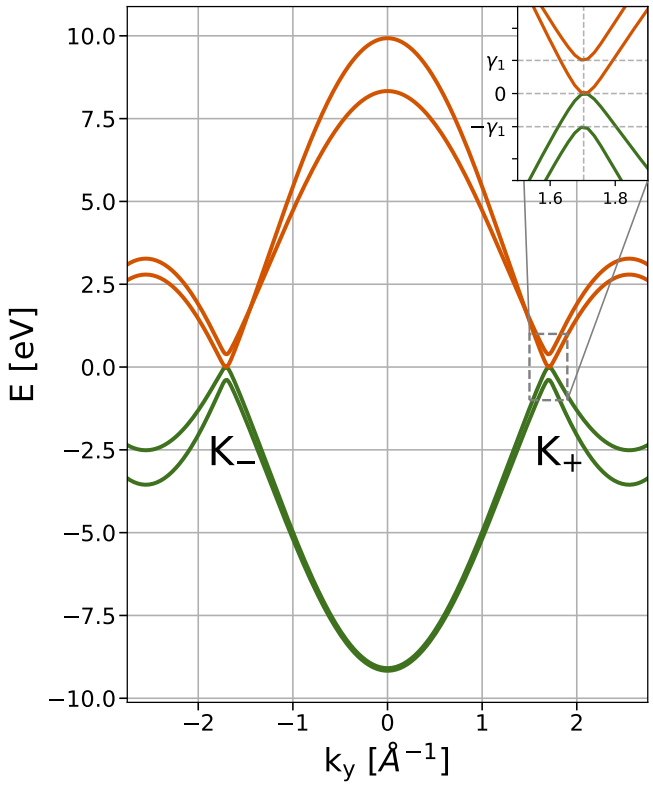

Figure 1.8: Energy bands for intrinsic bilayer graphene as function of k_y. The Dirac points are indicated as $\mathbf{K}_{\pm}$.

From the second row it is possible to express the high energy component θ_h in terms of the low energy one, i.e.,

$$\theta_h = -(h_h - E)^{-1} u^{\dagger} \theta_l, \tag{1.3.16}$$

and substituting this result in the first row of equation (1.3.15) it is obtained

$$\left[h_l - u\left(h_h - E\right)^{-1} u^{\dagger}\right] \theta_l = E\theta_l. \tag{1.3.17}$$

Since we are considering the low energy regime, the matrix $(h_h - E)^{-1}$ can be approximated as follows

$$(h_h - E)^{-1} \approx h_h^{-1} + E h_h^{-2}, \tag{1.3.18}$$

where the notation A^{-2} means that the inverse matrix of A is squared. Thus, equation (1.3.17) can be written in the approximate form

$$\left[h_l - u h_h^{-1} u^{\dagger}\right] \theta_l \approx ET\theta_l, \tag{1.3.19}$$

with $T = 1 + u h_h^{-2} u^{\dagger}$. Because we must ensure the normalization in the eigenvectors, defining $\Theta_l = T^{\frac{1}{2}} \theta_l$ it can be seen that $\Theta_l^{\dagger}\Theta_l = \theta_l^{\dagger} T \theta_l = \theta_l^{\dagger}\left(1 + u h_h^{-2} u^{\dagger}\right)\theta_l$. Thus, the high energy

component is approximately $\theta_h = -h_h^{-1}u^\dagger\theta_l$, and together with the fact that the matrix h_h is hermitian it is gotten that $\Theta_l^\dagger\Theta \approx \theta_l^\dagger\theta_l + \theta_h^\dagger\theta_h$. Therefore, equation (1.3.19) can be written as

$$T^{-\frac{1}{2}}\left[h_l - uh_h^{-1}u^\dagger\right]T^{-\frac{1}{2}}\Theta_l \approx E\Theta_l. \tag{1.3.20}$$

The previous equation means that an effective (2×2) Hamiltonian describing the low energy process in terms of the high energy one can be defined as follows

$$\mathcal{H}_{eff} = T^{-\frac{1}{2}}\left[h_l - uh_h^{-1}u^\dagger\right]T^{-\frac{1}{2}}. \tag{1.3.21}$$

Following the low energy approximation, it turns out that $T^{-\frac{1}{2}} \approx 1 - uh_h^{-2}u^\dagger/2$; recalling that $v_4|\mathbf{p}| < v_3|\mathbf{p}| \ll v_0|\mathbf{p}| \ll \gamma_1$. Hence, if only terms that are linear in the small parameters and quadratic in the momentum are considered, the effective Hamiltonian takes the rough form

$$\begin{aligned}\mathcal{H}_{eff} &\approx v_3\begin{pmatrix}0 & \pi^\dagger\\ \pi & 0\end{pmatrix} - \frac{1}{\gamma_1}\begin{pmatrix}2v_0v_4\pi\pi^\dagger & v_0^2\pi^2\\ v_0^2\left(\pi^\dagger\right)^2 & 2v_0v_4\pi^\dagger\pi\end{pmatrix} + \dots\\ &= -\frac{v_0^2}{\gamma_1}\begin{pmatrix}0 & \pi^2\\ \left(\pi^\dagger\right)^2 & 0\end{pmatrix} + v_3\begin{pmatrix}0 & \pi^\dagger\\ \pi & 0\end{pmatrix} - \frac{2v_0v_4}{\gamma_1}\begin{pmatrix}\pi\pi^\dagger & 0\\ 0 & \pi^\dagger\pi\end{pmatrix} + \dots\end{aligned} \tag{1.3.22}$$

The first term in the previous expansion is similar to the one obtained in the monolayer case, see equation (1.2.22), but being quadratic in the momentum rather than linear. This anti-diagonal matrix describes the low energy hopping between the non-dimer sites $A1$, $B2$ through the hopping from $A1$ to $B1$ (characterized by the in-plane factor $v_0\pi$), then a change of layer from $B1$ to $A2$ (giving the factor $1/\gamma_1$) and finally another in-plane hopping from $A2$ to $B2$. The other terms in the expansion give rise to another phenomena for bilayer graphene, such as the trigonal warping, electron-hole asymmetry and so on [McCann and Koshino, 2013], which for the moment are not of our interest. Therefore, we shall take as the effective Hamiltonian for bilayer graphene the operator matrix

$$H_b = -\frac{1}{2m}\begin{pmatrix}0 & \pi^2\\ \left(\pi^\dagger\right)^2 & 0\end{pmatrix}. \tag{1.3.23}$$

In the next section we shall see how to introduce the effect of a magnetic field applied to monolayer and bilayer graphene using the minimal coupling rule for the Hamiltonians (1.2.22) and (1.3.23).

Section 1.4

Graphene interacting with external magnetic fields

Let us suppose that a magnetic field $\mathbf{B}$ perpendicular to the graphene surface is applied, which varies only in one in-plane direction, e.g., $\mathbf{B}(x) = B(x)\mathbf{e}_z$. Such assumptions are made for simplicity; in fact, for more general magnetic fields applied to monolayer graphene we can recommend [Díaz-Bautista, 2020; Díaz-Bautista et al., 2019; Le et al., 2018]. In agreement with the minimal coupling rule, the magnetic field effect is considered in the Hamiltonian describing the system by adding the term $(e/c)\mathbf{A}$ to the momentum $\mathbf{p}$, where $\mathbf{A}$ is the vector potential associated to $\mathbf{B}$ such that

$$\mathbf{B} = \boldsymbol{\nabla}\times\mathbf{A}. \tag{1.4.1}$$

This equation implies that we can add the gradient of any scalar function to the vector potential $\mathbf{A}$ and the resulting magnetic field remains unchanged, which is called gauge invariance. In particular, here we will choose the Landau gauge which consists in taking the vector potential as $\mathbf{A}(x) = A(x)\mathbf{e}_y$ and thereby

$$B(x) = \frac{dA(x)}{dx}. \tag{1.4.2}$$

Subsection 1.4.1

Monolayer graphene

By applying now the minimal coupling rule to the effective Hamiltonian (1.2.22) for monolayer graphene and recalling that $\pi = p_x - ip_y$ we get

$$H_m = v_0 \begin{pmatrix} 0 & p_x - ip_y - i\frac{e}{c}A(x) \\ p_x + ip_y + i\frac{e}{c}A(x) & 0 \end{pmatrix}. \tag{1.4.3}$$

It is worth noting that this Hamiltonian commutes with the momentum operator p_y along y-direction, because the vector potential amplitude is only a function of x and the momentum operators in different directions commute themselves. This suggests that there is a free motion in y-direction, since the momentum in such direction is a conserved quantity. So, it is natural to propose the next form for the eigenvectors of H_m,

$$\Psi^{(m)}(x,y) = Ne^{iky} \begin{pmatrix} \psi^{(1)}(x) \\ i\psi^{(0)}(x) \end{pmatrix}, \tag{1.4.4}$$

with N being a normalization factor while k is the wavenumber in y-direction. In quantum mechanics the momentum operator in the coordinates representation is written as $p_j = -i\hbar\partial_j$, with $\partial_j = \partial/\partial j,\ j = x, y$. Thus the corresponding eigenvalue equation looks like

$$\begin{aligned} H_m\Psi^{(m)}(x,y) &= \hbar v_0 \begin{pmatrix} 0 & -i\partial_x - ik - i\frac{e}{\hbar c}A(x) \\ -i\partial_x + ik + i\frac{e}{\hbar c}A(x) & 0 \end{pmatrix} \Psi^{(m)}(x,y) \\ &= E_m\Psi^{(m)}(x,y). \end{aligned} \tag{1.4.5}$$

This equation is equivalent to the coupled system of equations

$$\begin{aligned} L_1^-\psi^{(0)}(x) &= \left[\frac{d}{dx} + k + \frac{e}{c\hbar}A(x)\right]\psi^{(0)}(x) = \mathcal{E}_m\psi^{(1)}(x), \\ L_1^+\psi^{(1)}(x) &= \left[-\frac{d}{dx} + k + \frac{e}{c\hbar}A(x)\right]\psi^{(1)}(x) = \mathcal{E}_m\psi^{(0)}(x), \end{aligned} \tag{1.4.6}$$

where $\mathcal{E}_m = E_m/v_0\hbar$. A straightforward way to decouple the previous system is to apply the operator L_1^+ to the first equation and L_1^- to the second equation (1.4.6). This process leads us to two second-order differential operators given by

$$\begin{aligned} L_1^+L_1^- &= \left[-\frac{d}{dx} + k + \frac{e}{c\hbar}A(x)\right]\left[\frac{d}{dx} + k + \frac{e}{c\hbar}A(x)\right] \\ &= -\frac{d^2}{dx^2} + k^2 + \left(\frac{e}{c\hbar}A(x)\right)^2 + 2\frac{ek}{c\hbar}A(x) - \frac{e}{c\hbar}A'(x) \\ &= -\frac{d^2}{dx^2} + \left[k + \frac{e}{c\hbar}A(x)\right]^2 - \frac{e}{c\hbar}A'(x), \end{aligned} \tag{1.4.7}$$

$$\begin{aligned} L_1^- L_1^+ &= \left[\frac{d}{dx} + k + \frac{e}{c\hbar}A(x)\right]\left[-\frac{d}{dx} + k + \frac{e}{c\hbar}A(x)\right] \\ &= -\frac{d^2}{dx^2} + k^2 + \left(\frac{e}{c\hbar}A(x)\right)^2 + 2\frac{ek}{c\hbar}A(x) + \frac{e}{c\hbar}A'(x) \\ &= -\frac{d^2}{dx^2} + \left[k + \frac{e}{c\hbar}A(x)\right]^2 + \frac{e}{c\hbar}A'(x), \end{aligned} \tag{1.4.8}$$

with $A'(x) = dA(x)/dx$. Thus, the next two second-order differential equations must be fulfilled

$$\begin{aligned} L_1^+ L_1^- \psi^{(0)}(x) &= \mathcal{E}_m^2 \psi^{(0)}(x), \\ L_1^- L_1^+ \psi^{(1)}(x) &= \mathcal{E}_m^2 \psi^{(1)}(x). \end{aligned} \tag{1.4.9}$$

It is worth noticing that these equations are similar to the eigenvalue problems for two one-dimensional Schrödinger-like Hamiltonians, provided that $A(x) \in \mathbb{R}$. If we denote H_0 as the product $L_1^+ L_1^-$ and H_1 as $L_1^- L_1^+$, then the corresponding potentials become

$$\begin{aligned} V_0(x) &= \left[k + \frac{e}{c\hbar}A(x)\right]^2 - \frac{e}{c\hbar}A'(x), \\ V_1(x) &= \left[k + \frac{e}{c\hbar}A(x)\right]^2 + \frac{e}{c\hbar}A'(x). \end{aligned} \tag{1.4.10}$$

It must be stressed that, since our Hamiltonians H_j are the product of the operators $L_1^{\pm}$, the following relation must be satisfied

$$H_1 L_1^- = L_1^- H_0. \tag{1.4.11}$$

This equation, called intertwining relation, together with the form for H_0 and H_1 of equations (1.4.7) and (1.4.8), respectively, as well as the expression (1.4.6) for the first-order differential operators $L_1^{\pm}$, constitute the basic ingredients required to implement the first-order supersymmetric quantum mechanics (SUSY QM). We shall discuss SUSY QM in the next chapter, in order to obtain the eigenvalues E_m and eigenvectors $\Psi(x, y)$ of H_m. There are many papers in the literature developing this idea and getting interesting results, see e.g. [Castillo-Celeita and Fernández, 2020; Concha et al., 2018; Díaz-Bautista, 2020; Díaz-Bautista and Fernández, 2017; Díaz-Bautista et al., 2019; Kuru et al., 2009; Le et al., 2018; Midya and Fernández, 2014; Milpas et al., 2011; Schulze-Halberg and Roy, 2017].

As we mentioned previously, the magnetic field $\mathbf{B}(x)$ is supposed to be real. However, mathematically speaking nothing forbids us to assume it is complex. In chapter 6 we shall address this idea and explore its physical meaning, as well as to obtain exact solutions for the associated eigenvalue equation.

Subsection 1.4.2

Bilayer graphene

If we apply now the minimal coupling rule to the effective Hamiltonian (1.3.23) for bilayer graphene, it turns out that

$$H_b = -\frac{1}{2m}\begin{pmatrix} 0 & \left[p_x - ip_y - i\frac{e}{c}A(x)\right]^2 \\ \left[p_x + ip_y + i\frac{e}{c}A(x)\right]^2 & 0 \end{pmatrix}. \tag{1.4.12}$$

Analogously to the monolayer case, the Hamiltonian H_b commutes with the momentum operator p_y, allowing us to propose the corresponding eigenvector as

$$\Psi^{(b)}(x,y) = Ne^{iky}\begin{pmatrix}\psi^{(2)}(x)\\ \psi^{(0)}(x)\end{pmatrix}, \tag{1.4.13}$$

with N being a normalization factor while k is the wavenumber in y-direction. Substituting this expression in the eigenvalue equation for H_b, one gets the following coupled system of equations

$$\begin{aligned} L_2^-\psi^{(0)}(x) &= \left[\frac{d^2}{dx^2} + 2\left(k+\frac{e}{c\hbar}A(x)\right)\frac{d}{dx} + \left(k+\frac{e}{c\hbar}A(x)\right)^2 + \frac{e}{c\hbar}A'(x)\right]\psi^{(0)}(x) = \mathcal{E}_b\psi^{(2)}(x),\\ L_2^+\psi^{(2)}(x) &= \left[\frac{d^2}{dx^2} - 2\left(k+\frac{e}{c\hbar}A(x)\right)\frac{d}{dx} + \left(k+\frac{e}{c\hbar}A(x)\right)^2 - \frac{e}{c\hbar}A'(x)\right]\psi^{(2)}(x) = \mathcal{E}_b\psi^{(0)}(x), \end{aligned} \tag{1.4.14}$$

where $\mathcal{E}_b = 2mE_b/\hbar^2$. It is possible to decouple the previous system by applying L_2^+ on the first equation (1.4.14) and L_2^- on the second one. The result turns out to be similar to equation (1.4.9), which looks like

$$\begin{aligned} L_2^+L_2^-\psi^{(0)}(x) &= \mathcal{E}_b^2\psi^{(0)}(x),\\ L_2^-L_2^+\psi^{(2)}(x) &= \mathcal{E}_b^2\psi^{(2)}(x). \end{aligned} \tag{1.4.15}$$

Unlike the monolayer case, now the products of the operators $L_2^\pm$ of equation (1.4.15) are fourth-order differential operators. Thus, the relation between such products and some one-dimensional Schrödinger-like Hamiltonians is not simple to be established. Nevertheless, let us suppose that there exist such Hamiltonians, denoted as H_0 and H_2, fulfilling an intertwining relation

$$H_2L_2^- = L_2^-H_0. \tag{1.4.16}$$

We shall explain later on how the second-order SUSY QM helps us to determine, using the previous relation, the solutions of the system of equations (1.4.14). It is important to emphasize that the use of this technique allows us to widen our options, in the sense that the operator L_2^- is not necessarily the square of the operator $d/dx+k+(e/c\hbar)A(x)$, but rather the product of two in general different first-order differential operators.

We must mention as well that the auxiliary Schrödinger-like Hamiltonians H_j, $j=0,1,2$, are just mathematical tools, introduced to give a better idea on how to translate the system of equations (1.4.6) and (1.4.14) to the SUSY QM language, hence they do not have physical meaning. For this reason, they should not be confused neither with physical Hamiltonians such as H_m or H_b, which describe an electron in monolayer or bilayer graphene, respectively, nor with those used to study the interactions between an electron and other components of graphene [Schütt et al., 2011]. On the other hand, in this work we are supposing that the magnetic field is externally applied either to the monoloyer or to the bilayer graphene. Although such magnetic profiles could not be entirely realized nowadays in the laboratory, there exist in the literature many papers about experimental implementations of inhomogeneous magnetic fields for systems which are similar to graphene. Some examples of this studies are those carried out through magnetic vortexes [Masir et al., 2011], or performed using magnetic field spectroscopy devices [Schnez et al., 2009] and ferromagnetic stripes [Matulis et al., 1994; Ramezani Masir et al., 2008]. Another point is that, despite graphene immersed in crossed external electric and magnetic fields or deformed by strain are phenomena of different physical nature, however their mathematical description is similar to the one presented here [Castillo-Celeita et al., 2020; Naumis et al., 2017; Oliva-Leyva and Naumis, 2015].

Chapter 2

Supersymmetric Quantum Mechanics

Supersymmetric quantum mechanics (SUSY QM) is a technique whose main goal is to generate new Schrödinger-like Hamiltonians H_j, $j = 1, 2, 3, \ldots$, their corresponding eigenvalues $\mathcal{E}^{(j)}$ and eigenfunctions $\psi^{(j)}(x)$ departing from an initial solvable Hamiltonian H_0 for which we know in advance the eigenvalues $\mathcal{E}^{(0)}$ and eigenfunctions $\psi^{(0)}(x)$ [Fernandez and Fernandez-Garcia, 2005]. This is reached by assuming that the two Hamiltonians H_0, H_j are intertwined through the jth-order differential operators $L_j^{\pm}$, therefrom the technique is usually called jth-order SUSY QM. In the next two sections we shall develop such a method but limit the discussion to the cases with $j = 1, 2$, which will be useful to deal with the problem of an electron in monolayer or bilayer graphene interacting with external magnetic fields.

Section 2.1

First-order supersymmetric quantum mechanics

Let us begin by considering two one-dimensional Schrödinger-like Hamiltonians

$$H_j = -\frac{d^2}{dx^2} + V_j(x), \quad j = 0, 1, \tag{2.1.1}$$

which are intertwined as follows

$$H_1 L_1^- = L_1^- H_0. \tag{2.1.2}$$

The first-order differential intertwining operator L_1^- is given by

$$L_1^- = \frac{d}{dx} + \mathrm{w}(x), \tag{2.1.3}$$

where the so-called superpotential $\mathrm{w}(x)$ is a real function to be determined. The constraint that the superpotential $\mathrm{w}(x)$ and the potentials V_j must be real is not necessary for the algorithm to work. Actually, $\mathrm{w}(x)$ could be complex; we shall address such a case later on.

Now, substituting the explicit form of H_j and L_1^- in the intertwining relation (2.1.2) we obtain

$$\begin{aligned} H_1 L_1^- &= -\frac{d^3}{dx^3} - \mathrm{w}\frac{d^2}{dx^2} + (V_1 - 2\mathrm{w}')\frac{d}{dx} + \mathrm{w}V_1 - \mathrm{w}', \\ L_1^- H_0 &= -\frac{d^3}{dx^3} - \mathrm{w}\frac{d^2}{dx^2} + V_0\frac{d}{dx} + \mathrm{w}V_0 + V_0'. \end{aligned} \tag{2.1.4}$$

Comparing terms with the same powers of d/dx, the following equations are reached

$$\begin{aligned} V_1 &= V_0 + 2\mathrm{w}', \\ \mathrm{w}V_1 - \mathrm{w}'' &= \mathrm{w}V_0 + V_0'. \end{aligned} \tag{2.1.5}$$

If the first equation (2.1.5) is substituted in the second one, it appears the following differential equation

$$2\mathrm{w}\mathrm{w}' - \mathrm{w}'' = V_0'. \tag{2.1.6}$$

By integrating this expression it is obtained a particular case of the Riccati equation [Ince, 1956], namely,

$$\mathrm{w}' - \mathrm{w}^2 + V_0 - \epsilon = 0, \tag{2.1.7}$$

where ϵ is a constant called factorization energy. Thus, in terms of the superpotential the potentials V_j can be written as

$$\begin{aligned} V_0 &= \mathrm{w}^2 - \mathrm{w}' + \epsilon, \\ V_1 &= \mathrm{w}^2 + \mathrm{w}' + \epsilon. \end{aligned} \tag{2.1.8}$$

Although it is possible to solve the Riccati equation (2.1.7), in the context of SUSY QM it is appropriate to make the change of variable

$$\mathrm{w} = -\frac{u'}{u}, \tag{2.1.9}$$

in order to arrive to the more familiar equation

$$-u'' + V_0 u = \epsilon u. \tag{2.1.10}$$

Said in words, $u(x)$ is a formal eigenfunction of the initial Hamiltonian H_0 associated to ϵ, and it is called seed solution in the literature.

On the other hand, we can define another first-order differential operator,

$$L_1^+ = -\frac{d}{dx} + \mathrm{w}, \tag{2.1.11}$$

which for $\mathrm{w}(x)$ real turns out to be the hermitian conjugate of L_1^-. Two important products of both operators are given by

$$\begin{aligned} L_1^+ L_1^- &= -\frac{d^2}{dx^2} + \mathrm{w}^2 - \mathrm{w}', \\ L_1^- L_1^+ &= -\frac{d^2}{dx^2} + \mathrm{w}^2 + \mathrm{w}'. \end{aligned} \tag{2.1.12}$$

Due to equation (2.1.8), the Hamiltonians H_j become factorized by the operators $L_1^\pm$ as follows,

$$H_0 = L_1^+ L_1^- + \epsilon, \quad H_1 = L_1^- L_1^+ + \epsilon. \tag{2.1.13}$$

As we mentioned before, it is supposed that H_0 is a solvable Hamiltonian whose eigenvalues $\mathcal{E}_n^{(0)}$ and eigenfunctions $\psi_n^{(0)}(x)$ are known, where n is a non-negative integer. Thus, we can determine the eigenfunctions $\psi_n^{(1)}(x)$ of H_1 from the relation

$$\psi_n^{(1)}(x) = \frac{L_1^- \psi_n^{(0)}(x)}{\sqrt{\mathcal{E}_n^{(0)} - \epsilon}}, \tag{2.1.14}$$

its corresponding eigenvalues being $\mathcal{E}_n^{(0)}$. However, the spectrum of H_1 could also contain the factorization energy ϵ, since equation (2.1.13) implies that if a function $\psi_\epsilon^{(1)}$ (provided it is square-integrable) is in the *kernel* of the operator L_1^+ then $H_1\psi_\epsilon^{(1)} = \epsilon\psi_\epsilon^{(1)}$. Moreover, from the first-order differential equation $L_1^+\psi_\epsilon^{(1)} = 0$ it follows that

$$\frac{d\psi_\epsilon^{(1)}}{dx} = \mathrm{w}\psi_\epsilon^{(1)}, \tag{2.1.15}$$

therefore

$$\psi_\epsilon^{(1)}(x) \propto e^{\int \mathrm{w}(x)dx} = \frac{1}{u(x)}. \tag{2.1.16}$$

Note that it is possible as well to get the eigenfunctions $\psi_n^{(0)}(x)$ from $\psi_n^{(1)}(x)$ through the relation

$$\psi_n^{(0)}(x) = \frac{L_1^+\psi_n^{(1)}(x)}{\sqrt{\mathcal{E}_n^{(0)} - \epsilon}}. \tag{2.1.17}$$

As it can be seen, both the superpotential $\mathrm{w}(x)$ and the eigenfunction $\psi_\epsilon^{(1)}(x)$ are inversely proportional to the seed solution $u(x)$, thus it must be nodeless. In order to ensure this requirement, the factorization energy ϵ should take values below or equal to the ground state energy $\mathcal{E}_0^{(0)}$ of H_0 [Sukumar, 1985a,b].

Let us illustrate the first-order SUSY QM operation through the harmonic oscillator Hamiltonian

$$H_0 = -\frac{d^2}{dx^2} + \omega^2 x^2, \tag{2.1.18}$$

whose eigenvalues and eigenfunctions are given by

$$\mathcal{E}_n^{(0)} = 2\omega\left(n + \frac{1}{2}\right), \quad \psi_n^{(0)}(x) = c_n e^{-\omega\frac{x^2}{2}}\mathrm{H}_n\left(\sqrt{\omega}x\right), \tag{2.1.19}$$

with n being a non negative integer. For implementing the first-order SUSY QM it is necessary to choose a seed solution $u(x)$ associated to the factorization energy such that $\epsilon \leq \mathcal{E}_0^{(0)}$, for example, let us take

$$\epsilon = \mathcal{E}_0^{(0)} = \omega, \quad u(x) = \psi_0^{(0)}(x) = c_0 e^{-\omega\frac{x^2}{2}}. \tag{2.1.20}$$

Thus, equation (2.1.9) leads to the superpotential $\mathrm{w} = \omega x$, while the intertwining operator and the SUSY partner Hamiltonian can be calculated using equations (2.1.3) and (2.1.8), respectively. We get that

$$L_1^- = \frac{d}{dx} + \omega x, \quad H_1 = -\frac{d^2}{dx^2} + \omega^2 x^2 + 2\omega. \tag{2.1.21}$$

The eigenvalues and eigenfunctions of H_1 become

$$\mathcal{E}_n^{(1)} = \mathcal{E}_{n+1}^{(0)}, \quad \psi_n^{(1)}(x) = \psi_n^{(0)}(x), \quad n = 0, 1, 2, \ldots \tag{2.1.22}$$

It is important to notice that $\mathrm{sp}[H_1] = \left\{2\omega\left(n + \frac{1}{2}\right) \mid n = 1, 2, \ldots\right\}$, thus the factorization energy $\epsilon = \mathcal{E}_0^{(0)}$ does not belong to that set since $\psi_\epsilon^{(1)}(x) = e^{\omega\frac{x^2}{2}}$ is not square-integrable. Furthermore,

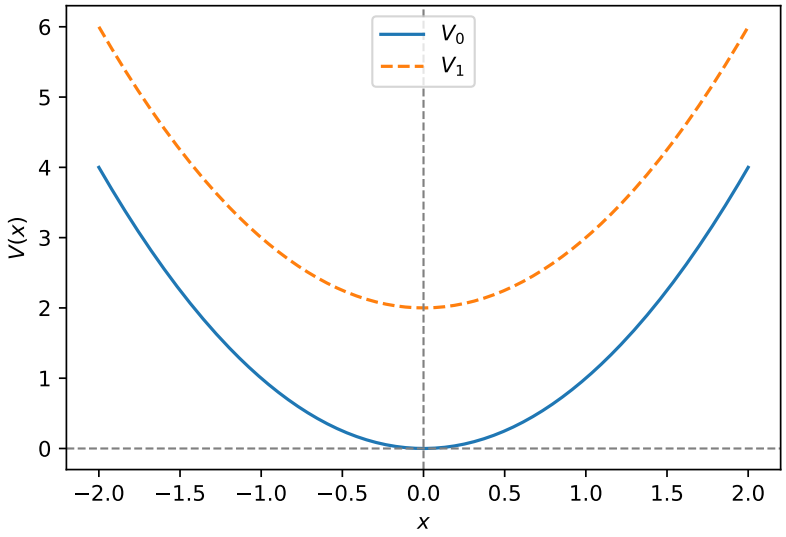

Figure 2.1: Harmonic oscillator potential and its first-order SUSY partner. The factorization energy taken was $\epsilon = \mathcal{E}_0^{(0)}$, for this plot we choose $\omega = 1$.

the eigenfunctions $\psi_n^{(1)}(x)$ of H_1 have the same functional form (actually they are the same) than the eigenfunctions of H_0 because V_0 and V_1 are shape-invariant potentials [Bagchi, 2001; Cariñena and Ramos, 2000; Dong, 2007; Sandhya et al., 2015], see Figure 2.1. Such a class of potentials fulfil

$$V_1(x, \lambda_1) = V_0(x, \lambda_0) + C(\lambda_1), \tag{2.1.23}$$

where λ_j are labels representing the corresponding potential parameters, λ_1 is a function of λ_0 and $C(\lambda_1)$ is an additive constant [Gangopadhyaya et al., 2018]. Equation (2.1.23) means that both potentials have the same functional dependence of x, but they have different potential parameters. In our example it turns out that $V_1(x, \omega) = V_0(x, \omega) + 2\omega$, $\lambda_1 = \lambda_0 = \omega$ and thus it follows equation (2.1.22).

Section 2.2

Second-order supersymmetric quantum mechanics

As we mentioned before, in the second-order SUSY QM [Andrianov et al., 1995, 1993; Fernandez, 2010, 2019; Samsonov, 1999] it is taken a second-order differential operator L_2^- intertwining two Schrödinger-like Hamiltonians with the same form as equation (2.1.1) for $j = 0, 2$. The intertwining relation reads now

$$H_2 L_2^- = L_2^- H_0, \tag{2.2.1}$$

with the intertwining operator being given by

$$L_2^- = \frac{d^2}{dx^2} + \eta(x)\frac{d}{dx} + \gamma(x). \tag{2.2.2}$$

Substituting the explicit expressions of H_j and L_2^- in equation (2.2.1), it turns out that

$$\begin{aligned} H_2L_2^- &= -\frac{d^4}{dx^4} - \eta\frac{d^3}{dx^3} + [V_2 - 2\eta' - \gamma]\frac{d^2}{dx^2} + [V_2\eta - \eta'' - 2\gamma']\frac{d}{dx} + V_2\gamma - \gamma'', \\ L_2^-H_0 &= -\frac{d^4}{dx^4} - \eta\frac{d^3}{dx^3} + [V_0 - \gamma]\frac{d^2}{dx^2} + [2V_0' + \eta V_0]\frac{d}{dx} + V_0'' + \eta V_0' + \gamma V_0. \end{aligned} \tag{2.2.3}$$

If we compare the terms with the same powers of d/dx, the following expressions are obtained

$$\begin{aligned} &V_2 = V_0 + 2\eta', \\ &V_2\eta - \eta'' - 2\gamma' = 2V_0' + \eta V_0, \\ &V_2\gamma - \gamma'' = V_0'' + \eta V_0' + \gamma V_0. \end{aligned} \tag{2.2.4}$$

By plugging the first row of the previous equation in the second one, we arrive at

$$\gamma' = \eta\eta' - \frac{\eta''}{2} - V_0'. \tag{2.2.5}$$

Integrating this result, we get the function γ in terms of η

$$\gamma = \frac{\eta^2}{2} - \frac{\eta'}{2} - V_0 + d, \tag{2.2.6}$$

with d being a real constant.

On the other hand, if we insert the first row of equation (2.2.4) in the third one we can express the second derivative of γ in the form

$$\gamma'' = 2\gamma\eta' - V_0'' - \eta V_0'. \tag{2.2.7}$$

Taking now the derivative of equation (2.2.5), we have

$$\gamma'' = (\eta')^2 + \eta\eta'' - \frac{\eta'''}{2} - V_0''. \tag{2.2.8}$$

Substituting equations (2.2.8) and (2.2.6) in (2.2.7) it is obtained the third-order differential equation

$$2V_0\eta' + \eta V_0' = \frac{\eta'''}{2} - 2(\eta')^2 - \eta\eta'' + \eta^2\eta' + 2\eta' d. \tag{2.2.9}$$

Multiplying the previous expression by η, then adding and subtracting $\eta'\eta''/2$ and integrating the result leads to the non-linear second-order differential equation

$$\frac{\eta\eta''}{2} - \left(\frac{\eta'}{2}\right)^2 - \eta^2\eta' + \frac{\eta^4}{4} - \eta^2 V_0 + \eta^2 d + c = 0, \tag{2.2.10}$$

with c being another real constant. In order to solve this equation, the following *ansätz* is proposed

$$\eta' = \eta^2 + 2\beta\eta - 2\varepsilon, \tag{2.2.11}$$

where $\beta(x)$ and $\varepsilon(x)$ are functions to be determined. Calculating the derivative of equation (2.2.11) and its square it is found that

$$\begin{aligned} \frac{\eta\eta''}{2} &= \eta^2\eta' + \beta'\eta^2 + \beta\eta\eta' - \eta\varepsilon', \\ -\left(\frac{\eta'}{2}\right)^2 &= -\frac{\eta^4}{4} - \eta^3\beta + \left(\varepsilon - \beta^2\right)\eta^2 + 2\varepsilon\beta\eta - \varepsilon^2. \end{aligned} \tag{2.2.12}$$

By plugging the two previous expressions into equation (2.2.10), it turns out that

$$\beta'\eta^2 + \beta\eta\eta' - \eta\varepsilon' - \eta^3\beta + \left(\varepsilon - \beta^2\right)\eta^2 + 2\varepsilon\beta\eta - \varepsilon^2 - \eta^2 V_0 + \eta^2 d + c = 0. \tag{2.2.13}$$

If we substitute once again the *ansätz* (2.2.11) in order to eliminate η' in the previous expressions we arrive at

$$\left(\beta' + \beta^2 - V_0 + \varepsilon + d\right)\eta^2 - \varepsilon'\eta + c - \varepsilon^2 = 0. \tag{2.2.14}$$

Since this equation has to be valid for an arbitrary η the coefficient of each power must vanish. Therefore, we conclude that ε is a constant whose square is equal to c. Moreover, β satisfies the Riccati equation

$$\beta' + \beta^2 = V_0 - \epsilon, \tag{2.2.15}$$

where $\epsilon = d + \varepsilon$. Nevertheless, in the context of SUSY QM it is better to make the change $\beta = u'(x)/u(x)$, hence the Riccati equation (2.2.15) transforms into

$$-u'' + V_0 u = \epsilon u. \tag{2.2.16}$$

Thus, $u(x)$ is a solution of the stationary Schrödinger equation for H_0 associated to the formal eigenvalue ϵ, which is called seed solution in a similar way as for the first-order case. Since $\varepsilon = \pm\sqrt{c}$, in general there are two possible values for ϵ, namely, $\epsilon_1 = d + \sqrt{c}$, $\epsilon_2 = d - \sqrt{c}$, and of course two associated seed solutions u_j, $j = 1, 2$.

Analogously to the first-order SUSY QM, we define the hermitian conjugate of L_2^- as follows

$$L_2^+ = \left(L_2^-\right)^\dagger = \frac{d^2}{dx^2} - \eta\frac{d}{dx} + \gamma - \eta'. \tag{2.2.17}$$

The product $L_2^+ L_2^-$ turns out to be

$$L_2^+ L_2^- = \frac{d^4}{dx^4} + \left(2\gamma - \eta^2 + \eta'\right)\frac{d^2}{dx^2} + \left(\eta'' + 2\gamma' - 2\eta\eta'\right)\frac{d}{dx} + \gamma'' - \eta\gamma' + \gamma^2 - \gamma\eta'. \tag{2.2.18}$$

Due to equations (2.2.6), (2.2.7), (2.2.10), and given that $d = \left(\epsilon_1 + \epsilon_2\right)/2$, $c = \left(\epsilon_1 - \epsilon_2\right)^2/4$, the previous product is reduced to

$$L_2^+ L_2^- = \frac{d^4}{dx^4} + \left(\epsilon_1 + \epsilon_2 - 2V_0\right)\frac{d^2}{dx^2} - 2V_0\frac{d}{dx} + V_0^2 - V_0'' - V_0\left(\epsilon_1 + \epsilon_2\right) + \epsilon_1\epsilon_2. \tag{2.2.19}$$

A straightforward calculation allows us to realize that this product is equal to the following second-order polynomial in H_0

$$L_2^+ L_2^- = \left(H_0 - \epsilon_1\right)\left(H_0 - \epsilon_2\right). \tag{2.2.20}$$

On the other hand, the other product $L_2^- L_2^+$ can be written as

$$L_2^- L_2^+ = \frac{d^4}{dx^4} + \left(2\gamma - 3\eta' - \eta^2\right)\frac{d^2}{dx^2} + \left(2\gamma' - 3\eta'' - 2\eta\eta'\right)\frac{d}{dx} + \gamma'' - \eta''' + \eta\gamma' - \gamma\eta' + \gamma^2 - \eta\eta''. \tag{2.2.21}$$

Using equations (2.2.4), (2.2.6), (2.2.7), (2.2.9), (2.2.10), we obtain that

$$L_2^- L_2^+ = \frac{d^4}{dx^4} + \left(\epsilon_1 + \epsilon_2 - 2V_2\right)\frac{d^2}{dx^2} - 2V_2\frac{d}{dx} + V_2^2 - V_2'' - V_2\left(\epsilon_1 + \epsilon_2\right) + \epsilon_1\epsilon_2. \tag{2.2.22}$$

Therefore

$$L_2^- L_2^+ = \left(H_2 - \epsilon_1\right)\left(H_2 - \epsilon_2\right). \tag{2.2.23}$$

A consequence of equations (2.2.20) and (2.2.23) is that the eigenfunctions of the Hamiltonians H_0 and H_2 are related as follows

$$\psi_n^{(0)}(x) = \frac{L_2^+\psi_n^{(2)}(x)}{\sqrt{\left(\mathcal{E}_n^{(0)} - \epsilon_1\right)\left(\mathcal{E}_n^{(0)} - \epsilon_2\right)}}, \quad \psi_n^{(2)}(x) = \frac{L_2^-\psi_n^{(0)}(x)}{\sqrt{\left(\mathcal{E}_n^{(0)} - \epsilon_1\right)\left(\mathcal{E}_n^{(0)} - \epsilon_2\right)}}. \tag{2.2.24}$$

Finally, since c has to fulfil the law of trichotomy of the real numbers, the second-order SUSY QM can be classified into three different cases: the real case when $c > 0$, the confluent case if $c = 0$ and the complex case for $c < 0$. In what remains of this section we shall address each case of this second-order SUSY QM classification.

Subsection 2.2.1

Real case

The most simple way to understand the second-order SUSY QM technique is through the real case, where ϵ_1 and ϵ_2 are two real formal eigenvalues associated to the real seed solutions $u_1(x)$ and $u_2(x)$, or equivalently to the Riccati solutions β_1, β_2. From the *ansätz* (2.2.11) we get two equations

$$\begin{aligned} \eta' &= \eta^2 + 2\beta_1\eta - \left(\epsilon_1 - \epsilon_2\right), \\ \eta' &= \eta^2 + 2\beta_2\eta - \left(\epsilon_2 - \epsilon_1\right), \end{aligned} \tag{2.2.25}$$

and substracting them the function $\eta(x)$ is obtained

$$\eta = \frac{\epsilon_1 - \epsilon_2}{\beta_1 - \beta_2}. \tag{2.2.26}$$

In terms of the seed solutions it turns out that

$$\eta = -\frac{\left(\epsilon_1 - \epsilon_2\right)u_1 u_2}{W\left(u_1, u_2\right)}, \tag{2.2.27}$$

where $W(f, g) = fg' - f'g$ is the Wronskian of f and g. Using the Schrödinger equation (2.2.16) it is obtained the more useful form

$$\eta = -\frac{W'\left(u_1, u_2\right)}{W\left(u_1, u_2\right)}. \tag{2.2.28}$$

To avoid singularities induced by the transformation, the Wronskian $W\left(u_1, u_2\right)$ must not have zeros in the appropriate x-domain.

As mentioned previously, the eigenfunctions of both Hamiltonians are linked through the expressions given in equation (2.2.24). However, the spectrum of H_2, $\mathrm{Sp}\left(H_2\right)$, could contain two extra levels as compared with $\mathrm{Sp}\left(H_0\right)$, corresponding to the factorization energies ϵ_1, ϵ_2. This depends on the normalizability of the formal eigenfunctions $\psi_{\epsilon_1}^{(2)}(x)$, $\psi_{\epsilon_2}^{(2)}(x)$ associated to these factorization energies, and since (2.2.23) they are as well in the *kernel* of L_2^+ thus they satisfy

$$\begin{aligned} &\psi_{\epsilon_j}^{(2)\prime\prime} - \eta\psi_{\epsilon_j}^{(2)\prime} + \left(\gamma - \eta'\right)\psi_{\epsilon_j}^{(2)} = 0, \\ &\psi_{\epsilon_j}^{(2)\prime\prime} - \left(V_2 - \epsilon_j\right)\psi_{\epsilon_j}^{(2)} = 0. \end{aligned} \tag{2.2.29}$$

Substituting $\psi_{\epsilon_j}^{(2)\prime\prime}$ of the second row in the first one we arrive at

$$\eta\psi_{\epsilon_j}^{(2)\prime} = \left(\gamma - \eta' + V_2 - \epsilon_j\right)\psi_{\epsilon_j}^{(2)}. \tag{2.2.30}$$

Using now equations (2.2.6), (2.2.4) and (2.2.11) it is obtained that

$$\eta\psi_{\epsilon_j}^{(2)\prime} = \left(\eta' - \beta_j\eta\right)\psi_{\epsilon_j}^{(2)}. \tag{2.2.31}$$

Expressed in terms of the seed solutions u_j, this differential equation can be written as

$$\frac{\psi_{\epsilon_j}^{(2)\prime}}{\psi_{\epsilon_j}^{(2)}} = \frac{\eta'}{\eta} - \frac{u_j'}{u_j}, \tag{2.2.32}$$

whose solution is given by

$$\psi_{\epsilon_j}^{(2)} \propto \frac{\eta}{u_j}. \tag{2.2.33}$$

An explicit form can be gotten if the expression for η in equation (2.2.27) is used, so that

$$\psi_{\epsilon_1}^{(2)} \propto \frac{u_2}{W\left(u_1, u_2\right)}, \quad \psi_{\epsilon_2}^{(2)} \propto \frac{u_1}{W\left(u_1, u_2\right)}. \tag{2.2.34}$$

The second-order SUSY algorithm offers a wider range of possibilities for modifying the spectra than the first-order case. Nevertheless, there exist some constraints about which factorization energies and their corresponding eigenfunctions can be chosen, arising from the fact that the Wronskian of the seed solutions must be nodeless. A heuristic criterion helping us to identify the appropriate seed solutions $u_j(x)$ is the following. Since $L_2^+L_2^- = \left(H_0 - \epsilon_1\right)\left(H_0 - \epsilon_2\right)$, any average of this operator product must be positive definite on the corresponding Hilbert space, i.e.,

$$\langle\psi_n^{(0)}|L_2^+L_2^-|\psi_n^{(0)}\rangle = |L_2^-|\psi_n^{(0)}\rangle|^2 \geq 0, \tag{2.2.35}$$

which implies that

$$\left(\mathcal{E}_n^{(0)} - \epsilon_1\right)\left(\mathcal{E}_n^{(0)} - \epsilon_2\right) \geq 0. \tag{2.2.36}$$

Thus, our prospective factorization energy range can be reduced to the next cases:

a) Both factorization energies are taken below the ground state, $\epsilon_2 < \epsilon_1 < \mathcal{E}_0^{(0)}$, their corresponding seed solutions are chosen such that $u_1(x)$ is nodeless and $u_2(x)$ has one zero in the initial x-domain, which guarantee that the Wronskian $W\left(u_1, u_2\right)$ will be nodeless.

b) Both factorization energies are placed between two consecutive bound state energies, $\mathcal{E}_j^{(0)} < \epsilon_2 < \epsilon_1 < \mathcal{E}_{j+1}^{(0)}$. In order to make the Wronskian of the corresponding seed solutions to be nodeless, we choose $u_1(x)$, $u_2(x)$ having $j+1, j+2$ zeros, respectively. In that way these zeros are alternating thus making that $W(u_1, u_2)$ will be nodeless.

c) Both factorization energies are equal to two consecutive bound state energies, $\epsilon_2 = \mathcal{E}_j^{(0)}$, $\epsilon_1 = \mathcal{E}_{j+1}^{(0)}$, and consequently $u_2(x) = \psi_j^{(0)}(x)$, $u_1(x) = \psi_{j+1}^{(0)}(x)$. It is worth noting that although such seed solutions have j and $j+1$ zeros inside the x-domain, respectively, they vanish at both ends of such domain. These asymptotic zeros allow to show that $W(u_1, u_2)$ is nodeless in the full domain.

d) Finally, it is possible to choose one factorization energy as a bound state energy $\mathcal{E}_j^{(0)}$ and the other one between $\mathcal{E}_j^{(0)}$ and the previous energy level, i.e., $\mathcal{E}_{j-1}^{(0)} < \epsilon_2 < \epsilon_1 = \mathcal{E}_j^{(0)}$. The seed solutions are chosen as $u_1(x) = \psi_j^{(0)}(x)$ and $u_2(x)$ with $j+1$ zeros, thus making the corresponding Wronskian to be nodeless.

Further details about these possibilities can be found in [Fernandez and Fernandez-Garcia, 2005]; an interesting work on SUSY QM applied to the Pöschl-Teller potential, in particular the cases described above, is [Contreras-Astorga and Fernández C., 2008].

Now, let us explore the example of a real second-order SUSY QM transformation applied to the harmonic oscillator Hamiltonian of equation (2.1.18). The general solution of the stationary Schrödinger equation can be written as

$$u(x) = e^{-\omega\frac{x^2}{2}}\left[{}_1F_1\left(\frac{1}{4} - \frac{\epsilon}{4\omega}; \frac{1}{2}; \omega x^2\right) - 2x\nu\frac{\Gamma\left(\frac{3}{4} - \frac{\epsilon}{4\omega}\right)}{\Gamma\left(\frac{1}{4} - \frac{\epsilon}{4\omega}\right)}\,{}_1F_1\left(\frac{3}{4} - \frac{\epsilon}{4\omega}; \frac{3}{2}; \omega x^2\right)\right], \quad (2.2.37)$$

where ν is a real constant. Note that $u(x)$ is nodeless for $\epsilon < \omega$ and $|\nu| \leq 1$.

The second-order SUSY partner potential $V_2(x)$ of $V_0(x)$, obtained by taking the ground state of H_0 (see equation (2.1.20)) as the first seed solution, $u_1(x) = \psi_0^{(0)}(x)$, and $u_2(x)$ as the expression of equation (2.2.37) for zero energy, $\epsilon = 0$, and $\nu = 1.1$, is plotted in Figure 2.2. It is worth noticing that the spectrum of H_2 becomes $\mathrm{Sp}(H_2) = \{0, 3\omega, 5\omega, \dots\}$, in other words, we have deleted the level with energy ω and replaced it with the zero energy level. This is a consequence that the Wronskian in equation (2.2.34) is nodeless inside the x-domain, and it does not have asymptotic zeros, thus leaving the square-integrability of $\psi_{\epsilon_1}^{(2)}(x)$, $\psi_{\epsilon_2}^{(2)}(x)$ to depend on $u_2(x)$, $\psi_0^{(0)}(x)$, respectively.

Subsection 2.2.2

Confluent case

The main feature of this case is that the two factorization energies are equal, $\epsilon_1 = \epsilon_2 = \epsilon \in \mathbb{R}$, so, there is only one seed solution $u(x)$. On the other hand, the *ansätz* (2.2.11) leads to the next equation for η

$$\eta' = \eta^2 + 2\beta\eta. \quad (2.2.38)$$

Making the change of variable $\eta = 1/y$ we arrive at

$$y' + 2\beta y = -1. \quad (2.2.39)$$

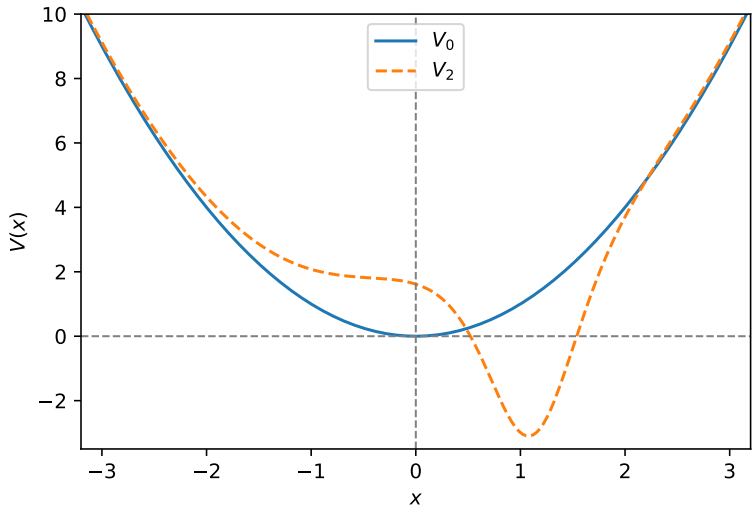

Figure 2.2: Harmonic oscillator potential and its second-order SUSY partner in the real case. The factorization energies were chosen as $\epsilon_1 = \omega$, $\epsilon_2 = 0$, for $\omega = 1$ and $\nu = 1.1$.

This inhomogeneous first-order linear differential equation has a one-parametric family of solutions given by

$$y(x;\omega_0) = \left[\omega_0 - \int e^{2\int \beta dx} dx\right] e^{-2\int \beta dx}. \tag{2.2.40}$$

If we remember that $\beta(x)$ is expressed in terms of $u(x)$ as $\beta(x) = u'(x)/u(x)$, it turns out that $u(x) \propto e^{\int \beta(x)dx}$ and thus the function η becomes

$$\eta(x;\omega_0) = \frac{u^2}{\omega_0 - \int_{x_0}^{x} u^2(y)dy} = -\frac{\mathrm{w}'(x)}{\mathrm{w}(x)}, \tag{2.2.41}$$

with $\mathrm{w}(x) \equiv \omega_0 - \int_{x_0}^{x} u^2(y)dy$. In order to avoid singularities in $\eta(x)$, $\mathrm{w}(x)$ has to be nodeless. Since $\mathrm{w}(x)$ is a decreasing monotonic function, we can select the seed solution in the following way:

a) It is an eigenfunction of H_0, $u(x) = \psi_n^{(0)}$. Thus, it is fulfilled that $u(x \to \pm\infty) = 0$ and $\int_{-\infty}^{\infty} u^2(y)dy = 1$. It is suitable to choose x_0 as the left end of the domain, then $\mathrm{w}(x)$ is nodeless when $\omega_0 \geq 1$ or $\omega_0 \leq 0$.

b) It fulfils $u(x \to -\infty) = 0$ and $I_- = \int_{-\infty}^{x_0} u^2(y)dy < \infty$. Since the seed solution $u(x)$ is a non-physical eigenfunction of H_0, then $u(x \to \infty)$ does not converge and thus $w(x \to \infty) = -\infty$. Consequently, for $\omega_0 \leq -I_-$ it is guaranteed that $\mathrm{w}(x)$ is nodeless.

c) It is such that $u(x \to \infty) = 0$ and $I_+ = \int_{x_0}^{\infty} u^2(y)dy < \infty$. Thus $w(x \to -\infty) = \infty$ and the ω_0-domain for which $\mathrm{w}(x)$ is nodeless is $\omega_0 \geq I_+$.

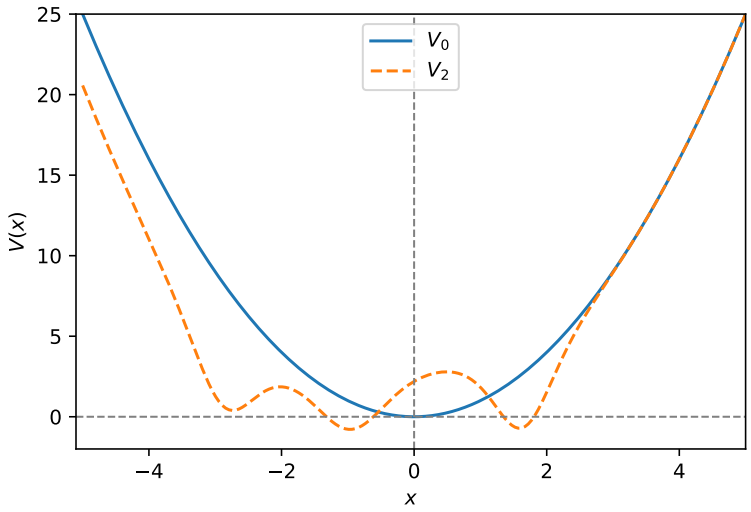

Figure 2.3: Harmonic oscillator potential and its second-order SUSY partner in the confluent case. The factorization energy was chosen as $\epsilon = 2\omega$, with $\omega = \nu = 1$, $x_0 = 0$ and $\omega_0 = 3$.

Analogously to the real case, we can obtain the expression for the formal eigenfunction $\psi_\epsilon^{(2)}$ of H_2 associated to the factorization energy ϵ. It is found that

$$\psi_\epsilon^{(2)}(x) \propto \frac{\eta(x)}{u(x)} = \frac{u(x)}{\mathrm{w}(x)}. \tag{2.2.42}$$

The factorization energy ϵ could belong to Sp (H_2), depending on the square-integrability of $\psi_\epsilon^{(2)}$. There exist two possibilities: i) if ω_0 is exactly equal to one of the edges where $\mathrm{w}(x)$ is nodeless, for example in the previous case c) $\omega_0 = I_+$, then $\psi_\epsilon^{(2)}(x)$ is not square-integrable and thus ϵ does not belong to Sp (H_2) (this will be called limit case); ii) when ω_0 lies inside the nodeless domain the eigenfunction $\psi_\epsilon^{(2)}(x)$ of H_2 is square-integrable and thus ϵ belongs to Sp (H_2) (this will be called the standard case).

As an example, let us take the initial harmonic oscillator Hamiltonian of equation (2.1.18) with $\omega = 1$. If we choose the factorization energy as $\epsilon = 2$, whose corresponding seed solution $u(x)$ is obtained from equation (2.2.37) with $\nu = 1$, the second-order SUSY partner potential $V_2(x)$ of $V_0(x)$ looks like the plot of Figure 2.3. The remaining parameters are taken as $x_0 = 0$ and $w_0 = 3$, the last lies inside the domain where $\mathrm{w}(x)$ is nodeless and $\psi_\epsilon^{(2)}(x)$ is square integrable. The spectrum of H_2 is $\{\omega, 2\omega, 3\omega, 5\omega \dots\}$, i.e., a SUSY partner Hamiltonian containing a new energy level above the ground state of H_0 has been generated. This spectre manipulation can not be carried out via the first-order SUSY technique, which highlights the difference between the first-order case and the confluent second-order SUSY QM. Despite both seem to be equal, the second-order transformation can be seen as an iteration procedure of two first-order singular ones.

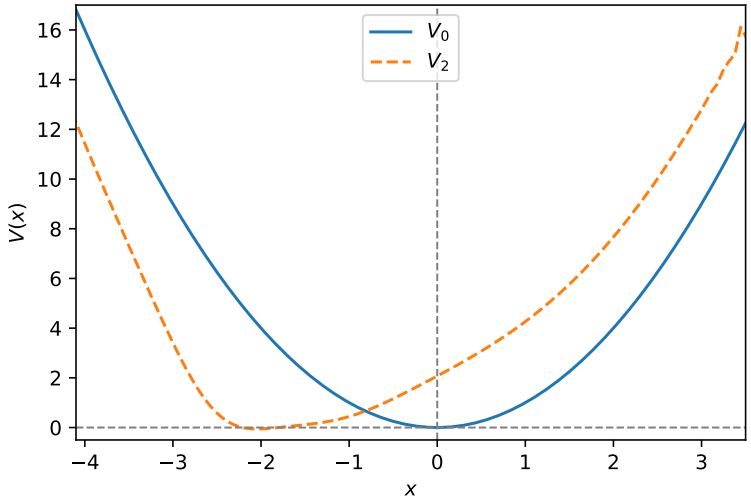

Figure 2.4: Harmonic oscillator potential and its second-order SUSY partner in the complex case. The factorization energy is taken as $\epsilon_1 = 1 + i$, and $\omega = \nu_1 = 1$.

Subsection 2.2.3

Complex case

Finally, the complex case of the second-order SUSY QM is called in this way since the two factorization energies are complex. Although we can choose these factorization energies, in general, as two arbitrary complex numbers, we will describe here just the algorithm leading to a SUSY partner potential $V_2(x)$ which is real. The function $\eta(x)$ can be calculated analogously to the real case, see equation (2.2.26); as it should be real the conditions $\epsilon_2 = \overline{\epsilon}_1$ and $\beta_2 = \overline{\beta}_1$ are required. Thus, we arrive at

$$\eta = \frac{\text{Im}[\epsilon_1]}{\text{Im}[\beta_1]}. \tag{2.2.43}$$

In terms of the seed solutions $u_1(x)$ and $u_2(x) = \overline{u}_1(x)$ the function $\eta(x)$ is expressed as

$$\eta = -\frac{(\epsilon_1 - \overline{\epsilon}_1)\,|u_1|^2}{W\left(u_1, \overline{u}_1\right)}. \tag{2.2.44}$$

The Wronskian of the two seed solutions in the previous expression must be nodeless to ensure that the potential $V_2(x)$ does not have added singularities. Since $W'\left(u_1, \overline{u}_1\right) / \left(\epsilon_1 - \overline{\epsilon}_1\right) = |u_1(x)|^2 \geq 0$, hence this normalized Wronskian is a non-decreasing monotonic function. Then, in order to guarantee it will be nodeless it is sufficient that either of the following two limits are fulfilled

$$u_1(x \to \infty) = 0 \quad \text{or} \quad u_1(x \to -\infty) = 0. \tag{2.2.45}$$

As the formal eigenfunctions $\psi^{(2)}_{\epsilon_j}(x)$ are given in equation (2.2.34), with the considerations taken into account previously and due to the conditions (2.2.45), they are not square-integrable. Therefore, the Hamiltonian H_2 is isospectral to H_0.

As an example, let us take as seed solution the $u_1(x)$ equation (2.2.37) with $\omega = \nu_1 = 1$, associated to the factorization energy $\epsilon_1 = 1 + i$. The SUSY partner potentials V_2 and V_0 are shown in Figure 2.4. As we mentioned before, both potentials have the same spectrum since $\psi^{(2)}_{\epsilon_1}(x)$ and $\psi^{(2)}_{\bar{\epsilon}_1}(x)$ are not square-integrable.

We must mention that it is possible to choose the seed solutions associated to two in general complex factorization energies, without requiring that $\epsilon_2 = \bar{\epsilon}_1$ such that the SUSY partner potential $V_2(x)$ is not singular. However, $V_2(x)$ turns out to be complex, thus H_2 in general is non-hermitian, which is not usually worked in SUSY QM. Despite this, in chapter 6 an effective complex magnetic field applied to monolayer graphene will be considered, which will lead us to deal with a pair of complex first-order SUSY partners potentials, and to determine some exact solutions for them. The case of bilayer graphene under similar complex magnetic fields, which leads to analyze two complex second-order SUSY partners potentials, is left for a future study.

Chapter 3

Shape-invariant potentials

As we have seen in chapter 1, a lot of papers in the literature have addressed the effect of a magnetic field applied to monolayer graphene, from which we obtain a system of equations that can be solved using the first-order SUSY QM described in chapter 2. Here, we will implement the same idea but for bilayer graphene, which leads us to the system of equations (1.4.14). However, the operator L_2^- appearing there turned out to be the square of the first-order differential operator $d/dx + k + (e/c\hbar)A(x)$, which limits a lot the use of the second-order SUSY QM. In order to surpass that restriction, and to apply in a straightforward way this technique, we will make two assumptions:

a) L_2^- will be a second-order differential intertwining operator which can be expressed in general as a product of two different first-order differential operators, whose form is given in equation (2.2.2). Substituting the expression (2.2.10) in (2.2.6), the function $\gamma(x)$ will be given by

$$\gamma = \frac{\eta'}{2} + \frac{\eta^2}{4} - \frac{\eta''}{2\eta} + \left(\frac{\eta'}{2\eta}\right)^2 - \left(\frac{\epsilon_1 - \epsilon_2}{2\eta}\right)^2. \tag{3.1}$$

We can see that the first two terms in the previous formula correspond to those appering in the system of equations (1.4.14), i.e., they are the terms necessary for the operator L_2^- to have a part which is the square of a first-order differential operator. Meanwhile, the remaining terms are required for this operator to be a general second-order differential intertwining operator of the form (2.2.2).

b) The vector potential amplitude $\mathbf{A}(x)$ giving rise to the external magnetic field $\mathbf{B}(x)$ applied to bilayer graphene and the coefficient $\eta(x)$ of the second term of L_2^- are related as follows

$$\eta(x) = 2\left(k + \frac{e}{c\hbar}A(x)\right). \tag{3.2}$$

Thus, the derivative of $\eta(x)$ produces the magnetic field amplitude in the following way

$$\eta'(x) = \frac{2e}{c\hbar}B(x). \tag{3.3}$$

It is important to stress that the function $\eta(x)$ depends on the parameters of the initial potential V_0. In turn, these parameters depend of the wavenumber k, and we should be able to find such a dependence. However, in general this is not an easy calculation (see appendix A).

Therefore, the Hamiltonian (1.4.12) has been modified to the form

$$H_b = -\frac{1}{2m}\begin{pmatrix} 0 & \Pi^2 \\ \left(\Pi^\dagger\right)^2 & 0 \end{pmatrix} + \frac{\hbar^2}{2m} f(x)\sigma_x, \tag{3.4}$$

where $\Pi = p_x - ip_y - i(e/c)A(x)$, $f(x) = (\eta'/2\eta)^2 - \eta''/2\eta - [(\epsilon_1 - \epsilon_2)/2\eta]^2$ and σ_x is a Pauli matrix. Note that the second term in the previous Hamiltonian H_b could be associated to spatially varying external potentials, large-distance hopping processes, etcetera [Castillo-Celeita et al., 2020; Wu et al., 2012].

As a first approach to the problem, in this chapter we shall take some initial potentials $V_0(x)$ for which we know the solution and then determine the magnetic field that must be applied to the bilayer graphene for producing $V_0(x)$ as well as its SUSY partner potential $V_2(x)$, such that both will be shape-invariant in the sense explained at the end of section 2.1. In order to carry out this procedure, we choose the two factorization energies as the ground state and the first exited state eigenvalues of the initial Hamiltonian, i.e.,

$$\epsilon_2 = \mathcal{E}_0^{(0)}, \quad \epsilon_1 = \mathcal{E}_1^{(0)}, \tag{3.5}$$

and the corresponding seed solutions are taken as

$$u_2(x) = \psi_0^{(0)}(x), \quad u_1(x) = \psi_1^{(0)}(x). \tag{3.6}$$

It can be seen that this choice of factorization energies belongs to the real case of the second-order SUSY QM described in section 2.2. Thereby, the function $\eta(x)$ is calculated via equation (2.2.28), the corresponding magnetic field is obtained through equation (3.3), and the SUSY partner potential $V_2(x)$ is determined from equation (2.2.4). Since we know in advance the eigenfunctions of the initial potential, and because $V_0(x)$, $V_2(x)$ are shape-invariant, then the eigenfunctions $\psi_n^{(2)}(x)$ have the same functional form as $\psi_n^{(0)}(x)$ but with the corresponding parameters change. Meanwhile, the formal eigenfunctions $\psi_{\epsilon_1}^{(2)}(x)$, $\psi_{\epsilon_2}^{(2)}(x)$ in equation (2.2.34) are not square integrable. Thus, the spectrum of H_2 has two energies less than $\mathrm{Sp}(H_0)$. Comparing the system of equations (1.4.14), including of course the assumptions a), b) and the action of the operators (2.2.20) and (2.2.23) onto the eigenfunctions of the two intertwined Hamiltonians H_0, H_2, it is possible to find the eigenvectors and eigenenergies of the electron (hole) in bilayer graphene as follows

$$\begin{aligned} \Psi_{0,\ell}(x,y) &= e^{iky}\begin{pmatrix} 0 \\ \psi_\ell^{(0)}(x) \end{pmatrix}, \quad E_0 = 0, \quad \ell = 0,1, \\ \Psi_{n-1}(x,y) &= \frac{e^{iky}}{\sqrt{2}}\begin{pmatrix} \psi_{n-2}^{(2)}(x) \\ \psi_n^{(0)}(x) \end{pmatrix}, \quad E_{n-1} = \pm\frac{\hbar^2}{2m}\sqrt{\left(\mathcal{E}_n^{(0)} - \mathcal{E}_0^{(0)}\right)\left(\mathcal{E}_n^{(0)} - \mathcal{E}_1^{(0)}\right)}, \end{aligned} \tag{3.7}$$

with $n \in \{2,3,4,\dots\}$. Note that the positive energies correspond to electrons and the negatives ones to holes. It is important to stress that the ground state eigenvectors have an extra index ℓ to indicate the double degeneracy of E_0. This fact does not depend neither on the magnetic field applied nor on the parameters of the auxiliar potentials.

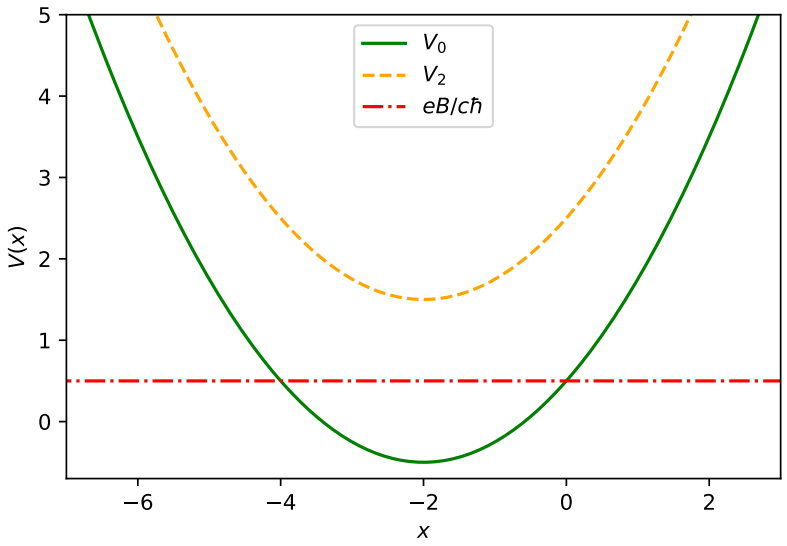

Figure 3.1: Harmonic oscillator potential, its shape-invariant SUSY partner and the associated constant magnetic field. The parameter values taken are $\omega = k = 1$.

In what follows, three different magnetic profiles will be analysed. Since the time-independent matrix Hamiltonian describing bilayer graphene defines a time-dependent dynamic equation similar to the Dirac one, two important physical quantities will be explored, the probability and current densities given by

$$\rho = \Psi^\dagger \Psi, \quad \mathbf{J} = -\frac{\hbar}{m}\left[\mathrm{Im}\left(\Psi^\dagger \mathbf{j} \Psi\right) + \frac{e}{c\hbar} A(x) \Psi^\dagger \boldsymbol{\varsigma} \Psi\right], \tag{3.8}$$

where

$$j_x = \sigma_x \partial_x + \sigma_y \partial_y, \quad j_y = \sigma_y \partial_x - \sigma_x \partial_y, \quad \varsigma_l = \varepsilon_{lm} \sigma_m, \tag{3.9}$$

with ε_{lm} being the Levi-Civita symbol in two dimensions and σ_l the Pauli matrices. Further details about the current density expression are given in appendix B.

Finally, we must mention that all the parameters of the potentials arising in this chapter will be real non-negative, unless otherwise indicated.

Section 3.1

Shifted harmonic oscillator potential

The first example to be considered is a shifted harmonic oscillator as the initial potential, which can be written in the way

$$V_0(x) = \frac{\omega^2}{4}\left(x + \frac{2\kappa}{\omega}\right)^2 - \frac{\omega}{2}, \tag{3.1.1}$$

whose eigenfunctions and eigenvalues are

$$\psi_n^{(0)}(x) = c_n e^{-\frac{\zeta^2}{2}} \mathcal{H}_n(\zeta), \quad \mathcal{E}_n^{(0)} = n\omega, \tag{3.1.2}$$

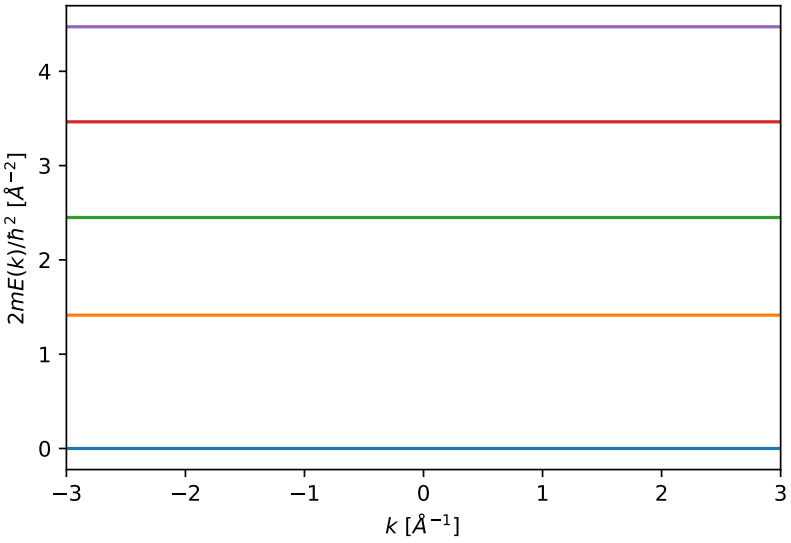

Figure 3.2: First electron energies as functions of k for bilayer graphene in a constant magnetic field with $\omega = 1$.

with n being a non-negative integer, $\mathcal{H}_n(\zeta)$ are the Hermite polynomials, $\zeta = \sqrt{\omega/2}\,(x + 2\kappa/\omega)$ and c_n is a normalization factor. Selecting the factorization energies and seed solutions as in equations (3.5), (3.6), the relation (2.2.28) leads to the key function

$$\eta(x) = 2\kappa + \omega x. \tag{3.1.3}$$

According to equation (3.2), and since the potential parameter κ and the wavenumber k in y-direction are equal in this case (see appendix A), the vector potential becomes $\mathbf{A}(x) = xB\mathbf{e}_y$, where $\omega = 2eB/c\hbar$. In turn, due to equation (3.3) the corresponding magnetic field $\mathbf{B}(x) = B\mathbf{e}_z$ is constant.

On the other hand, from equation (2.2.4) the SUSY partner potential of $V_0(x)$ is expressed as

$$V_2(x) = \frac{\omega^2}{4}\left(x + \frac{2\kappa}{\omega}\right)^2 + \frac{3\omega}{2}. \tag{3.1.4}$$

This and the initial potential are shape-invariant, because $V_2(x) = V_0(x) + 2\omega$. A plot of both potentials can be seen in Figure 3.1. The eigenfunctions and eigenvalues of $V_2(x)$ become

$$\psi_n^{(2)}(x) = c_n e^{-\frac{\zeta^2}{2}}\mathcal{H}_n(\zeta), \quad \mathcal{E}_n^{(2)} = (n+2)\omega. \tag{3.1.5}$$

Thus, from equation (3.7) the electron (hole) energies in bilayer graphene under a constant magnetic field are given by

$$E_{n-1} = \pm\frac{\hbar^2\omega}{2m}\sqrt{n(n-1)}. \tag{3.1.6}$$

Although the auxiliary potentials and their eigenfunctions depend on the wavenumber k, the energy eigenvalues (3.1.6) do not. Since the square-integrability of the eigenfunctions (3.1.2) and (3.1.5)

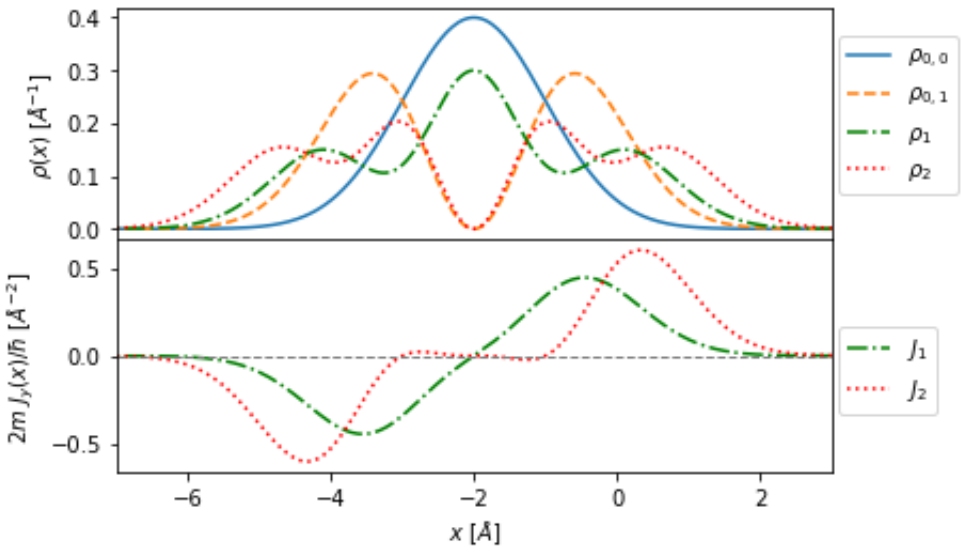

Figure 3.3: Probability (top) and current (bottom) densities for a constant magnetic field. The parameter values taken are $\omega = k = 1$. The ordering followed is the standard one, based on the spectrum of H_b.

does not impose any constraint on the parameters of the auxiliary potentials, the spectrum of H_b is infinite discrete, as can be seen in Figure 3.2 where the first electron energies as functions of k are shown. Furthermore, plots of the probability and current densities are displayed in Figure 3.3.

Section 3.2

Trigonometric Rosen-Morse potential

Let us consider now an initial trigonometric Rosen-Morse potential of the form

$$V_0(x) = \kappa^2 - D^2 + D(D-\mu)\csc^2 \mu x - 2D\kappa \cot \mu x, \tag{3.2.1}$$

where $0 < \mu x < \pi$. The corresponding eigenfunctions and eigenvalues are

$$\begin{aligned} \psi_n^{(0)}(x) &= c_n(-1)^{-(s_0+n)/2}\left(\zeta^2+1\right)^{-(s_0+n)/2} e^{a_0 \cdot \operatorname{arccot}(\zeta)} \mathcal{P}_n^{(-s_0-n-ia_0,-s_0-n+ia_0)}(i\zeta), \\ \mathcal{E}_n^{(0)} &= \kappa^2 - D^2 + (D+n\mu)^2 - \frac{\kappa^2 D^2}{(D+n\mu)^2}, \end{aligned} \tag{3.2.2}$$

with n being a non-negative integer, c_n is a normalization factor, $s_0 = D/\mu$, $a_0 = -\kappa D/\mu(D + n\mu)$, $\zeta = \cot \mu x$ and $\mathcal{P}_n^{(\alpha,\beta)}$ are the pseudo Jacobi polynomials. It is worth mentioning that there is an alternative expression for the eigenfunctions of the trigonometric Rosen-Morse potential in terms of real orthogonal polynomials of a real argument, see [Compean and Kirchbach, 2005]. Choosing the two factorization energies as indicated previously, equation (2.2.28) leads us to

$$\eta(x) = (2D+\mu)\left(\frac{\kappa}{D+\mu} - \cot \mu x\right), \tag{3.2.3}$$

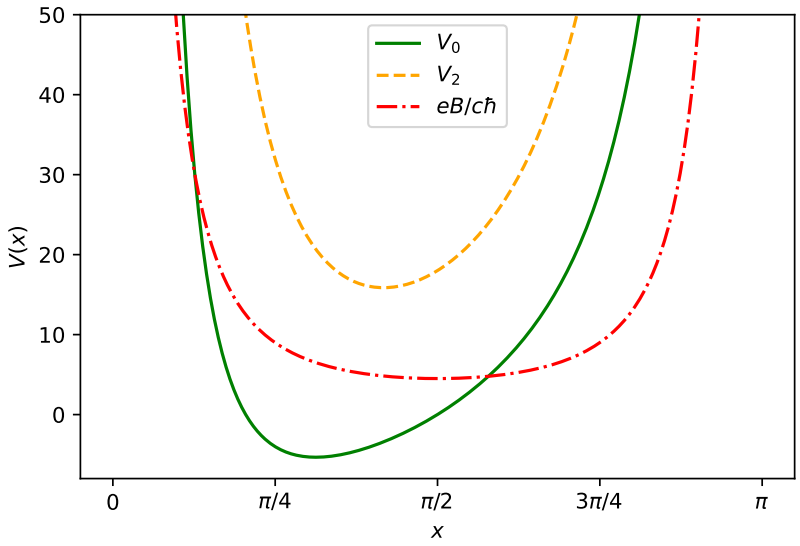

Figure 3.4: Trigonometric Rosen-Morse potential, its shape-invariant SUSY partner and the trigonometric singular well magnetic profile. The parameter values taken are $D = 4$, $k = 9/5$ and $\mu = 1$.

where in this case the potential parameter κ in terms of the wavenumber k is given by

$$\kappa = 2\left(\frac{D+\mu}{2D+\mu}\right)k. \tag{3.2.4}$$

We observe that $\kappa(k)$ is linear in k. Thus, the vector potential is written as $\mathbf{A}(x) = -(B/\mu)\cot\mu x\,\mathbf{e}_y$ with $D + \mu/2 = eB/c\hbar\mu$. The associated magnetic field becomes $\mathbf{B}(x) = B\csc^2\mu x\,\mathbf{e}_z$, with the magnetic profile $B(x)$ being known typically as trigonometric singular well.

Taking into account the function $\eta(x)$ in (3.2.3) and substituting it in equation (2.2.4) we get that

$$V_2(x) = \kappa^2 - D^2 + (D+2\mu)(D+\mu)\csc^2\mu x - 2D\kappa\cot\mu x. \tag{3.2.5}$$

The initial potential (3.2.1) and the latter one are shape-invariant potentials, since $V_2(x,\widetilde{D},\widetilde{\kappa}) = V_0(x,D,\kappa) + \mathcal{E}_2^{(0)}$, with $\widetilde{D} = D+2\mu$ and $\widetilde{\kappa} = D\kappa/(D+2\mu)$. A plot of these potentials is shown in Figure 3.4. It is important to stress that we can find in the literature the trigonometric Rosen-Morse potential expressed as $V(x) = A(A-1)\csc^2 x + 2B\cot x - A^2 + B^2/A^2$ [Gangopadhyaya et al., 2018]. Since, this potential admits bound states for both $B > 0$ and $B \leq 0$ [Junker, 2019], thus the potential worked out here is obtained by taking $B = -\kappa A$, and this selection is consistent with the theory developed in the previous chapters. Therefore, the eigenfunctions and eigenvalues of V_2 are given by

$$\begin{aligned}
\psi_n^{(2)}(x) &= c_n(-1)^{-(s_2+n)/2}\left(\zeta^2+1\right)^{-(s_2+n)/2} e^{a_2\cdot\operatorname{arccot}(\zeta)}\mathcal{P}_n^{(-s_2-n-ia_2,-s_2-n+ia_2)}(i\zeta),\\
\mathcal{E}_n^{(2)} &= \kappa^2 - D^2 + (D+2\mu+n\mu)^2 - \frac{\kappa^2 D^2}{(D+2\mu+n\mu)^2},
\end{aligned} \tag{3.2.6}$$

with $s_2 = s_0 + 2$ and $a_2 = -\kappa D/\mu(D+2\mu+n\mu)$.

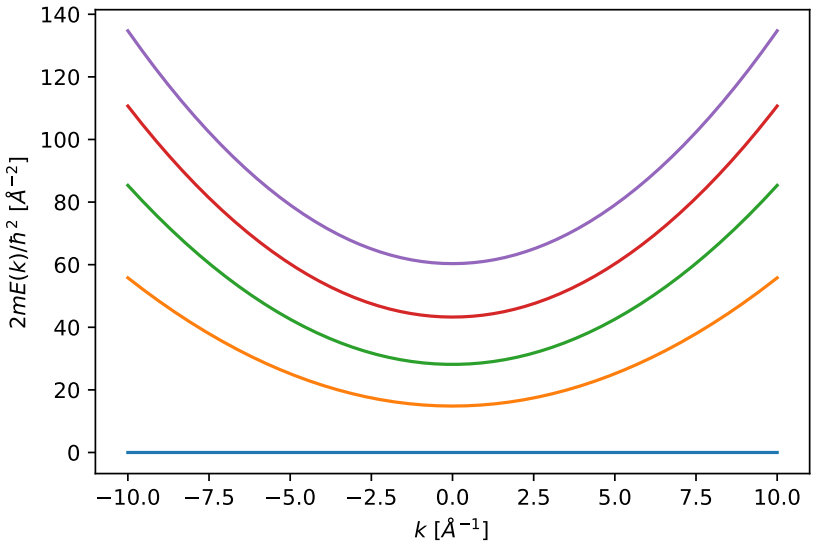

Figure 3.5: First electron energies for the trigonometric singular well magnetic profile as functions of k, with $D = 4$ and $\mu = 1$.

Consequently, the electron (hole) energies for bilayer graphene in the trigonometric singular well magnetic profile become

$$E_{n-1} = \pm\frac{\hbar^2}{2m}\left(\kappa^2 - D^2 + (D+n\mu)^2 - \frac{\kappa^2 D^2}{(D+n\mu)^2}\right)\sqrt{1 - \frac{\kappa^2 - D^2 + (D+\mu)^2 - \frac{\kappa^2 D^2}{(D+\mu)^2}}{\kappa^2 - D^2 + (D+n\mu)^2 - \frac{\kappa^2 D^2}{(D+n\mu)^2}}}. \tag{3.2.7}$$

The square-integrability requirement does not impose any constraints on the parameters involved. Thus, despite these eigenvalues depend on k this fact does not impose any restriction on the spectrum which is infinite discrete, as it is seen in Figure 3.5 where the first electron energies as functions of the wavenumber k are plotted. Finally, Figure 3.6 displays plots of the probability and current densities for some eigenvectors, associated to the lowest electron eigenenergies.

Section 3.3

Eckart potential

The last example of this chapter is the Eckart potential, which is expressed in terms of hyperbolic functions as follows

$$V_0(x) = \kappa^2 + D^2 + D(D-\mu)\operatorname{csch}^2\mu x - 2D\kappa\coth\mu x. \tag{3.3.1}$$

The corresponding eigenfunctions and eigenvalues are

$$\begin{aligned}\psi_n^{(0)}(x) &= c_n(\zeta-1)^{-(s_0+n-a_0)/2}(\zeta+1)^{-(s_0+n+a_0)/2}\mathcal{P}_n^{(-s_0-n+a_0,-s_0-n-a_0)}(\zeta),\\ \mathcal{E}_n^{(0)} &= \kappa^2 + D^2 - (D+n\mu)^2 - \frac{\kappa^2 D^2}{(D+n\mu)^2},\end{aligned} \tag{3.3.2}$$

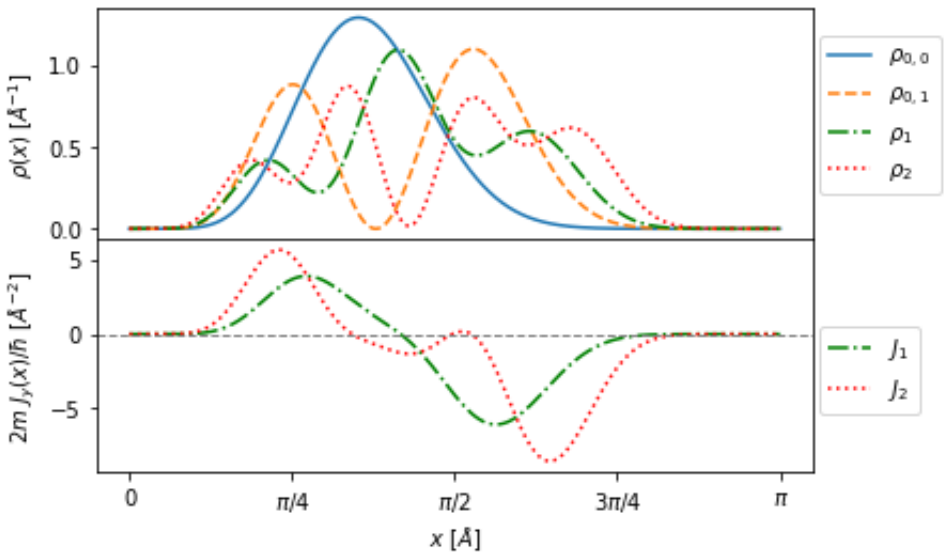

Figure 3.6: Probability (top) and current (bottom) densities for a trigonometric singular well magnetic profile. The parameter values taken are $D = 4$, $k = 9/5$ and $\mu = 1$. The ordering followed is the standard one for the spectrum of H_b.

where n is a non-negative integer, $s_0 = D/\mu$, $a_0 = \kappa D/\mu(D + n\mu)$, $\zeta = \coth \mu x$ and $\mathcal{P}_n^{(\alpha,\beta)}$ is a Jacobi polynomial. We choose now the factorization energies and seed solutions as in equations (3.5), (3.6) in order to obtain (see equation (2.2.28))

$$\eta(x) = (2D + \mu)\left(\frac{\kappa}{D + \mu} - \coth \mu x\right). \tag{3.3.3}$$

Analogously to the previous case, the potential parameter κ is a linear function of the wavenumber k, namely,

$$\kappa = 2\left(\frac{D + \mu}{2D + \mu}\right)k. \tag{3.3.4}$$

Thus, the vector potential turns out to be $\mathbf{A}(x) = -(B/\mu)\coth \mu x\, \mathbf{e}_y$ with $D + \mu/2 = eB/c\hbar\mu$. The corresponding magnetic field $\mathbf{B}(x) = B\mathrm{csch}^2 \mu x\, \mathbf{e}_z$ is called hyperbolic singular field.

The function $\eta(x)$ of equation (3.3.3) leads to the SUSY partner potential of $V_0(x)$:

$$V_2(x) = \kappa^2 + D^2 + (D + 2\mu)(D + \mu)\mathrm{csch}^2 \mu x - 2D\kappa \coth \mu x. \tag{3.3.5}$$

This potential and the initial one are shape-invariant, since $V_2(x, \widetilde{D}, \widetilde{\kappa}) = V_0(x, D, \kappa) + \mathcal{E}_2^{(0)}$, where $\widetilde{D} = D + 2\mu$, $\widetilde{\kappa} = \kappa D/(D + 2\mu)$. Plots of $V_0(x)$, $V_2(x)$ and the hyperbolic singular field are shown in Figure 3.7. The corresponding eigenfunctions and eigenvalues take the form,

$$\begin{aligned} \psi_n^{(2)}(x) &= c_n(\zeta - 1)^{-(s_2+n-a_2)/2}(\zeta + 1)^{-(s_2+n+a_2)/2}\mathcal{P}_n^{(-s_2-n+a_2,-s_2-n-a_2)}(\zeta), \\ \mathcal{E}_n^{(2)} &= \kappa^2 + D^2 - (D + 2\mu + n\mu)^2 - \frac{\kappa^2 D^2}{(D + 2\mu + n\mu)^2}, \end{aligned} \tag{3.3.6}$$

with $s_2 = s_0 + 2$ and $a_2 = \kappa D/\mu(D + 2\mu + n\mu)$.

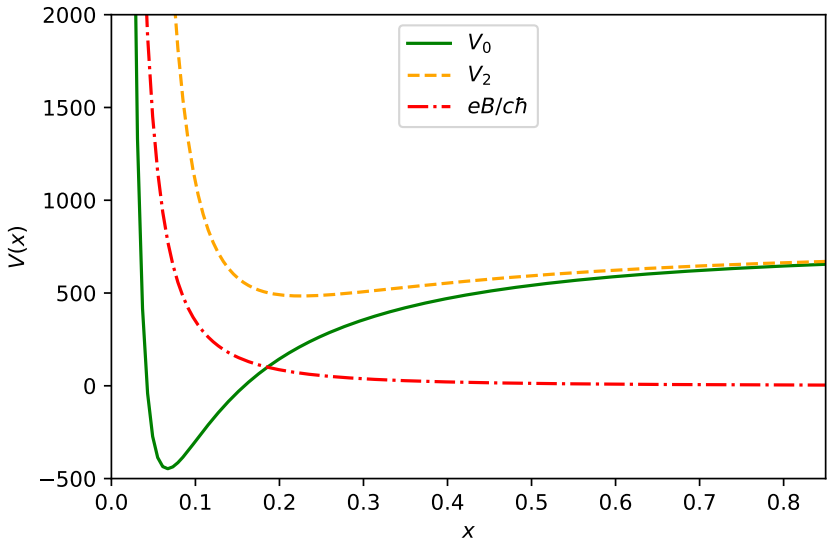

Figure 3.7: Eckart potential, its shape-invariant SUSY partner and the hyperbolic singular field. The parameter values taken are $D = 3$, $k = 105/4$ and $\mu = 1$.

Consequently, the electron (hole) energies for bilayer graphene in a hyperbolic singular field can be written as

$$E_{n-1} = \pm\frac{\hbar^2}{2m}\left(\kappa^2 + D^2 - (D+n\mu)^2 - \frac{\kappa^2 D^2}{(D+n\mu)^2}\right)\sqrt{1 - \frac{\kappa^2 + D^2 - (D+\mu)^2 - \frac{\kappa^2 D^2}{(D+\mu)^2}}{\kappa^2 + D^2 - (D+n\mu)^2 - \frac{\kappa^2 D^2}{(D+n\mu)^2}}}. \tag{3.3.7}$$

Unlike the previous examples, in this case the square-integrability requirement for the eigenfunctions $\psi_n^{(j)}$ constrains the potential parameters in the way $\kappa > D$. Furthermore, the exponent of the first factor in equations (3.3.2), (3.3.6) has to be positive while for the second factor it must be negative. Hence, if the above restrictions are fulfilled the spectrum of H_b is finite discrete, since the quantum number n has to satisfy that $\kappa > (D+n\mu)^2/D$. Figure 3.8 shows the lowest energies as functions of k; it is worth noting that an enveloping quadratic polynomial $\mathcal{E}(k) = ak^2 + bk + c$ appears, whose parameters a, b, c can be written in terms of the potential parameters as follows

$$a = 4D(D+\mu)/(2D+\mu)^2, \quad b = -2\mu - 4D^2/(2D+\mu), \quad c = D(D+\mu). \tag{3.3.8}$$

The first derivative of this polynomial, evaluated at the left end point of intersection with E_{n-1} is directly proportional to the group velocity in y-direction while the second derivative is related to the component $[M]_{2,2}$ of the effective mass tensor, i.e.,

$$\begin{aligned} v_g &= \frac{1}{\hbar}\frac{d\mathcal{E}(k)}{dk} = v_0^2\left(\frac{\hbar}{\gamma_1}\right)(2ak+b), \\ [M]_{2,2} &= \hbar^2\left(\frac{d^2\mathcal{E}(k)}{dk^2}\right)^{-1} = \frac{m}{a}. \end{aligned} \tag{3.3.9}$$

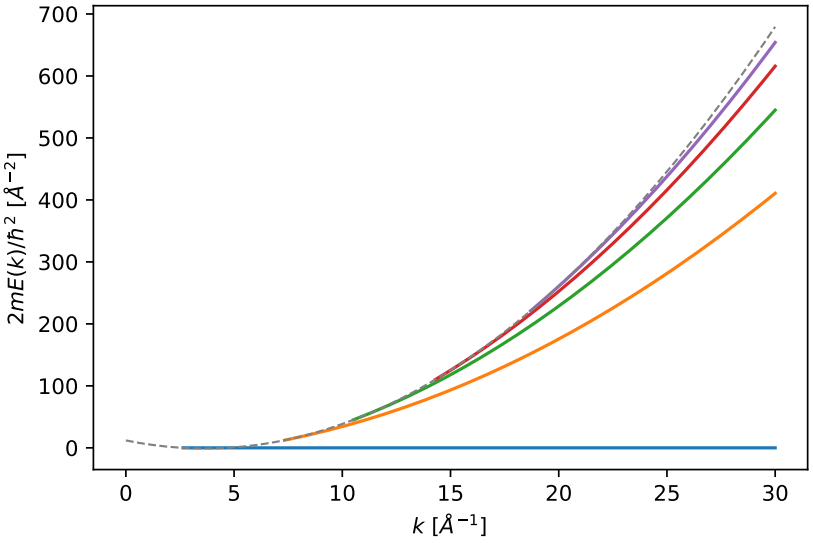

Figure 3.8: First electron energies as functions of k for the hyperbolic singular field with $D = 3$ and $\mu = 1$.

In Figure 3.9 it is displayed the probability and current densities for the two ground states and the first two excited states. These physical quantities have interesting properties that, together with some remarkable results, are going to be discussed in the next section.

Section 3.4

Discussion

We have addressed some examples where departing from an initial solvable potential, we have obtained a SUSY partner potential and a magnetic field, which allows us to find exact analytic solutions to the problem of an electron in bilayer graphene placed in the same magnetic field obtained earlier. Although from an experimental view point the resulting magnetic profiles do not seem to be easy to produce nowadays in the laboratory, in the literature there are experimental studies that can be considered as the first step for designing experiments involving graphene in the magnetic fields examined here, see also section 1.4.

As we mentioned at the beginning of this chapter, the ground state eigenvectors have an upper element equal to zero, see equation (3.7). This is due to the fact that the seed solutions lie in the *kernel* of the intertwining operator L_2^-, and since we choose them as the ground and the first excited state eigenfunctions of H_0, thus from equation (2.2.24) such result follows immediately.

Another interesting fact is the existence of two orthogonal zero energy states, namely, the double degeneracy of the ground state energy, which does not depend on the potential parameters, of the wavenumber in y-direction of the magnetic amplitude, provided that the momentum of the particle fulfils the low energy condition leading to the Hamiltonian (1.3.12). These zero energy states are very important for bilayer graphene, since in the low energy approximation two energy bands of graphene, one corresponding to electrons and the other to holes, touch each other at the

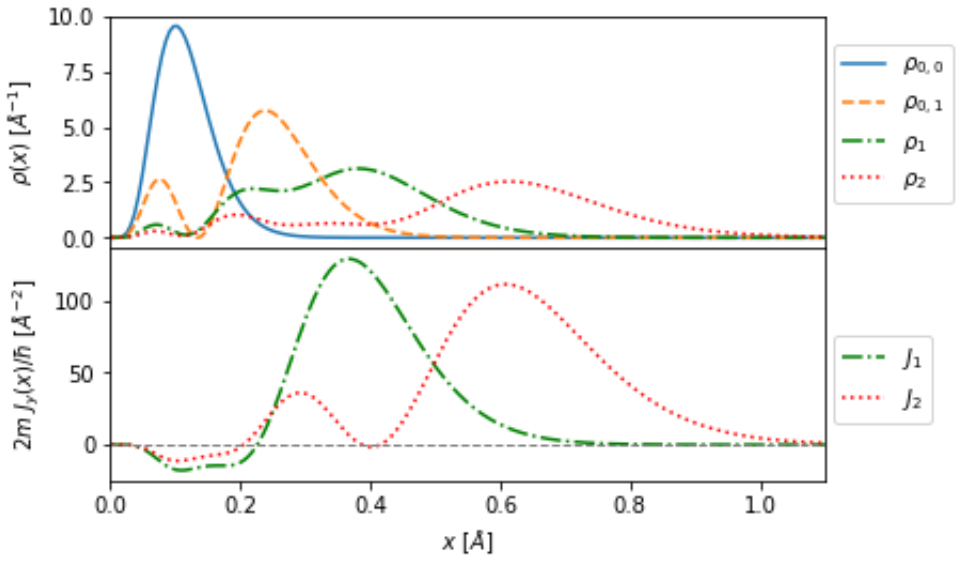

Figure 3.9: Probability (top) and current (bottom) densities for the hyperbolic singular field. The parameter values taken are $D = 3$, $k = 105/4$ and $\mu = 1$. The ordering followed is the standard one for the spectrum of H_b.

Dirac point, see Figure 1.8. Concerning the energy eigenvalues of the electron (hole), we can see that its principal quantum number $n - 1$ tells suggests us that the spectrum of the Hamiltonian H_b in equation (3.4) can be ordered in the standard way by simply introducing a new index $m = n-1, n \in \mathbb{N}$. Consequently, the energy eigenvalues, as well as the probability and current densities shown in this chapter follow the ordering given by m.

It is worth noting that, unlike monolayer graphene [Kuru et al., 2009], the magnetic field profile is not equal to the SUSY partner potential at any point inside its domain, thus there are not direct implications for the *'kinematical'* classical momentum $\pi_y = \hbar(k+(e/c)A)$, nor for the probability and current densities.

The enveloping quadratic curve for the energies of the Eckart potential divides the k-domain into two parts: to the right of the curve there are bound states while to the left they transform into scattering states whose group velocity is given by equation (3.3.9). Finally, we can see that the parameters of the enveloping curve depend on D and μ, so in the limit $D \to 0$ the group velocity is constant but the effective mass diverges, while if $D \gg \mu$ the group velocity keeps linear in k but the effective mass goes around m.

Chapter 4

Non-shape-invariant potentials: factorization energies as two consecutive levels

Here we shall generalize the algorithm for bilayer graphene of the previous chapter, taking advantage of the assumptions given at the beginning which guarantee the direct use of the second-order SUSY QM to solve the eigenvalue equation for the Hamiltonian H_b of equation (3.4). The factorization energies will be chosen now as two consecutive eigenvalues of H_0, i.e.,

$$\epsilon_1 = \mathcal{E}_{j+1}^{(0)}, \quad \epsilon_2 = \mathcal{E}_j^{(0)}. \tag{4.1}$$

Since when $j = 0$ this choice reduces to the shape-invariant case explored in the previous chapter and in [Fernández C. et al., 2020; Fernández C and Martínez-Moreno, 2020] (see equation (3.5)), from now on we will assume that $j \geq 1$. The corresponding seed solutions are chosen as

$$u_1(x) = \psi_{j+1}^{(0)}(x), \quad u_2(x) = \psi_j^{(0)}(x). \tag{4.2}$$

We are still working on the real case of the second-order SUSY QM developed in section 2.2, then the function $\eta(x)$ is calculated from equation (2.2.28), the corresponding magnetic field is obtained via (3.3) and the SUSY partner potential is determined from equation (2.2.4). Unlike the case with $j = 0$, this time the auxiliary potentials are not shape-invariant. However, we can get the eigenfunctions $\psi_n^{(2)}(x)$ of $V_2(x)$ through equation (2.2.24) while the functions $\psi_{\epsilon_\ell}^{(2)}(x)$ in (2.2.34) are not square-integrable. Hence, the spectrum of the Hamiltonian H_2 has two energy levels less than the spectrum of H_0. The eigenvectors of an electron (hole) in bilayer graphene in this case can be written as

$$\Psi_n(x,y) = \begin{cases} e^{iky}\begin{pmatrix} 0 \\ \psi_n^{(0)}(x) \end{pmatrix} & \text{for } n = j, j+1, \\ \frac{e^{iky}}{\sqrt{2}}\begin{pmatrix} \psi_n^{(2)}(x) \\ \psi_n^{(0)}(x) \end{pmatrix} & \text{for } n \neq j, j+1, \end{cases} \tag{4.3}$$

and the energy eigenvalues are

$$E_n = \pm\frac{\hbar^2}{2m}\sqrt{\left(\mathcal{E}_n^{(0)} - \mathcal{E}_j^{(0)}\right)\left(\mathcal{E}_n^{(0)} - \mathcal{E}_{j+1}^{(0)}\right)}, \tag{4.4}$$

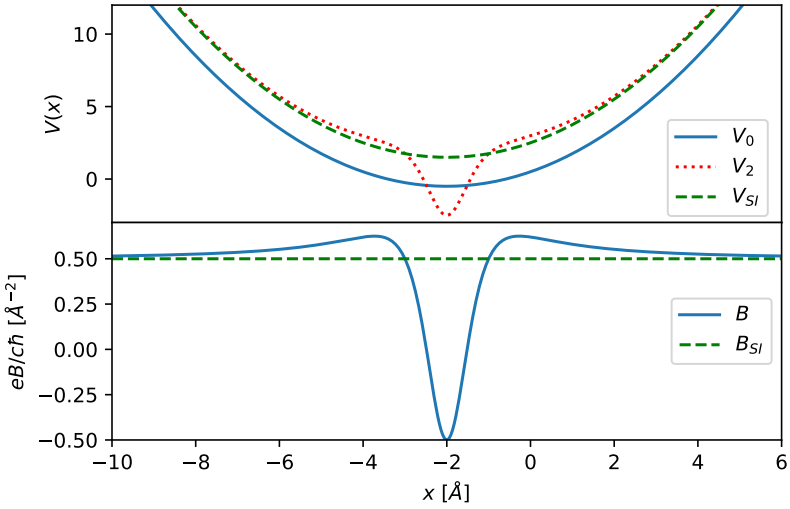

Figure 4.1: Supersymmetric partners of the harmonic oscillator potential, non-shape-invariant and shape-invariant ones (top). Magnetic field $B(x)$ of equation (4.1.1) and the corresponding one in the shape-invariant case (bottom). The parameters taken are $\omega = \kappa = 1$.

where n is a non-negative integer. It is important to stress that the index n supplies the standard ordering for the eigenvalues of the initial auxiliary Hamiltonian, namely, $\mathcal{E}_n^{(0)} < \mathcal{E}_{n+1}^{(0)}$. Nevertheless, this property is not inherited by the electron (hole) energies in equation (4.4), i.e., E_n is not necessarily less than E_{n+1}. It is still possible to determine the right index for getting the standard ordering of the spectrum of H_b, but it will depend in general on the election of j and the potential parameters.

In the next examples we shall fix $j = 1$, i.e., the factorization energies are chosen as the first and second excited state energies of H_0, and we will explore the way the magnetic field is deformed as compared with the corresponding shape-invariant case. The probability and current densities of equation (3.8) will be as well explored. All the parameters involved will be supposed to be positive, unless otherwise indicated.

Section 4.1

Shifted harmonic oscillator

Let us take the shifted harmonic oscillator of equation (3.1.1) as the initial potential, whose eigenfunctions and eigenvalues are given in equation (3.1.2). Choosing the factorization energies and corresponding seed solutions as in equations (4.1 - 4.2) with $j = 1$, the function $\eta(x)$ will be obtained straightforwardly, thus the SUSY partner potential $V_2(x)$ and the corresponding magnetic field turn out to be

$$\begin{aligned} V_2(x) &= V_{SI}(\zeta) + 4\omega \frac{2\zeta^2 - 1}{(2\zeta^2 + 1)^2}, \\ B(x) &= B_{SI}(\zeta) \left[1 + \frac{4\zeta^2 - 2}{(2\zeta^2 + 1)^2} \right], \end{aligned} \tag{4.1.1}$$

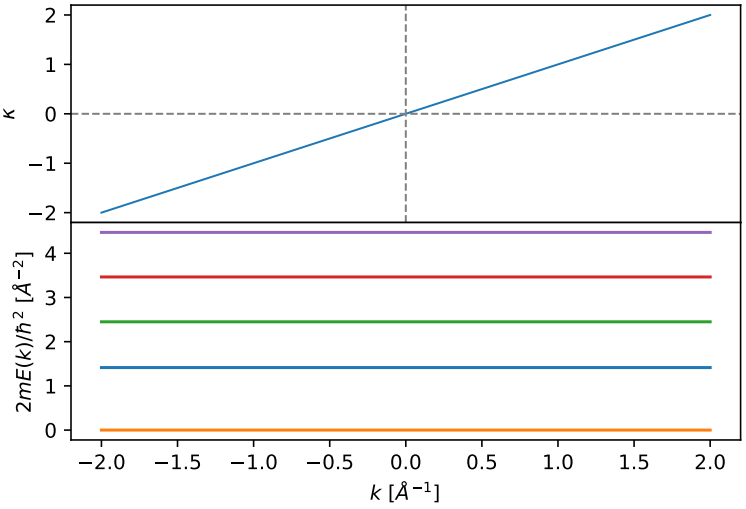

Figure 4.2: Parameter κ of the potential (top) and the first five electron energies (bottom) as functions of the wavenumber k for the shifted harmonic oscillator with $\omega = 1$.

where

$$V_{SI}(\zeta) = \frac{\omega}{2}\zeta^2 + \frac{3}{2}\omega,$$
$$B_{SI}(\zeta) = \frac{c\hbar\omega}{2e}, \tag{4.1.2}$$

with $\zeta = \sqrt{\omega/2}(x + 2\kappa/\omega)$. A plot of the potentials $V_0(x), V_2(x)$ and $V_{SI}(x)$ is displayed in Figure 4.1, which also shows $B(x)$ and $B_{SI}(x)$. It is important to remember that the potential parameter κ depends on the wavenumber k in y-direction in the way $\kappa = k$, see appendix A. A plot of this parameter κ as function of the wavenumber k is shown in Figure 4.2.

The electron (hole) energies in bilayer graphene under the magnetic field (4.1.1) turn out to be

$$E_n = \pm\frac{\hbar^2\omega}{2m}\sqrt{(n-1)(n-2)}, \tag{4.1.3}$$

with n being a non-negative integer. Once again, the energies E_n do not have the standard ordering that the auxiliary ones present. Nevertheless, in this case it is simple to determine the index that will define the standard ordering of the electron (holes) energies. Indeed, for an arbitrary j these energies are directly proportional to the square root of $(n-j)(n-j-1)$, and the first $j+1$ of them (for $n = j, \ldots, 0$) are doubly degenerate growing energies associated to the pairs of eigenvectors $\{(\Psi_j, \Psi_{j+1}), (\Psi_{j-1}, \Psi_{j+2}), \ldots, (\Psi_0, \Psi_{2j+1})\}$, where the first pair are the ground states, the second are the first exited states and so on until the j-th excited states. The remaining eigenstates of the Hamiltonian H_b constitute the set $\{\Psi_{2j+2}, \Psi_{2j+3}, \ldots\}$ associated to the non-degenerate electron (hole) energies $\{E_{2j+2}, E_{2j+3}, \ldots\}$, the first one being associated to the $(j+1)$-th excited state and so on. In particular, for the example worked here with $j = 1$ we have 2 twofold degenerate energy levels corresponding to the ground state $(n = 1, 2)$ and the first excited state $(n = 0, 3)$, which is remarkably different from the shape-invariant case where only the ground state energy

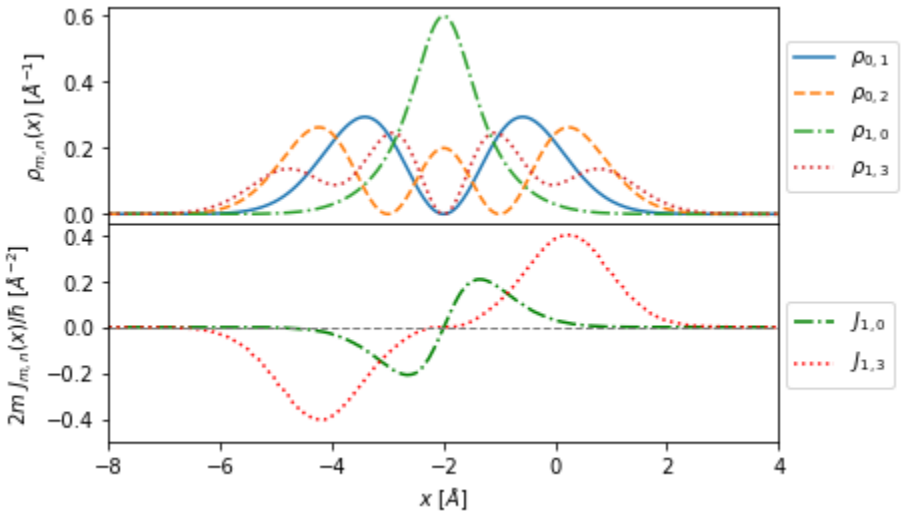

Figure 4.3: Probability densities (top) and currents in y-direction (bottom) as functions of x. The index m defines the standard ordering, while n is the quantum number for the initial harmonic oscillator potential. The parameters taken are $\omega = \kappa = 1$.

is twofold degenerate, see Figure 4.2. Finally, in Figure 4.3 the probability and current densities for several bound states are shown, with only currents in y-direction being displayed since in the x-direction they turn out to be zero.

Section 4.2

Trigonometric Rosen-Morse potential

The next example to be analyzed is the trigonometric Rosen-Morse potential of equation (3.2.1), whose eigenfunctions and eigenvalues are given in equation (3.2.2). We take the factorization energies as in equation (4.1) (see also [Domínguez-Hernández and Fernández C, 2011]), so the SUSY partner potential and corresponding magnetic field become

$$\begin{aligned} V_2(x) &= V_{SI}(\zeta) + 8\mu^2\left[\kappa^2 + (D+2\mu)^2\right] \\ &\times \frac{(1+\zeta^2)(D+\mu)(2D+3\mu)\zeta^2 - 2\kappa(2D+3\mu)\zeta + 2\kappa^2 - \mu(D+\mu)}{\left[(D+2\mu)(2D+3\mu)\zeta^2 - 2\kappa(2D+3\mu)\zeta 2\kappa^2 + \mu(D+2\mu)\right]^2}, \end{aligned} \tag{4.2.1}$$

$$\begin{aligned} B(x) &= B_{SI}(\zeta)\left[1 + 4\mu\frac{\kappa^2 + (D+2\mu)^2}{2D+\mu}\right. \\ &\left.\times \frac{(D+\mu)(2D+3\mu)\zeta^2 - 2\kappa(2D+3\mu)\zeta + 2\kappa^2 - \mu(D+\mu)}{\left[(D+2\mu)(2D+3\mu)\zeta^2 - 2\kappa(2D+3\mu)\zeta 2\kappa^2 + \mu(D+2\mu)\right]^2}\right], \end{aligned} \tag{4.2.2}$$

with

$$\begin{aligned} V_{SI}(\zeta) &= (D+\mu)(D+2\mu)(1+\zeta^2) - 2\kappa D\zeta - D^2 + \kappa^2, \\ B_{SI}(\zeta) &= \frac{c\hbar\mu}{2e}(2D+\mu)(1+\zeta^2), \end{aligned} \tag{4.2.3}$$

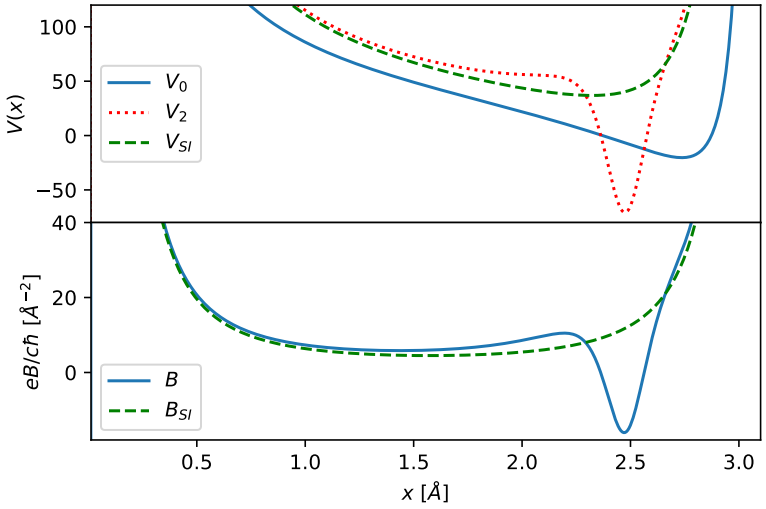

Figure 4.4: Supersymmetric partners of the trigonometric Rosen-Morse potential (top), non-shape-invariant and shape-invariant ones. Magnetic field $B(x)$ of equation (4.2.2) and the corresponding field in the shape-invariant case (bottom). The parameters taken are $D = 4$, $\kappa = -7$ and $\mu = 1$.

and $\zeta = \cot(\mu x)$. Figure 4.4 displays plots of the potentials $V_0(x), V_2(x), V_{SI}(x)$, and the magnetic fields $B(x), B_{SI}(x)$. In this case the wavenumber k is a rational function of the potential parameter κ, depending as well on the other parameters D, μ, namely,

$$k = \frac{\kappa(2D+3\mu)}{2(D+\mu)(D+2\mu)} \cdot \frac{(D+\mu)(D+2\mu)^2 - D\kappa^2}{(D+\mu)(D+2\mu) - \kappa^2}. \tag{4.2.4}$$

The electron (hole) energies for bilayer graphene in the magnetic field (4.2.2) are given by

$$\begin{aligned} E_n = \pm\frac{\hbar^2}{2m}\sqrt{(D+n\mu)^2 - \frac{\kappa^2 D^2}{(D+n\mu)^2} - (D+\mu)^2 + \frac{\kappa^2 D^2}{(D+\mu)^2}} \\ \times \sqrt{(D+n\mu)^2 - \frac{\kappa^2 D^2}{(D+n\mu)^2} - (D+2\mu)^2 + \frac{\kappa^2 D^2}{(D+2\mu)^2}}. \end{aligned} \tag{4.2.5}$$

Notice that such electron (hole) energies depend on κ, but this dependence does not imply any further restriction on them. The standard ordering for the spectrum of the Hamiltonian H_b in this case is more complicated to determine, because it depends on the potential parameters D, κ, μ and the selection of j. We must mention also that the ground state energy is always doubly degenerate. Furthermore, equation (4.2.4) leads to three solutions for $\kappa(k)$, see Figure 4.5. However, let us remember that in the low energy approximation the electron (hole) energy should be quadratic in the momentum [McCann and Koshino, 2013]. Taking this into account, the appropriate solutions $\kappa(k)$ leading to the right energies can be identified. In Figure 4.5 it is shown as well a plot of the first energies. The probability and current densities in y-direction are drawn in Figure 4.6 for the lowest bound states, since the currents along x-direction are zero.

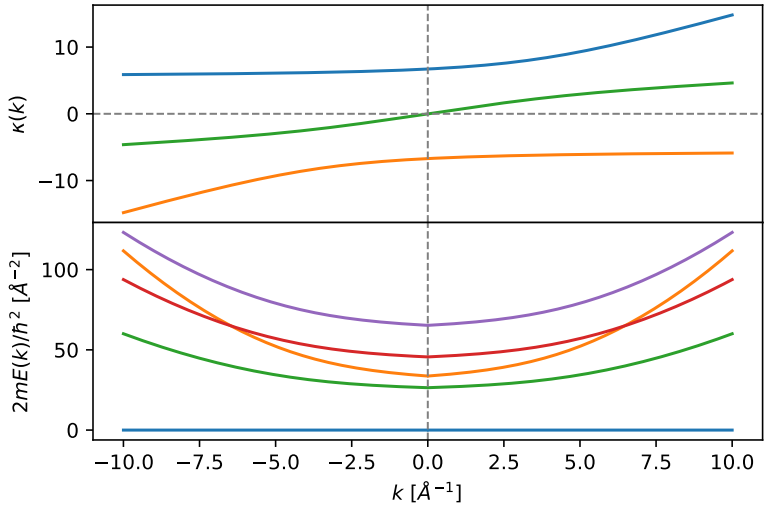

Figure 4.5: The three solutions of the parameter κ (top) and the first five electron energies (bottom) as functions of the wavenumber k for the trigonometric Rosen-Morse potential with $D = 4$, $\mu = 1$.

Section 4.3

Discussion

The selection of factorization energies as two consecutive energy levels of $Sp\,(H_0)$, in particular the examples worked in this chapter with the first and second excited state energies, produces non-shape-invariant SUSY partner potentials and non-trivial magnetic fields. It is important to analyse now the dependency of these magnetic fields on the wavenumber k in y-direction. Thus, since from the very beginning of the algorithm construction for bilayer graphene k is fixed, the exact solutions to the eigenvalue problem and the magnetic fields found here will depend on k, which means that if this parameter changes the eigenvectors $\Psi_n(x, y)$, the energy eigenvalues E_n and the magnetic profiles $B(x)$ will accordingly change.

On the other hand, some of the electron (hole) energies could be twofold degenerate. This degeneracy depends on the potential parameters and j. However, in some special cases, as for the harmonic oscillator potential of section 4.1, there exist $j + 1$ doubly degenerate eigenvalues, and this fact does not depend neither on ω nor on k, but only on j. In other cases, as for the trigonometric Rosen-Morse potential, there is only one doubly degenerate eigenvalue, namely, the ground state energy. It must be said that the dependency of E_n on k in this case causes that for $n < j$ these eigenvalues show a rate of increase with respect to k which is bigger than the corresponding rate for $n > j + 1$. In the example of section 4.2 the energy for $n = 0$ displays such a behavior (see Figure 4.5), thus as the absolute value of k increases the eigenvalue that close $k = 0$ was the second excited energy level can become greater than or equal to the subsequent energy levels. Hence, the standard ordering of the spectrum of H_b can be modified, by changing the potential parameters and j. To make clear this point, we show a plot of the energies E_n versus the index n for the harmonic oscillator with $j = 1$ in Figure 4.7; it can be seen that the ground state energy corresponds to $n = 1, 2$, while the first excited energy level corresponds to $n = 0, 3$,

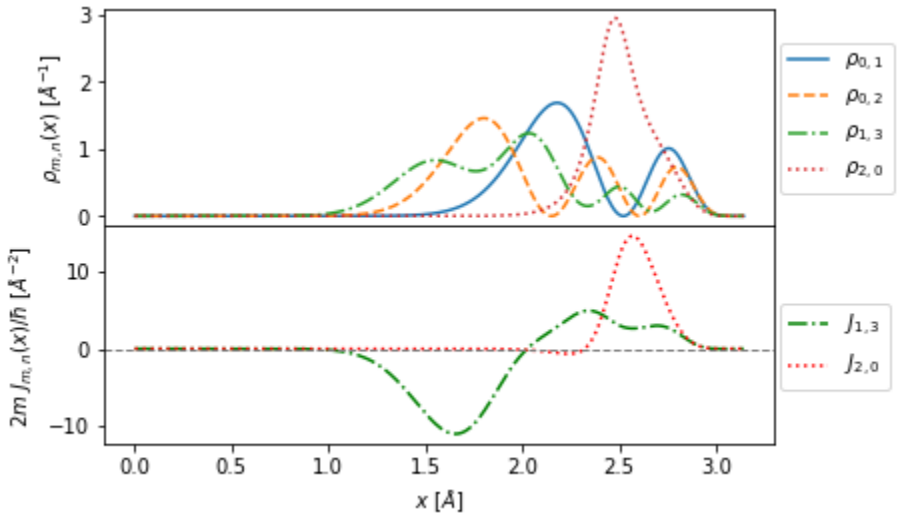

Figure 4.6: Probability densities (top) and currents in y-direction (bottom). The index m defines the standard ordering, while n is the quantum number for the trigonometric Rosen-Morse potential. The parameters taken are $D = 4$, $\kappa = -7$ and $\mu = 1$.

the second excited energy level to $n = 4$ and so on. In other words, the new index m leading to the standard ordering of the electron (holes) energies in this case is

$$m = \begin{cases} 0, & \text{for } n = 1, 2, \\ 1, & \text{for } n = 0, 3, \\ n - 2, & \text{for } n \geq 4. \end{cases} \tag{4.3.1}$$

On the other hand, for the trigonometric Rosen-Morse potential the corresponding energy plot versus the index n appears in Figure 4.8, with the same parameter values used in the plots of section 4.2. We can see that for $n = 1, 2$ we get the ground state energy, for $n = 3$ the first excited energy level, for $n = 0$ the second excited energy level and for $n \geq 4$ the $n - 1$ excited energy level. It is worth noting that if we change the value of k, for example to 9, the levels corresponding to $n = 0, 4$ change their order: the level for $n = 4$ becomes the second excited energy and the level for $n = 0$ becomes the third excited energy.

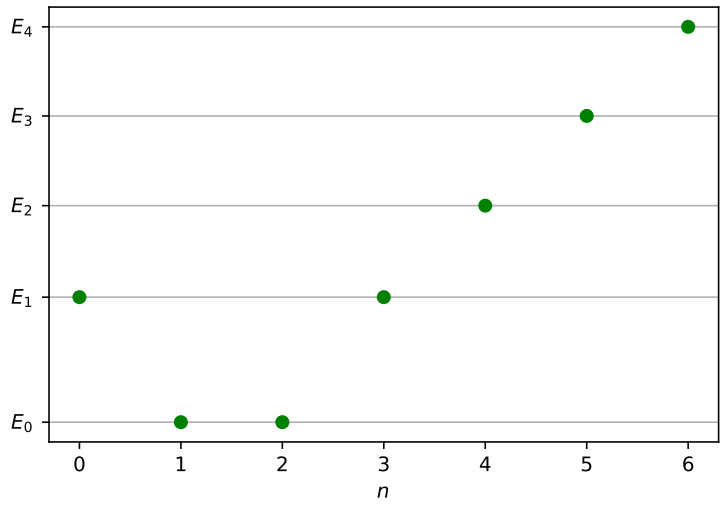

Figure 4.7: First electron energies for the shifted harmonic oscillator potential: the index n defines the standard ordering of $Sp(H_0)$. It can be seen the twofold degeneracy of the ground and the first exited state energy. The parameters taken are $\omega = \kappa = 1$.

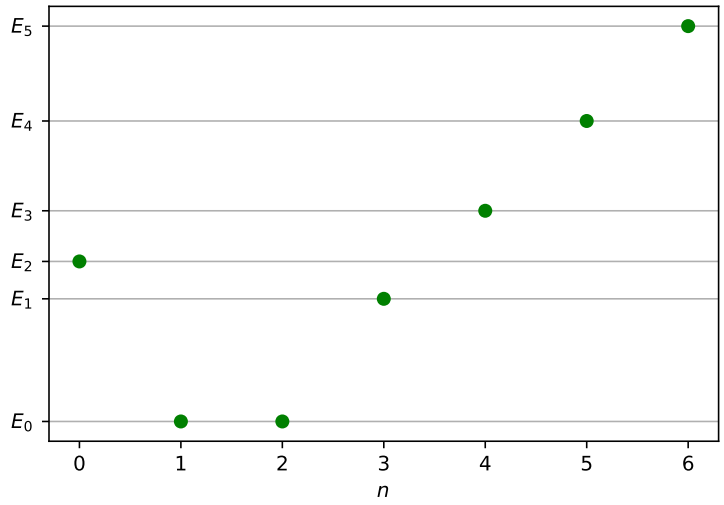

Figure 4.8: First electron energies for the trigonometric Rosen-Morse potential: the index n defines the standard ordering of $Sp(H_0)$. It can be seen the twofold degeneracy of the ground state energy. The parameters taken are $D = 4$, $\kappa = -7$ and $\mu = 1$.

Chapter 5

Non-shape-invariant potentials: confluent algorithm

The characteristic feature of the confluent algorithm is that both factorization energies are equal, i.e., $\epsilon_1 = \epsilon_2 = \epsilon$ [Fernández C and Salinas-Hernández, 2003; Fernández C. and Salinas-Hernández, 2005]. Then, there is a unique seed solution $u(x)$ of the Schrödinger equation for the initial Hamiltonian H_0, [Fernández C and Roy, 2020], see also [Bermudez, 2016; Bermudez et al., 2012; Contreras-Astorga and Schulze-Halberg, 2015a,b, 2017; Correa et al., 2015; Fernández C and Salinas-Hernández, 2011; Grandati and Quesne, 2015; Mielnik et al., 2000; Schulze-Halberg and Yesiltas, 2018]. In this chapter we will apply this algorithm to bilayer graphene, taking into account the assumptions given at the beginning of chapter 3. In particular, we will take the factorization energy as one of the bound state energies of the initial potential, namely,

$$\epsilon = \mathcal{E}_j^{(0)}, \tag{5.1}$$

with j being a non-negative integer. The seed solution chosen will be the corresponding eigenfunction of H_0, namely,

$$u(x) = \psi_j^{(0)}(x). \tag{5.2}$$

The key function $\eta(x, \omega_0)$ is calculated from equation (2.2.41), the magnetic field $B(x; \omega_0)$ is generated from equation (3.3) and the supersymmetric partner potential $V_2(x; \omega_0)$ is obtained via the first equation (2.2.4), forming one-parametric families of functions characterized by ω_0. It is convenient to express the last equation as follows

$$V_2(x; \omega_0) = V_0(x; \omega_0) + 4\frac{e}{c\hbar}B(x; \omega_0). \tag{5.3}$$

The eigenfunction $\psi_\epsilon^{(2)}(x)$ in equation (2.2.42) will be square-integrable if the parameter ω_0 lies in the intervals $\omega_0 > 1$ or $\omega_0 < 0$, while for $\omega_0 = 0$ or $\omega_0 = 1$ it will not be square-integrable anymore. Therefore, we get two different cases: one in which the spectra of both auxiliary Hamiltonians are equal, so the eigenvectors of the graphene Hamiltonian H_b are

$$\Psi_n(x, y) = \frac{e^{iky}}{\sqrt{2}} \begin{pmatrix} \psi_n^{(2)}(x) \\ \psi_n^{(0)}(x) \end{pmatrix}, \tag{5.4}$$

with n being a non-negative integer. The other case is such that the supersymmetric partner Hamiltonian H_2 has an energy level less than the initial Hamiltonian H_0. Thus, the eigenvectors

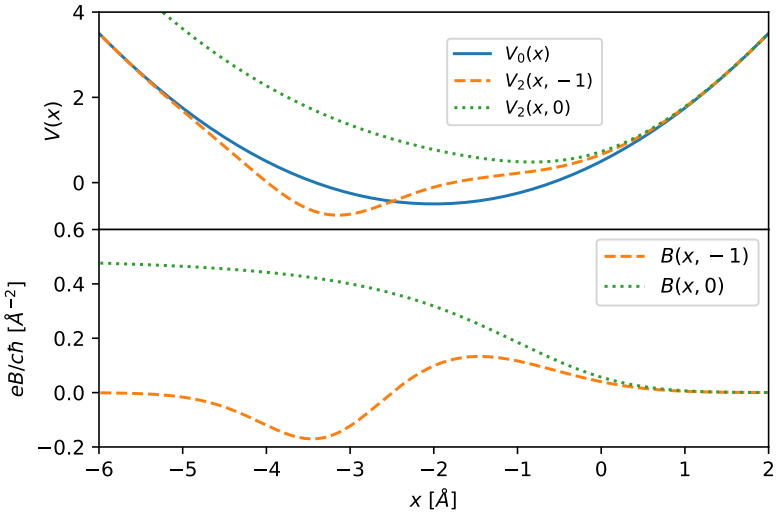

Figure 5.1: Confluent SUSY partners of the shifted harmonic oscillator in the isospectral case $V_2(x;-1)$ and in the limit case $V_2(x;0)$ (top). Associated magnetic fields in both cases (bottom). The parameters were taken as $\omega = \kappa = 1$.

$\Psi_n(x,y)$ are now given by

$$\Psi_n(x,y) = \begin{cases} e^{iky}\begin{pmatrix} 0 \\ \psi_n^{(0)}(x) \end{pmatrix}, & \text{for } n = j, \\ \frac{e^{iky}}{\sqrt{2}}\begin{pmatrix} \psi_n^{(2)}(x) \\ \psi_n^{(0)}(x) \end{pmatrix}, & \text{for } n \neq j. \end{cases} \tag{5.5}$$

In both cases the eigenvalues of the electron (hole) in bilayer graphene turn out to be

$$E_n = \pm\frac{\hbar^2}{2m}\left|\mathcal{E}_n^{(0)} - \mathcal{E}_j^{(0)}\right|. \tag{5.6}$$

Once again, the index n does not supply in general the standard ordering of the spectrum of H_b. However, unlike the two previous cases, the two consecutive levels and in the shape-invariant case, now the ground state energy is non-degenerate. In the next examples we shall calculate the key integral of the function $\mathrm{w}(x)$ for an arbitrary j, but for making plots and some other calculations we will take $j = 0$.

Section 5.1

Shifted harmonic oscillator

The first example to be addressed is the harmonic oscillator potential of equation (3.1.1), whose eigenfunctions and eigenvalues are given in equation (3.1.2). By choosing the factorization energy as $\epsilon = \mathcal{E}_j^{(0)}$ and the seed solution as the corresponding eigenfunction of H_0, the integral in $\mathrm{w}(x)$ becomes

$$\int_{-\infty}^{x}\left[\psi_j^{(0)}(y)\right]^2 dy = \frac{I_j(x)}{I_j(x\to\infty)}. \tag{5.1.1}$$

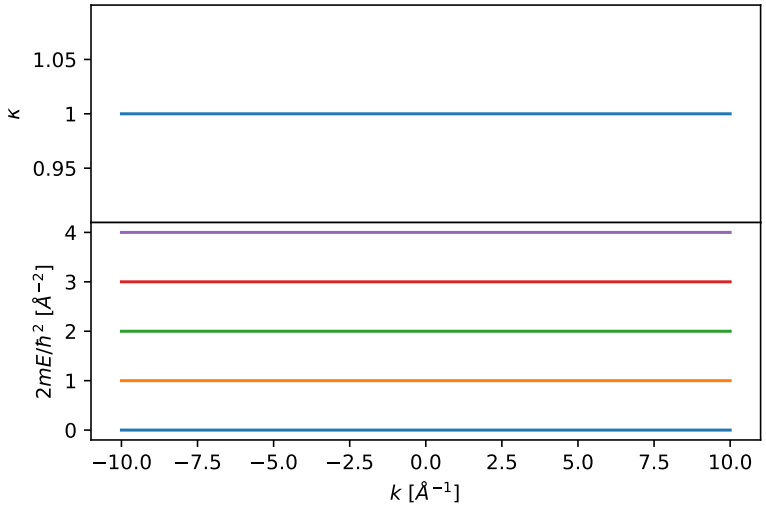

Figure 5.2: Potential parameter κ (top) and first electron energies for bilayer graphene (bottom) as functions of the wavenumber k in the confluent case for the shifted harmonic oscillator potential with $\omega = 1$.

Since the eigenfunction $\psi_j^{(0)}(x)$ is normalized, the function $I(x)$ evaluated in the limit $x \to \infty$ is the square of the normalization factor of that eigenfunction. Thus, we have

$$I_j(x) = \sum_{l,m=0}^{\lfloor \frac{j}{2} \rfloor} \frac{(-1)^{m+l} 2^{2*(j-m-l)-1}}{m!l!(j-2m)!(j-2l)!} \begin{cases} \Gamma\left(j-m-l+\frac{1}{2}\right) + \gamma\left(j-m-l+\frac{1}{2}, \zeta^2\right), & \zeta \geq 0, \\ \Gamma\left(j-m-l+\frac{1}{2}\right) - \gamma\left(j-m-l+\frac{1}{2}, \zeta^2\right), & \zeta < 0, \end{cases} \tag{5.1.2}$$

with $\lfloor x \rfloor$ being the floor function, $\Gamma(x)$ the gamma function, $\gamma(s,x)$ the lower incomplete gamma function and $\zeta = \sqrt{\omega/2}(x + 2\kappa/\omega)$. In terms of j the function $I_j(x)$ in the limit $x \to \infty$ reduces to

$$I_j(x \to \infty) = \sum_{l,m=0}^{\lfloor \frac{j}{2} \rfloor} \frac{(-1)^{m+l} 2^{2(j-m-l)}}{m!l!(j-2m)!(j-2l)!} \Gamma\left(j-m-l+\frac{1}{2}\right). \tag{5.1.3}$$

From equation (5.1.1) we can calculate $\eta(x;\omega_0)$ via equation (2.2.41) with $j = 0$, and then the magnetic field $B(x;\omega_0)$ through equation (3.3), which leads to

$$B(x;\omega_0) = \frac{c\hbar\omega}{e} \left\{ \frac{e^{-2\zeta^2}}{\pi[\mathrm{erfc}(\zeta) - 2 + 2\omega_0]^2} - \frac{\zeta e^{-2\zeta^2}}{\sqrt{\pi}[\mathrm{erfc}(\zeta) - 2 + 2\omega_0]^2} \right\}, \tag{5.1.4}$$

where $\mathrm{erfc}(x)$ is the complementary error function. The SUSY partner potential $V_2(x;\omega_0)$ is gotten using equation (5.3). Figure 5.1 shows plots of the SUSY partner potential of V_0 for two different values of the parameter ω_0, -1 and 0, as well as the corresponding magnetic field in each case.

The electron (hole) energies for bilayer graphene under the magnetic field (5.1.4) take the form

$$E_n = \frac{\hbar^2\omega}{2m} n, \tag{5.1.5}$$

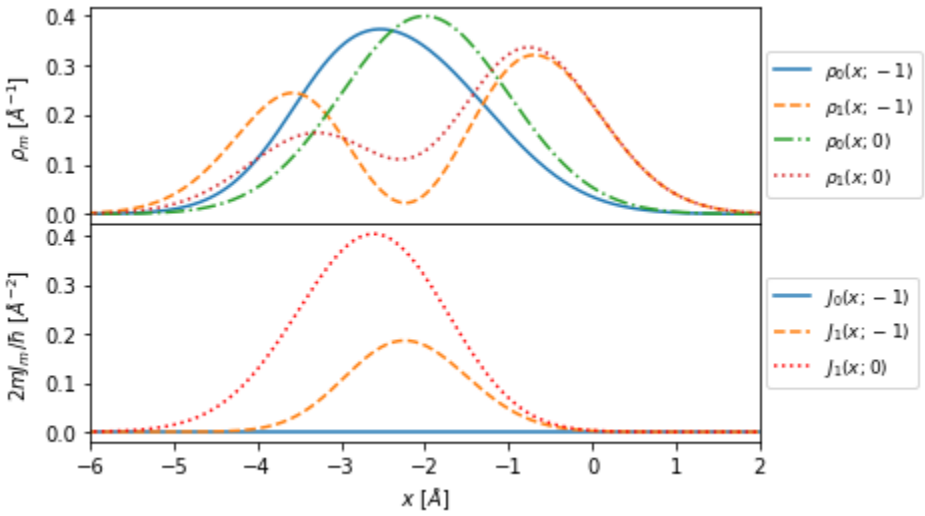

Figure 5.3: Probability densities (top) and currents in y-direction (bottom) for some eigenstates of the bilayer graphene Hamiltonian H_b in the case of the shifted harmonic oscillator. The index m supplies the standard ordering for the spectrum of H_b. The parameters were chosen as $\omega = \kappa = 1$.

with n being a non-negative integer. Notice that these electron (hole) energies are equidistant, which is similar to what happens for the eigenvalues (3.1.2) of the auxiliary initial Hamiltonian. Moreover, since the factorization energy was chosen as the ground state energy of H_0, all these eiegenvalues are non-degenerate. Nevertheless, if we would take $j \geq 1$ the first j excited state energies would be doubly degenerate. Note also that, if we follow the procedure described in appendix A, we can find that in this case the potential parameter κ does not depend on the wavenumber k. Hence, the energies E_n do not depend neither on κ nor on k, see Figure 5.2. Lastly, the probability densities and currents are drawn in Figure 5.3, where only the currents in y-direction are displayed since in x-direction they vanish.

Section 5.2

Trigonometric Rosen-Morse potential

Let us consider now the trigonometric Rosen-Morse potential (3.2.1), whose eigenfunctions and eigenvalues are given in equation (3.2.2). Taking the factorization energy (5.1), the integral in w(x) can be written as in equation (5.1.1), but now the function $I_j(x)$ is not a piecewise continuous function as for the shifted harmonic oscillator but rather a continuous function in the full domain. It is expressed in terms of the hypergeometric function, the gamma function and some periodic

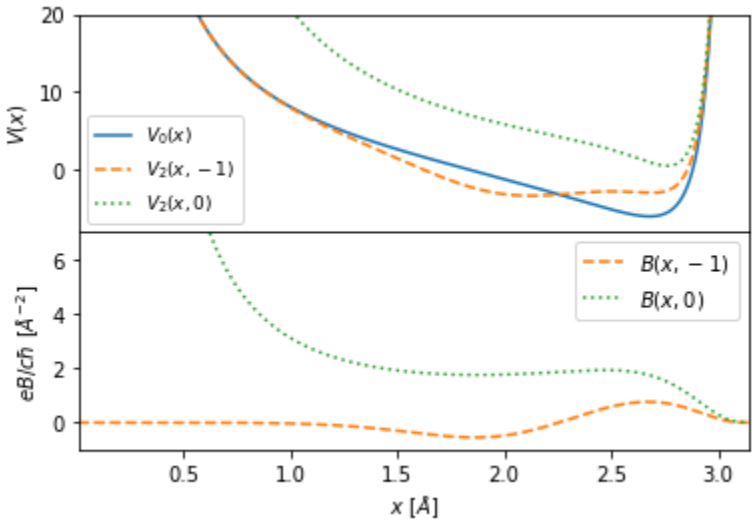

Figure 5.4: Confluent supersymmetric partners for the trigonometric Rosen-Morse potential in the isospectral case $V_2(x;-1)$ and in the limit case $V_2(x;0)$ (top). Associated magnetic fields in both cases (bottom). The parameters were taken as $D=2$, $\kappa=-2$ and $\mu=1$.

functions, as can be seen in the result

$$\begin{aligned} I_j(x) = \sum_{l,m=0}^{j} (-1)^{m+l} \binom{j}{m}\binom{j}{l} \frac{(l+q-p+j)_l (l+q-p+j)_m}{\Gamma(l+1-p)\Gamma(m+1-p)} \\ \times \Big[e^{-i\frac{p+q}{2}[\pi-2\theta(x)]} e^{-i(p-q)\theta(x)}\, {}_2F_1\left(q, m+l+q-p; 1+q; -e^{i2\theta(x)}\right) \\ - \frac{\Gamma(1+q)\Gamma(p-q-m-l+1)}{\Gamma(p+1-m-l)} e^{-i\frac{p-q}{2}\pi} \Big], \end{aligned} \tag{5.2.1}$$

where $p = s+j+ia_j$, $q=-s-j+ia_j$, $s=D/\mu$, $a_j=-\kappa D/\mu(D+j\mu)$, $\theta(x)=\arctan(\cot(\mu x))$ and ${}_2F_1(a,b;c;x)$ is the hypergeometric function. In the limit $x\to\infty$ the function $I_j(x)$ tends to

$$\begin{aligned} I_j(x\to\infty) = \sum_{l,m=0}^{j} (-1)^{l+m} \binom{j}{l}\binom{j}{m} \frac{(1+q-p+j)_l (1+q-p+j)_m}{\Gamma(l+1-p)\Gamma(m+1-p)} \\ \times \frac{\Gamma(1+q)\Gamma(p-q+1-l-m)}{\Gamma(p+1-m-l)} \left(e^{-i(p+q)\pi} e^{i\frac{p-q}{2}\pi} - e^{-i\frac{p-q}{2}\pi} \right). \end{aligned} \tag{5.2.2}$$

Similarly to the previous case, from equations (2.2.41), (5.1.1) we can calculate $\eta(x;\omega_0)$, but substituting now the corresponding function $I_j(x)$ (5.2.1) and its limit (5.2.2). The magnetic field

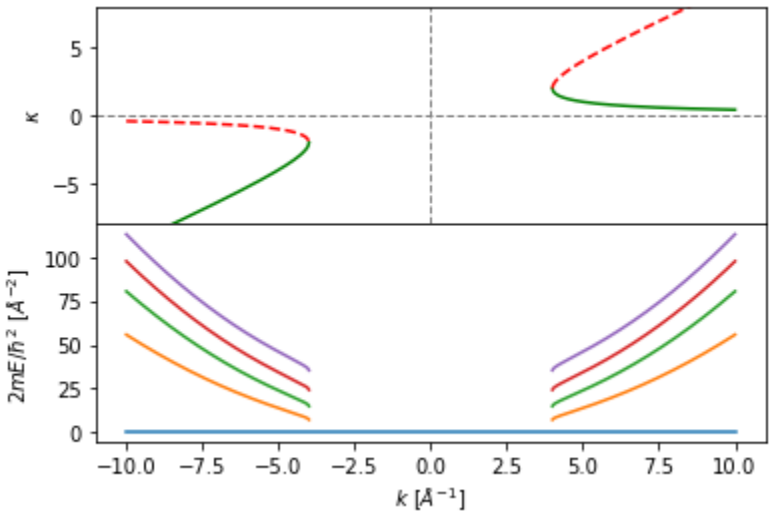

Figure 5.5: Potential parameter κ (top) and first electron energies for bilayer graphene (bottom) as functions of the wavenumber k in the confluent case for the trigonometric Rosen-Morse potential with $D = 2$ and $\mu = 1$.

$B(x;\omega_0)$ is determined from equation (3.3) for $j = 0$, which can be written as

$$\begin{aligned} B(x;\omega_0) = &-2q\frac{c\hbar}{e}\mu^2\Gamma(1+p)\left(1+e^{i2\theta(x)}\right)^{p-q}\left\{\left[\Gamma(1+q)\Gamma(p-q+1)\right.\right. \\ &\times\left[1-i2\omega_0\sin(q\pi)\right]e^{-i2q\theta(x)} - \Gamma(1+p)\,{}_2F_1\left(q,q-p;1+q;e^{-i2\mu x}\right)\Big]^{-2} \\ &\times\left[q\Gamma(1+p)\left(\left(1-e^{-i2\mu x}\right)^{p-q} - {}_2F_1\left(q,q-p;1+q;e^{-i2\mu x}\right)\right) - \frac{p-q}{1+e^{-i2\theta(x)}}\right. \\ &\times\left(\Gamma(1+p)\,{}_2F_1\left(q,q-p;1+q;e^{-i2\mu x}\right) - \Gamma(p-q+1)\Gamma(1+q)\right. \\ &\left.\times\left[1-i2\omega_0\sin(q\pi)\right]e^{-i2q\theta(x)}\right) \\ &\left.\left.+\,q\Gamma(p-q+1)\Gamma(1+q)\left[1-i2\omega_0\sin(q\pi)\right]e^{-i2q\theta(x)}\right]\right\}. \end{aligned} \tag{5.2.3}$$

The non-shape-invariant SUSY partner potentials of $V_0(x)$ in two cases, for $\omega_0 = -1$ and $\omega_0 = 0$, are shown in Figure 5.4, as well as the corresponding magnetic fields.

For these magnetic fields the electron (holes) energies for bilayer graphene are given by

$$E_n = \pm\frac{\hbar^2}{2m}\left[\kappa^2 - D^2 + (D+n\mu)^2 - \frac{\kappa^2 D^2}{(D+n\mu)^2}\right]. \tag{5.2.4}$$

Up to a factor, these energies are equal to the corresponding ones for the auxiliary potential (3.1.1). Unlike the harmonic oscillator case, however, now there are not degenerate energy eigenvalues (see Figure 5.5). Furthermore, a dependence of the electron (hole) energies on the wavenumber k appears, due to the fact that κ and k are now related as follows

$$k = \kappa + \frac{4}{\kappa}. \tag{5.2.5}$$

It is worth noticing that this equation is valid only for $D = 2$ and $\mu = 1$, since the calculation for arbitrary values of these parameters is difficult, see appendix A. By solving the previous

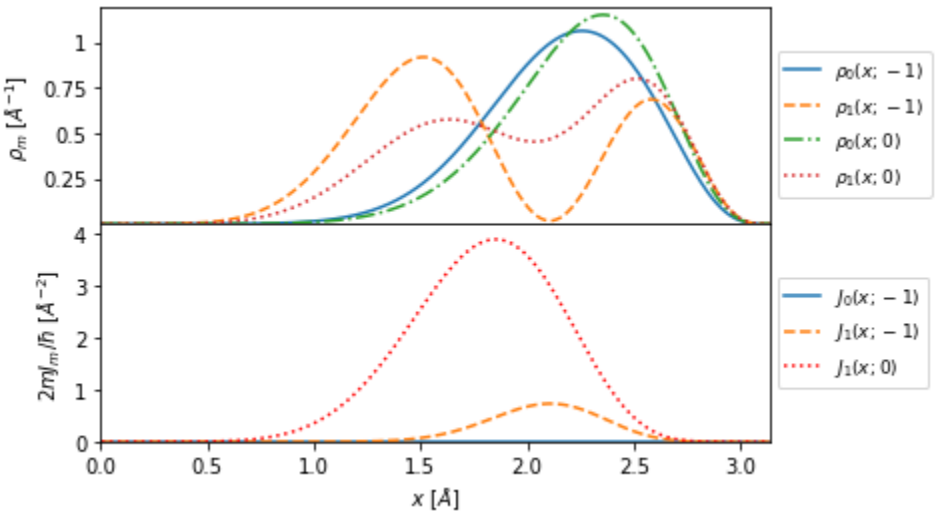

Figure 5.6: Probability densities (top) and currents in y-direction (bottom) for some eigenstates of the bilayer graphene Hamiltonian H_b in the case of the trigonometric Rosen-Morse potential. The index m supplies the standard ordering for the spectrum of H_b. The parameters were chosen as $D = 2$, $\kappa = -2$ and $\mu = 1$.

equation for $\kappa(k)$, two different solutions will be obtained (see Figure 5.5). Even though both are mathematically correct, physically the electron energies (5.2.4) must depend on each of these solutions in a way that the quadratic dependence in the momentum remains valid. Consequently, only in the domain $(-4, 4)$ the ground state exists. Finally, the probability and currents densities for some eigenfunctions are plotted in Figure 5.6. Since in x-direction the current becomes zero, we show only the currents along y-direction.

Section 5.3

Discussion

The confluent algorithm produces quite interesting results, since it cannot be seen in general as the iteration of two non-singular first-order SUSY transformations. One of them is the fact that the magnetic field (5.1.4) for the harmonic oscillator potential is independent of the wavenumber k, so we can modify k but $B(x;\omega_0)$ remains unchanged. Since the eigenvectors $\Psi_n(x, y)$ and eigenvalues E_n of the bilayer graphene Hamiltonian H_b neither depend on k, in this case the electron motion in x-direction is independent of the motion along y-direction, in contrast to what happens for any other example of this and the previous chapters.

As we mentioned at section 5.1, in the harmonic oscillator case there are j twofold degenerate energy eigenvalues, namely, the first j excited energies. However, unlike all previous cases, where the zero energy was twofold degenerate, the ground state energy is now non-degenerate. This means that only one particle can be placed in such energy, contrary to the case when deleting two consecutive levels where two particles can be placed in the zero energy at the same time. Similarly, when the results for the trigonometric Rosen-Morse potential are analyzed we see that the ground state energy is non-degenerate, no matter the parameter values taken nor the factorization energy choice. It is still possible to get degeneracy for some excited state energies, by selecting exceptional

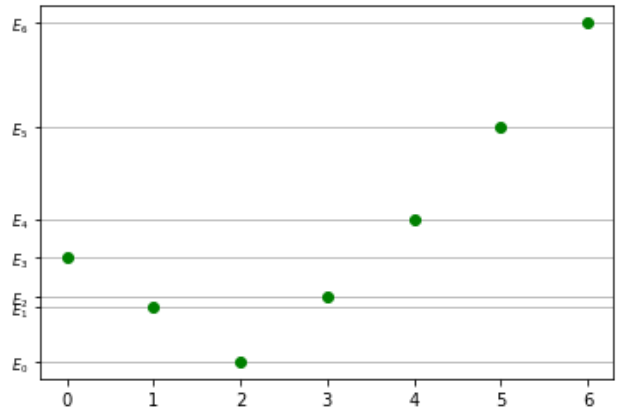

Figure 5.7: Electron energy levels versus the index n labelling the eigenvalues of H_0 for the trigonometric Rosen-Morse potential, when the factorization energy chosen is the second excited state energy. All these energies are non-degenerate. The parameters were taken as $D = 2$, $\kappa = -2$ and $\mu = 1$.

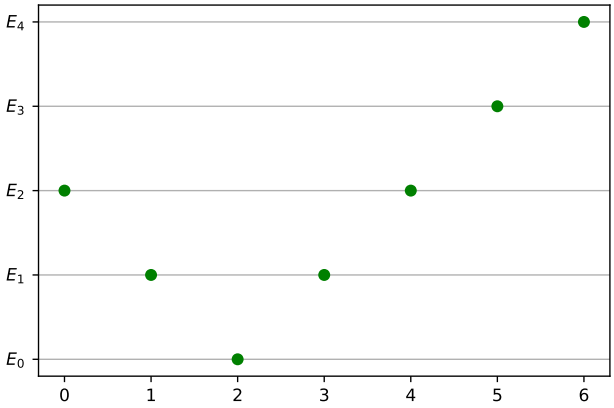

Figure 5.8: Electron energy levels versus the index n labelling the eigenvalues of H_0 for the harmonic oscillator, when the factorization energy chosen is the second excited state energy. The first two excited state energies are twofold degenerate. The parameters were taken as $\omega = \kappa = 1$.

and specific combinations of the parameters and the value of j. In Figure 5.7 we show a plot of the energy levels versus the index n for $j = 2$, where it is possible to see that any energy level is non-degenerate. In order to clarify further this point, it has been shown also a plot of the electron energies versus the quantum number n for the harmonic oscillator potential but taking now $j = 2$, which supplies the standard ordering for the eigenvalues of the initial potential, see Figure 5.8. It can be clearly seen the twofold degeneracy of the first two excited energy levels, and the non-degenerate ground state energy located at $n = j$.

Chapter 6

Monolayer graphene in complex magnetic fields

Since the beginning of this thesis, at the end of subsection 1.4.1, we raised the problem of monolayer graphene in an external in general complex magnetic field $\mathbf{B}(x)$. Although the eigenvalue problem associated to the monolayer graphene electron in this kind of fields can be mathematically addressed, and sometimes solved explicitly, the nature of these magnetic profiles is supposed to be in principle non-physical. However, in recent years some coherent effects of many-body quantum systems due to complex magnetic fields have been detected, in an effective way [Peng et al., 2015]. Motivated by this fact, in this chapter we will solve theoretically and study the consequences of applying a complex magnetic field to monolayer graphene, and the way this assumption modifies the electron energies as well as the probability and current densities, as compared with the real case. Furthermore, we will discuss a possible physical interpretation of this complex magnetic field, by means of an analogy with non-uniformly strained graphene [Oliva-Leyva and Naumis, 2015].

With this in mind, first we need to address the first-order supersymmetric quantum mechanics (SUSY QM) for two intertwined non-Hermitian Schrödinger Hamiltonians, which will helps us to solve the eigenvalue problem for a graphene layer in a complex magnetic field. Thus, we will find the corresponding energy eigenvalues and eigenvectors in order to solve finally some simple examples, for specific complex magnetic profiles.

Section 6.1

SUSY QM for intertwined non-Hermitian Hamiltonians

As we can see in section 2.1, the first-order supersymmetric quantum mechanics is a technique in which two one-dimensional Shcrödinger-like Hermitian Hamiltonians, as well as their eigenfunctions and eigenvalues, are intertwined. In this section we will develop the analogous theory, but now assuming that the two Hamiltonians are non-Hermitian,

$$H^{\pm} = -\frac{d^2}{dx^2} + V^{\pm}(x), \tag{6.1.1}$$

where $V^{\pm}(x) \in \mathbb{C}$. Such operators will satisfy the intertwining relation

$$H^{+}L^{-} = L^{-}H^{-}, \tag{6.1.2}$$

with L^- being a first-order differential intertwining operator of the form

$$L^- = \frac{d}{dx} + \mathrm{w}(x). \tag{6.1.3}$$

Note that in this case $\mathrm{w}(x) \in \mathbb{C}$, thus the Hermitian conjugate of L^-, which is given by

$$\left(L^-\right)^\dagger = -\frac{d}{dx} + \overline{\mathrm{w}}(x), \tag{6.1.4}$$

is not appropriate for describing the complementary intertwining relation between the two Hamiltonians (6.1.1), as we shall see below. Let us substitute now the explicit form of the Hamiltonians (6.1.1) and the intertwining operators (6.1.3) in equation (6.1.2) in order to obtain

$$\begin{aligned} H^+L^- &= -\frac{d^3}{dx^3} - \mathrm{w}\frac{d^2}{dx^2} + \left(V^+ - 2\mathrm{w}'\right)\frac{d}{dx} + V^+\mathrm{w} - \mathrm{w}'', \\ L^-H^- &= -\frac{d^3}{dx^3} - \mathrm{w}\frac{d^2}{dx^2} + V^-\frac{d}{dx} + \mathrm{w}V^- + (V^-)'. \end{aligned} \tag{6.1.5}$$

By comparing the coefficients of the same powers in d/dx we obtain the next two equations

$$\begin{aligned} V^+ &= V^- + 2\mathrm{w}', \\ V^+\mathrm{w} - \mathrm{w}'' &= \mathrm{w}V^- + (V^-)'. \end{aligned} \tag{6.1.6}$$

The first equation gives us a relation between both potentials; if we plug it in the second equation and integrate the result, we arrive at a particular case of the Riccati equation [Ince, 1956],

$$\mathrm{w}^2 - \mathrm{w}' = V^- - \epsilon, \tag{6.1.7}$$

where $\epsilon \in \mathbb{C}$ is a constant called factorization energy. This equation can be transformed in a more familiar one if we make the change $\mathrm{w}(x) = -u'(x)/u(x)$, leading to the Schrödinger equation

$$-u'' + V^-u = \epsilon u. \tag{6.1.8}$$

Thus, $u(x)$ is a formal eigenfunction of the Hamiltonian H^- associated to the factorization energy ϵ, which is called seed solution. From the first row of equation (6.1.6) and (6.1.7) it follows that

$$\begin{aligned} V^- &= \mathrm{w}^2 - \mathrm{w}' + \epsilon, \\ V^+ &= \mathrm{w}^2 + \mathrm{w}' + \epsilon. \end{aligned} \tag{6.1.9}$$

Up to this point, the complex first-order supersymmetric quantum mechanics is similar to the real approach studied in section 2.1. Nevertheless, the products of L^- and its Hermitian conjugate (6.1.4) do not lead to the form of the potentials in equation (6.1.9), thus we cannot give a factorized form of the Hamiltonians $H^\pm$ in terms of those operators. However, if we consider the operator

$$L^+ = -\frac{d}{dx} + \mathrm{w}(x), \tag{6.1.10}$$

its products with the operator L^- turn out to be

$$\begin{aligned} L^+L^- &= -\frac{d^2}{dx^2} + \mathrm{w}^2 - \mathrm{w}', \\ L^-L^+ &= -\frac{d^2}{dx^2} + \mathrm{w}^2 + \mathrm{w}'. \end{aligned} \tag{6.1.11}$$

Hence, the Hamiltonians $H^{\pm}$ can be factorized in the way

$$H^- = L^+L^- + \epsilon, \quad H^+ = L^-L^+ + \epsilon. \tag{6.1.12}$$

From the last two equations it follows the complementary intertwining relation

$$H^-L^+ = L^+H^+. \tag{6.1.13}$$

Let us suppose now that we can solve the Hamiltonian H^-, in other words, the eigenvalues $\mathcal{E}_n^-$ in general complex and its corresponding eigenfunctions $\psi_n^-(x)$ are known. A consequence of the intertwining relation (6.1.2) is that $L^-\psi_n^-(x)$ is an eigenfunction of H^+ associated to the eigenvalue $\mathcal{E}_n^-$. In an analogous way, equation (6.1.13) implies that if $\psi_n^+(x)$ is an eigenfunction of H^+, then $L^+\psi_n^+(x)$ is an eigenfunction of H^-. Therefore, we can write

$$\psi_n^+(x) = \frac{L^-\psi_n^-(x)}{\sqrt{\mathcal{E}_n^- - \epsilon}}, \quad \psi_n^-(x) = \frac{L^+\psi_n^+(x)}{\sqrt{\mathcal{E}_n^- - \epsilon}}. \tag{6.1.14}$$

It is important to notice that the spectrum of the Hamiltonian H^+ could contain the factorization energy ϵ, if the corresponding eigenfunction ψ_ϵ^+ is square-integrable. In fact, equation (6.1.12) implies that such eigenfunction belongs also to the *kernel* of L^+, thus it is given by

$$\psi_\epsilon^+(x) \propto e^{\int \mathrm{w}(x)dx} = \frac{1}{u(x)}. \tag{6.1.15}$$

A paper where it is possible to see how the algorithm introduced here works is [Fernández C. and González, 2015].

Section 6.2

Monolayer graphene in complex magnetic fields

The graphene Hamiltonian H_m describing an electron on the monolayer surface in a magnetic field $\mathbf{B}(x)$ is given in equation (1.2.22). If we assume that the magnetic field is complex, in the Landau gauge the vector potential $\mathbf{A}(x)$ can be written as

$$\mathbf{A}(x) = A(x)e^{i\theta}\,\mathbf{e}_y, \tag{6.2.1}$$

with $A(x)$ being the norm of the vector potential and θ its argument. In agreement with the minimal coupling rule, the Hamiltonian H_m turns out to be

$$H_m = v_0 \begin{pmatrix} 0 & p_x - ip_y - i\frac{e}{c}A(x)e^{i\theta} \\ p_x + ip_y + i\frac{e}{c}A(x)e^{i\theta} & 0 \end{pmatrix}. \tag{6.2.2}$$

As in the real case, this Hamiltonian commutes with the momentum in y-direction. So, it is natural to propose the eigenvectors of the previous Hamiltonian as follows

$$\Psi(x,y) = Ne^{iky} \begin{pmatrix} \psi^+(x) \\ i\psi^-(x) \end{pmatrix}, \tag{6.2.3}$$

with N being a normalization factor, k is the wavenumber in y-direction and $\psi^{\pm}(x)$ are arbitrary functions to be found. Since in the coordinate representation the momentum operator is given by $p_j = -i\hbar\partial_j$, the eigenvalue equation $H_m\Psi(x,y) = E\Psi(x,y)$ leads us to the next system of equations

$$\begin{aligned} L^-\psi^-(x) &= \left[\frac{d}{dx} + k + \frac{e}{c\hbar}A(x)e^{i\theta}\right]\psi^-(x) = \mathcal{E}\psi^+(x), \\ L^+\psi^+(x) &= \left[-\frac{d}{dx} + k + \frac{e}{c\hbar}A(x)e^{i\theta}\right]\psi^+(x) = \mathcal{E}\psi^-(x), \end{aligned} \tag{6.2.4}$$

where $\mathcal{E} = E/\hbar v_0$. It is important to realize that L^+ is not the Hermitian conjugate of L^-. However, a straightforward way to decouple the previous system is to apply the operator L^+ on the first equation (6.2.4) and L^- on the second one, thus we get

$$\begin{aligned} L^+L^-\psi^-(x) &= \left[-\frac{d^2}{dx^2} + \left[k + \frac{e}{c\hbar}A(x)e^{i\theta}\right]^2 - \frac{e}{c\hbar}A'(x)e^{i\theta}\right]\psi^-(x) = \mathcal{E}^2\psi^-(x), \\ L^-L^+\psi^+(x) &= \left[-\frac{d^2}{dx^2} + \left[k + \frac{e}{c\hbar}A(x)e^{i\theta}\right]^2 + \frac{e}{c\hbar}A'(x)e^{i\theta}\right]\psi^+(x) = \mathcal{E}^2\psi^+(x). \end{aligned} \tag{6.2.5}$$

The products L^+L^- and L^-L^+ are second-order differential operators satisfying the eigenvalue equations (6.2.5). If we compare them with equation (6.1.11), we can associate the previous products with the Hamiltonians $H^{\pm}$ of equation (6.1.1), which satisfy the intertwining relation (6.1.2) and thus they can be factorized as in equation (6.1.12). Consequently, we obtain

$$\epsilon = 0, \quad \mathrm{w}(x) = k + \frac{e}{c\hbar}A(x)e^{i\theta}, \tag{6.2.6}$$

$$\begin{aligned} V^- &= \mathrm{w}^2(x) - \mathrm{w}'(x), \\ V^+ &= \mathrm{w}^2(x) + \mathrm{w}'(x). \end{aligned} \tag{6.2.7}$$

Since the factorization energy is zero and we associate it to an eigenfunction of H^-, $\epsilon = 0$ is the corresponding ground state eigenvalue of H_-. The potentials V^+ and V^- are typically shape-invariant, in the sense explained in equation (2.1.23). Note that $\mathrm{w}'(x)$ is directly proportional to the magnetic field amplitude as follows

$$\mathrm{w}'(x) = \frac{e}{c\hbar}B(x). \tag{6.2.8}$$

Therefore, the eigenvectors $\Psi_n(x,y)$ and its associated eigenvalues E_n are given by

$$\begin{aligned} \Psi_0(x,y) &= e^{iky}\begin{pmatrix} 0 \\ i\psi_0^-(x) \end{pmatrix}, \quad E_0 = 0, \\ \Psi_n(x,y) &= \frac{e^{iky}}{\sqrt{2}}\begin{pmatrix} \psi_{n-1}^+(x) \\ i\psi_n^-(x) \end{pmatrix}, \quad E_n = \pm\hbar v_0\sqrt{\mathcal{E}_n^-}, \quad n > 0. \end{aligned} \tag{6.2.9}$$

In the examples of the next section we will explore two useful physical quantities: the probability density, calculated as the product of an eigenvector and its Hermitian conjugate,

$$\rho = \Psi^\dagger\Psi, \tag{6.2.10}$$

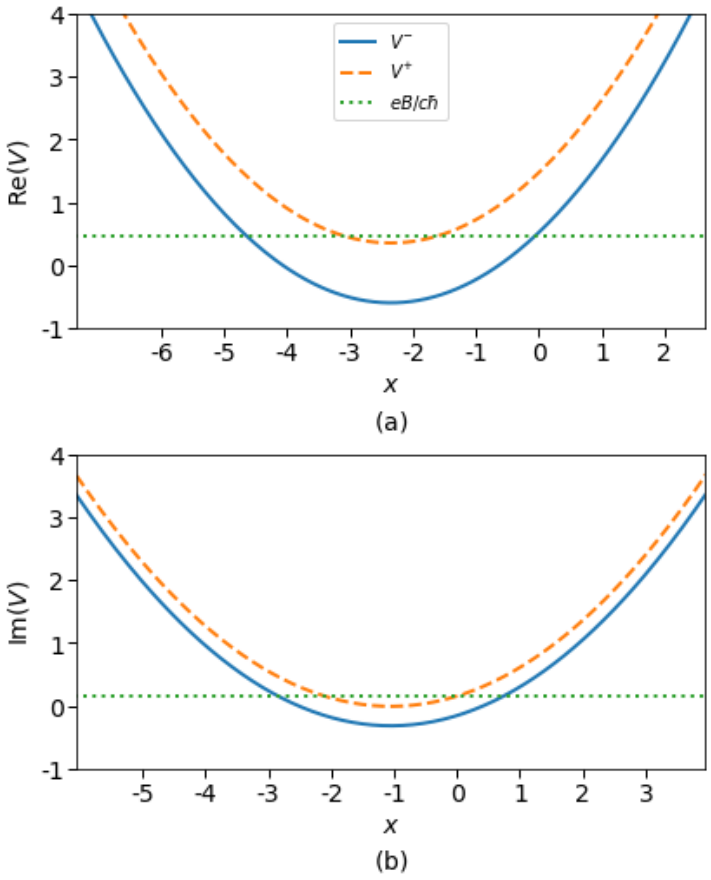

Figure 6.1: Real (a) and imaginary (b) parts of the auxiliary potentials $V^{\pm}$ and the constant magnetic field for $|\omega| = k = 1$ and $\theta = \pi/10$.

and the current density, which for the monolayer graphene Hamiltonian H_m turns out to be

$$\mathbf{J} = v_0 \Psi^\dagger \boldsymbol{\sigma} \Psi. \tag{6.2.11}$$

Although the previous current density expression is similar to that of the real case presented in [Kuru et al., 2009] or to the free case one of [Ferreira et al., 2011], now the continuity equation is inhomogeneous, see appendix B, the inhomogeneous term being given by

$$\frac{2ev_0}{c\hbar}\mathrm{Im}[A(x)e^{i\theta}]\Psi^\dagger \sigma_y \Psi. \tag{6.2.12}$$

Section 6.3

Solvable cases

In this section we will take some magnetic profiles whose amplitude is the product of a complex coefficient times a real function of x. Then, we will determine the corresponding superpotential the auxiliary potentials and the solutions to the problem of an electron in the graphene layer under

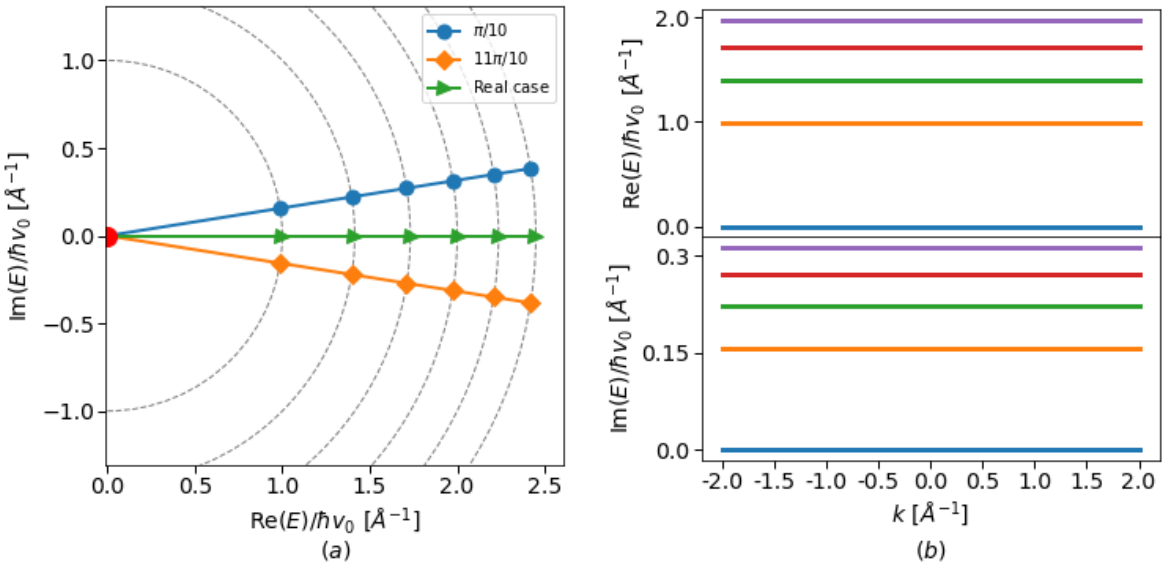

Figure 6.2: (a) Electron energies in the complex plane for the constant magnetic field with three different angles; the common ground state is indicated by a red circle at the origin, and the remaining potential parameters are taken as $|\omega| = k = 1$. (b) Real (top) and imaginary (bottom) parts of the first energies as functions of k for $|\omega| = 1$ and $\theta = \pi/10$.

the given complex magnetic field. It is worth noting that we will start solving first the auxiliary potential V^-, then from its eigenvalues and eigenfunctions the corresponding solutions of V^+ will be found. All the potential real parameters will be supposed to be positive, unless otherwise specified.

Subsection 6.3.1

Constant magnetic field

The first magnetic profile to be studied is constant, namely,

$$\mathbf{B}(x) = Be^{i\theta}\,\mathbf{e}_z, \quad B, \theta \in \mathbb{R}. \tag{6.3.1}$$

In the Landau gauge the vector potential reads

$$\mathbf{A}(x) = xBe^{i\theta}\,\mathbf{e}_y. \tag{6.3.2}$$

Substituting this expression in equation (6.2.6) we get that

$$\mathrm{w}(x) = k + \frac{\omega x}{2}, \tag{6.3.3}$$

with $\omega = (2eB/c\hbar)e^{i\theta}$. The resulting auxiliary potentials are

$$\begin{aligned} V^-(x) &= \frac{\omega^2}{4}\left(x + \frac{2k}{\omega}\right)^2 - \frac{\omega}{2}, \\ V^+(x) &= \frac{\omega^2}{4}\left(x + \frac{2k}{\omega}\right)^2 + \frac{\omega}{2}, \end{aligned} \tag{6.3.4}$$

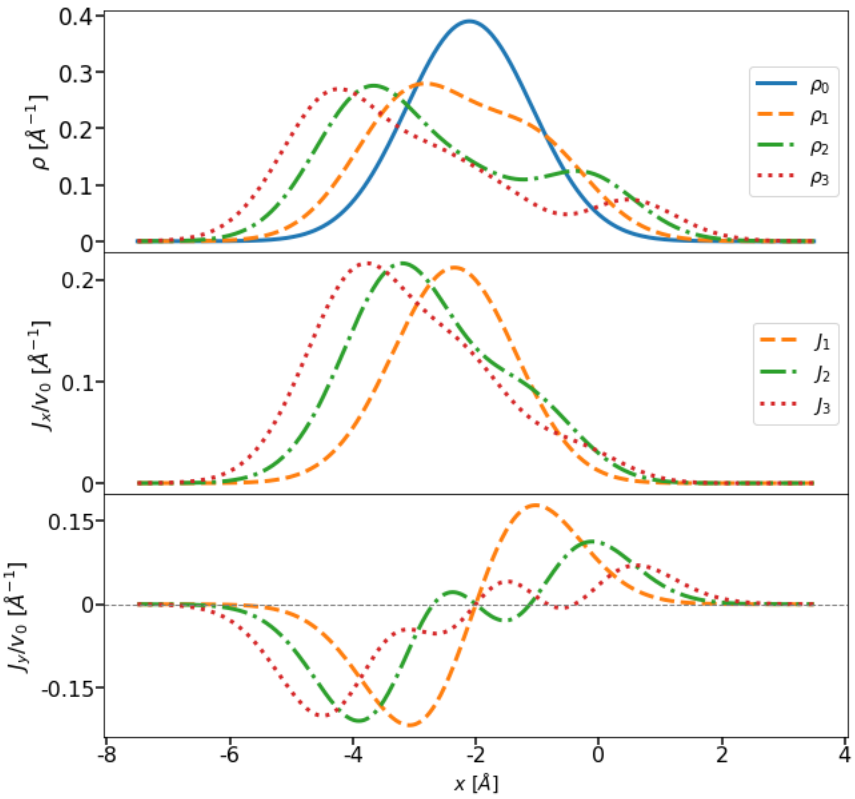

Figure 6.3: Probability densities (top), current densities in x-direction (middle) and in y-direction (bottom) for a constant magnetic field. The potential parameters taken are $|\omega| = k = 1$ and $\theta = \pi/10$.

which are complex shifted harmonic oscillators, as it is seen in Figure 6.1 where their real and imaginary parts are drawn. The associated eigenfunctions are given by

$$\psi_n^{\pm}(x) = \begin{cases} c_n e^{-\frac{\zeta^2}{2}} \mathcal{H}_n(\zeta), & -\frac{\pi}{2} < \theta < \frac{\pi}{2}, \\ c_n e^{-\frac{\xi^2}{2}} \mathcal{H}_n(\xi), & \frac{\pi}{2} < \theta < \frac{3\pi}{2}, \end{cases} \tag{6.3.5}$$

where n is a non-negative integer, $\zeta = \sqrt{\omega/2}(x + 2k/\omega)$, $\xi = \sqrt{-\omega/2}(x - 2k/\omega)$ and $\mathcal{H}_n(\zeta)$ is a Hermite polynomial of degree n with complex argument [Fernández C. and González, 2015]; the expression $\sqrt{\omega}$ represents to $\sqrt{|\omega|}e^{i\theta/2}$ and $\sqrt{-\omega}$ to $\sqrt{|\omega|}e^{i(\pi-\theta)/2}$. The corresponding eigenvalues of the potentials (6.3.4) turn out to be

$$\mathcal{E}_0^- = 0, \quad \mathcal{E}_n^- = \mathcal{E}_{n-1}^+ = \pm n\omega, \tag{6.3.6}$$

with n being a natural number, the upper sign is taken for $-\pi/2 < \theta < \pi/2$ while the lower one for $\pi/2 < \theta < 3\pi/2$. Thus, the electron (hole) energies (6.2.9) for monolayer graphene in a complex constant magnetic field can be written as follows

$$E_n = \pm\hbar v_0 \sqrt{\pm n\omega}, \tag{6.3.7}$$

whose norms are exactly the same as the electron (hole) energies for the real case addressed in [Kuru et al., 2009], but now they are rotated in the complex plane an angle $\theta/2$ with respect to

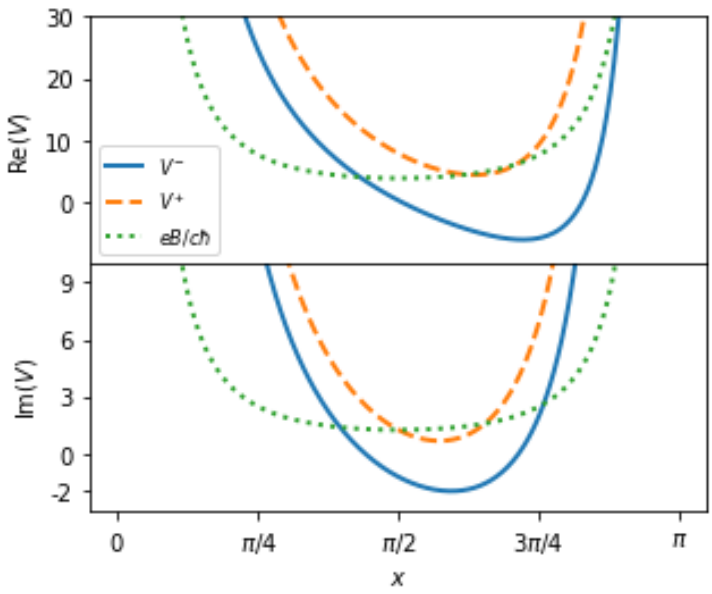

Figure 6.4: Real (top) and imaginary (bottom) parts of the auxiliary potentials $V^{\pm}$ and the magnetic field for the trigonometric singular well with $|D| = 4$, $\theta = \pi/10$, $k = -2$ and $\mu = 1$.

the real axis, see Figure 6.2(a). In that plot it can be seen also several concentric circumferences centered at the origin, of radius $R \propto \sqrt{n|\omega|}$, on which the energy E_n lies regardless of the angle θ. Thus, notwithstanding its complex nature we can say that for a fixed angle θ the spectrum of H_m is ordered in the standard way. Moreover, $\mathrm{Sp}(H_m)$ is infinite discrete, and its energies do not depend on k. In Figure 6.2(b) it is shown the real and imaginary parts of the first electron energies as functions of k. The square-integrability of $\Psi_n(x, y)$ does not impose constrains to the norm of ω, but only to its argument θ, as it is seen in equation (6.3.5). Furthermore, when $\theta = \pm\pi/2$ the eigenfunctions $\psi_n^{\pm}(x)$ are not square-integrable, since the auxiliary potentials become repulsive oscillators for which the Hamiltonian H_m does not have bound states [Bermudez and Fernández C., 2013]. The probability and current densities are drawn in Figure 6.3 for the first four eigenstates. Note that the ground state has a null current density, since as it is seen in equation (6.2.9) its upper entry is zero.

Subsection 6.3.2

Trigonometric singular well

Now it is taken a trigonometric complex magnetic field in the form

$$\mathbf{B}(x) = Be^{i\theta}\csc^2(\mu x)\,\mathbf{e}_z, \quad B, \theta, \mu \in \mathbb{R}. \tag{6.3.8}$$

The associated vector potential becomes

$$\mathbf{A}(x) = -\frac{Be^{i\theta}}{\mu}\cot(\mu x)\,\mathbf{e}_y. \tag{6.3.9}$$

From equation (6.2.6) the following superpotential $\mathrm{w}(x)$ is obtained,

$$\mathrm{w}(x) = k - D\cot(\mu x), \tag{6.3.10}$$

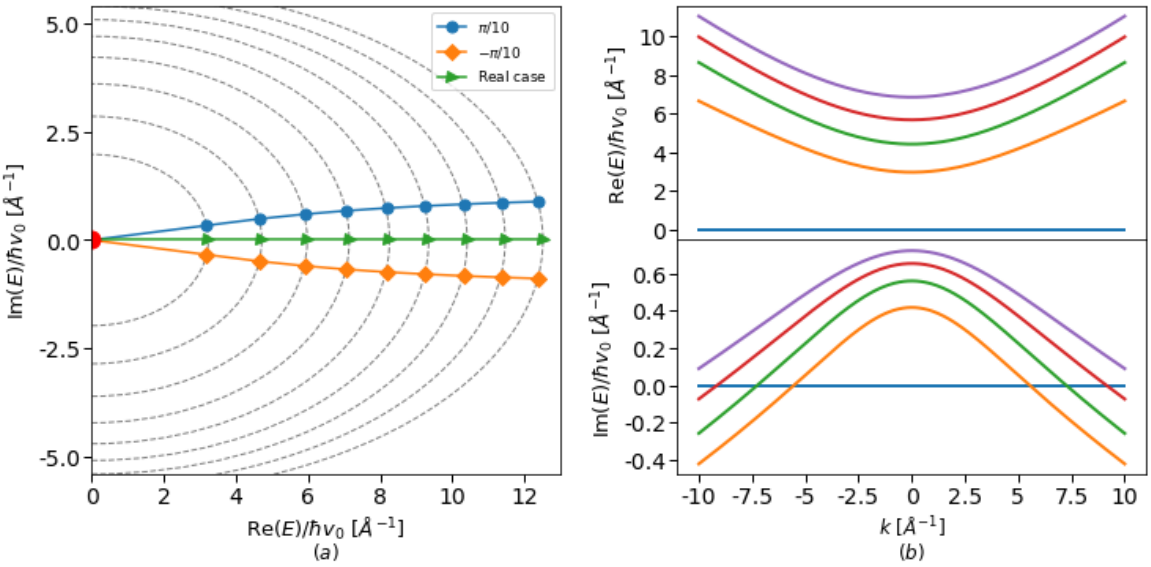

Figure 6.5: (a) Electron energies in the complex plane for the trigonometric singular well with three different angles; the common ground state is indicated by a red circle at the origin, and the remaining potential parameters are taken as $|D| = 4$, $k = -2$ and $\mu = 1$. (b) Real (top) and imaginary (bottom) parts of the first energies as functions of k for $|D| = 4$, $\theta = \pi/10$ and $\mu = 1$.

with $D = (eB/c\hbar\mu)e^{i\theta}$. Thus, the auxiliary potentials become

$$\begin{aligned} V^-(x) &= D(D-\mu)\csc^2(\mu x) - 2Dk\cot(\mu x) + k^2 - D^2, \\ V^+(x) &= D(D+\mu)\csc^2(\mu x) - 2Dk\cot(\mu x) + k^2 - D^2, \end{aligned} \tag{6.3.11}$$

whose form suggests to call them complex trigonometric Rosen-Morse potentials. In Figure 6.4 their real and imaginary parts are plotted. The corresponding eigenfunctions are given in terms of Jacobi polynomials $\mathcal{P}_n^{(\alpha,\beta)}$ with complex argument and indexes, namely,

$$\psi_n^{\pm}(x) = c_n(-1)^{-(s_\pm+n)/2}(1+\zeta^2)^{-(s_\pm+n)/2}e^{r_\pm \operatorname{arccot}(\zeta)}\mathcal{P}_n^{(-s_\pm-n-ir_\pm,-s_\pm-n+ir_\pm)}(i\zeta), \tag{6.3.12}$$

where $s_- = D/\mu$, $s_+ = s_- + 1$, $r_- = -kD/\mu(D+n\mu)$, $r_+ = -kD/\mu(D+\mu+n\mu)$, $\zeta = \cot(\mu x)$ and n is a non-negative integer. The square-integrability requirement of these eigenfunctions limits us to the right side of the complex plane, i.e., $-\pi/2 < \theta < \pi/2$. The spectra of the Hamiltonians $H^\pm$ are composed by the eigenvalues

$$\mathcal{E}_0^- = 0, \quad \mathcal{E}_n^- = \mathcal{E}_{n-1}^+ = k^2 - D^2 + (D+n\mu)^2 - \frac{k^2D^2}{(D+n\mu)^2}, \tag{6.3.13}$$

with $n \in \mathbb{N}$. Substituting them in equation (6.2.9) the electron (hole) energies turn out to be

$$E_n = \pm\hbar v_0\sqrt{k^2 - D^2 + (D+n\mu)^2 - \frac{k^2D^2}{(D+n\mu)^2}}. \tag{6.3.14}$$

We must notice that now the norm of E_n is not equal to the real energy derived in [Kuru et al., 2009], except by the case when $\theta = 0$. Meanwhile, its argument Φ_n has a non-trivial dependence

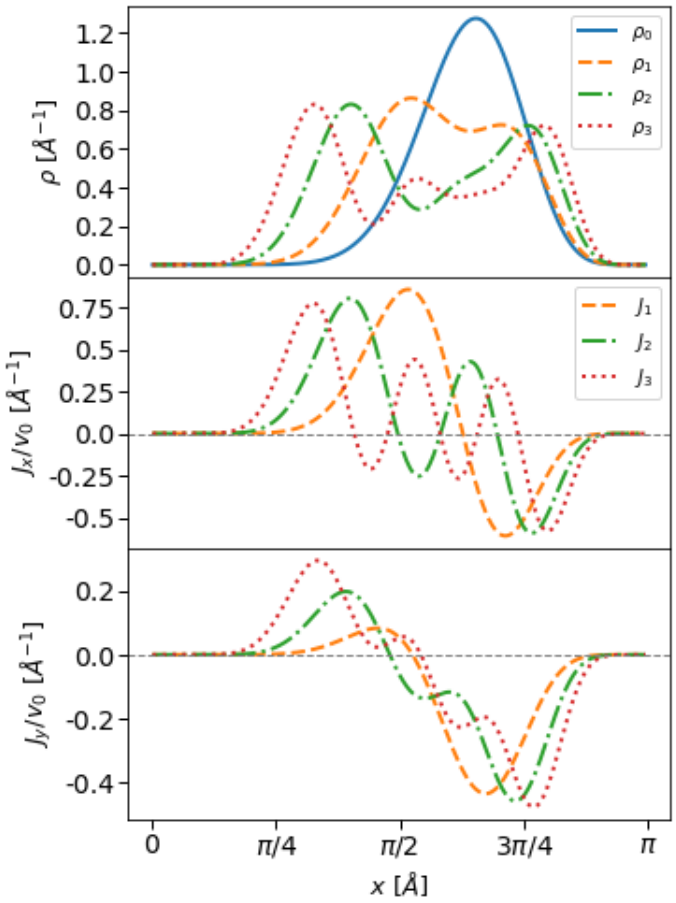

Figure 6.6: Probability densities (top), current densities in x-direction (middle) and in y-direction (bottom) for a trigonometric singular well. The potential parameters are taken as $|D| = 4$, $\theta = \pi/10$, $k = -2$ and $\mu = 1$.

on θ and the potential parameters. The first electron energies in the complex plane are shown in Figure 6.5(a). It can be observed also concentric ellipses centered at the origin, with the energy E_n belonging to the ellipse whose semi-major axis is equal to the n-th energy in the real case. Thus, analogously to the previous case this fact implies that for a fixed angle θ $\mathrm{Sp}(H_m)$ is ordered in the standard way. However, this happens just in the interval $(-k_0, k_0)$, where $\mathrm{Im}\,(E_1(k_0)) = 0$. Despite this, the spectrum of H_m is infinite discrete as can be observed in Figure 6.5(b). In addition, plots of the probability and current densities are displayed in Figure 6.6 for the first four eigenstates.

Subsection 6.3.3

Exponentially decaying field

As our last example, let us analyse the exponentially decaying complex magnetic field

$$\mathbf{B}(x) = Be^{i\theta}e^{-\mu x}\,\mathbf{e}_z, \quad B \in \mathbb{R}, \tag{6.3.15}$$

whose vector potential is

$$\mathbf{A}(x) = -\frac{B}{\mu}e^{i\theta}e^{-\mu x}\,\mathbf{e}_y. \tag{6.3.16}$$

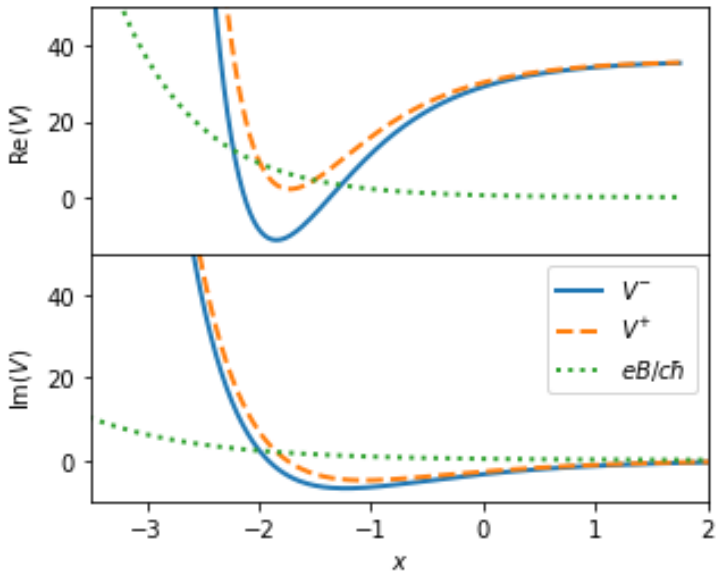

Figure 6.7: Real (top) and imaginary (bottom) parts of the auxiliary potentials $V^{\pm}$ and the exponentially decaying magnetic field for $|D| = 1$, $\theta = \pi/10$, $k = 6$ and $\mu = 1$.

In agreement with equation (6.2.6) the superpotential is written as

$$\mathrm{w}(x) = k - De^{-\mu x}, \tag{6.3.17}$$

with $D = (eB/c\hbar\mu)e^{i\theta}$. By substituting $\mathrm{w}(x)$ in equation (6.2.7) we get the auxiliary potentials

$$\begin{aligned} V^{-}(x) &= k^2 + D^2e^{-2\mu x} - 2D\left(k + \frac{\mu}{2}\right)e^{-\mu x}, \\ V^{+}(x) &= k^2 + D^2e^{-2\mu x} - 2D\left(k - \frac{\mu}{2}\right)e^{-\mu x}, \end{aligned} \tag{6.3.18}$$

which have the same form as the Morse potentials but with the parameter D being now complex. The real and imaginary parts of $V^{\pm}(x)$ are shown in Figure 6.7. They are exactly solvable potentials with its eigenfunctions being given by

$$\psi_n^{\pm}(x) = c_n(\zeta)^{s_{\pm}-n}e^{-\frac{\zeta}{2}}\mathcal{L}_n^{2(s_{\pm}-n)}(\zeta), \tag{6.3.19}$$

where $s_{-} = k/\mu$, $s_{+} = s_{-} - 1$, $\zeta = (2D/\mu)e^{\mu x}$, n is a non-negative integer and $\mathcal{L}_n^{\lambda}(\zeta)$ is an associated Laguerre polynomial of complex argument. The square-integrability conditions imply that $-\pi/2 < \theta < \pi/2$ and $k > n\mu$. The corresponding eigenvalues are

$$\mathcal{E}_0^{-} = 0, \quad \mathcal{E}_n^{-} = \mathcal{E}_{n-1}^{+} = k^2 - (k - n\mu)^2, \tag{6.3.20}$$

with n being a natural number. It is worth noticing that the spectra of the Hamiltonians $H^{\pm}$ are real since, unlike the two previous examples, now they are pseudo-Hermitian operators [Mostafazadeh, 2002a,b]. Thereby, the energy eigenvalues for the electrons (holes) in monolayer graphene take the form

$$E_n = \pm\hbar v_0\sqrt{k^2 - (k - n\mu)^2}. \tag{6.3.21}$$

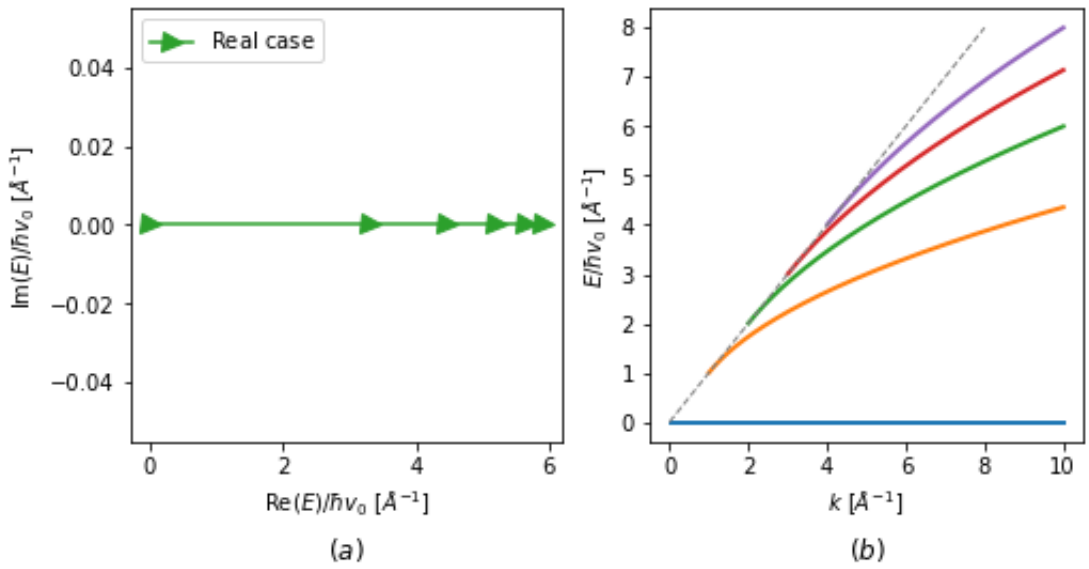

Figure 6.8: (a) Electron energies in the complex plane for the exponentially decaying magnetic field with $|D| = 1$, $k = 6$ and $\mu = 1$. (b) Electron energies as functions of k for $|D| = 1$ and $\mu = 1$.

In this instance the spectrum of H_m coincides exactly with the one for the real case addressed in [Kuru et al., 2009]. Such spectrum is discrete but finite, since once the parameters k and μ are fixed the condition $k > n\mu$ limits the number of square-integrable eigenfunctions and hence the number of allowed electron energies, see Figure 6.8(a). In Figure 6.8(b) the energy levels E_n as functions of k are shown, and an enveloping line is also shown whose slope v_0 equals the average y-velocity. This line separates the k-domain into two regions, one where there are bound states and an other one where the scattering states arise. Finally, the probability and current densities are plotted in Figure 6.9.

Section 6.4

Discussion

It is interesting to observe that there are some x-points for which the imaginary parts of $eB(x)/c\hbar$ and $V^+(x)$ are equal, as it is shown in figures 6.1, 6.4 and 6.7. If we denote as χ one of these points, in order to fulfill equation (6.1.9) it turns out that $\mathrm{Im}[\mathrm{w}^2(\chi)] = 0$, which implies that $\mathrm{Re}[\mathrm{w}(\chi)] = 0$. Let us recall now a classical '*kinematical' quantity*, the momentum along y-direction given by $\Pi_y = p_y + (e/c)A$. Since the canonical momentum p_y is a constant of motion, it follows that $\mathrm{Re}[\Pi_y(\chi)] = \hbar\mathrm{Re}[\mathrm{w}(\chi)] = 0$. It is worth noticing that the maximum of the ground state probability density appears at one point χ, and the latter depends on the angle θ (see Figures 6.3, 6.6 and 6.9).

On the other hand, since the Hamiltonian (6.2.2) is non-hermitian, its eigenvalues are not necessarily real. In fact, it can be written as

$$H_m = v_0 \left[\sigma_x p_x + \sigma_y (p_y + (e/c)A(x)e^{i\theta})\right], \tag{6.4.1}$$

or equivalently as

$$H = H_R + iv_0(e/c)\sigma_y A(x)\sin\theta, \tag{6.4.2}$$

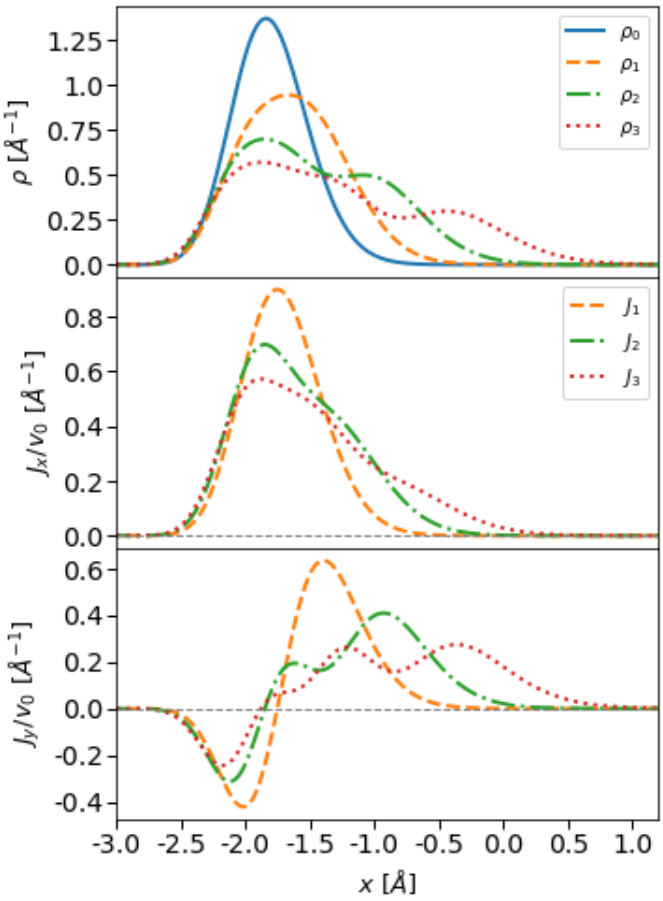

Figure 6.9: Probability densities (top), current densities in x-direction (middle) and in y-direction (bottom) for an exponentially decaying magnetic field. The potential parameters taken are $|D| = 1$, $\theta = \pi/10$, $k = 6$ and $\mu = 1$.

where $H_R = v_0 \left[\sigma_x p_x + \sigma_y \left(p_y + (e/c)|A(x)| \cos\theta\right)\right]$ is a hermitian operator whose eigenvalues are real, which is similar to the Hamiltonian addressed in Kuru et al. [2009]. The second term in equation (6.4.2) is an anti-hermitian operator whose eigenvalues are purely imaginary. In order to understand the nature of this term, let us remember that the Dirac-Weyl equation in graphene describes a massless *pseudo-spin* $1/2$ particle, where *pseudo-spin 'up'* means that the electron is in the sublattice B and *'down'* in the sublattice A. By remembering the pseudo-spin ladder operators $S_\pm = S_x \pm iS_y$, it follows that the second term can be written as $(ev_0/c\hbar)\,(S_+ - S_-)\,A(x)\sin\theta$. It induces pseudo-spin rotations, and it is analogous to the corresponding term that appears in the Hamiltonian describing non-uniformly strained graphene (see Oliva-Leyva and Naumis [2015]). By sticking to this analogy, in de Juan et al. [2013] this anti-hermitian operator is associated to the layer curvature induced by strain, while in the case analyzed here the analogous term is proportional to the imaginary part of the vector potential, but the point is to find a phenomenon that could be associated with it. Then, since the Hamiltonian (6.4.2) is time-independent, the time evolution of the total probability associated to an eigenstate has an exponential factor which depends on the imaginary part of its eigenvalue E_n, namely,

$$\mathcal{P}_T(t) = \langle \Psi_n(t)|\Psi_n(t)\rangle = e^{2\frac{\mathrm{Im}[E_n]}{\hbar}t}\langle \Psi_n(0)|\Psi_n(0)\rangle. \tag{6.4.3}$$

A small probability increase (decrease) occurs if the exponent fulfils $2(\mathrm{Im}[E_n]/\hbar)t \ll 1$. This happens for approximate times which are inversely proportional to the imaginary part of the energy eigenvalue. Using the polar form $E_n = |E_n|e^{i\phi_n}$, for the first bound states it turns out that if $\phi_n \ll 1$ we obtain times which are long enough to guarantee the probability conservation, except by small perturbations. Thus, the anti-hermitian term in the Hamiltonian (6.4.2) can be seen as a perturbation describing the loss or gain of charger carriers in the graphene sublattices. Therefore, one could revisit the graphene in a real magnetic field orthogonal to its surface, trying to model it as a non-conservative system, due to the interaction of the *pseudo-spin* electron with the magnetic field, through the exactly solvable non-hermitian Hamiltonian (6.2.2), and taking the expansion of the eigenvalues E_n in powers of ϕ_n one could find the corresponding energy corrections (if required). Furthermore, the probability and current densities will be modified, as compared with the real case. It is worth noticing that, despite the Hamiltonian is non-hermitian, we cannot ensure that its eigenvalues will be complex, as it was seen in the third example of the previous section where the eigenvalues were real and the total probability for their corresponding eigenstates was conserved.

Finally, we must mention an interesting case where the anti-hermitian term in the Hamiltonian (6.4.2) cannot be considered as a perturbation around $\theta = 0$: in the limit $\theta \to \pi/2$ our Hamiltonian describes the free graphene Ferreira et al. [2011] plus an interaction term between the *pseudo-spin* electron and a purely imaginary magnetic field. All the magnetic profiles discussed in section 6.3 will lead us to auxiliary potentials without bound states in this limit. However, for arguments $\theta \approx \pi/2$ we will get auxiliary potentials with "weak" bound states, whose probability densities have a pronounced maximum that diverges in the limit when θ tends to $\pi/2$.

Conclusions

Throughout this work we have solved exactly, inside the tight-binding framework, the effective Hamiltonians describing an electron in monolayer and bilayer graphene under magnetic fields orthogonal to the graphene surface, finding explicit expressions for the bound states by means of supersymmetric quantum mechanics. We have analysed different magnetic profiles in the Landau gauge leading us to translationally invariant problems along y-direction. Thus, through the minimal coupling rule the eigenvalues and eigenvectors of the graphene Hamiltonians H_m and H_b in equations (6.2.2) and (3.4) will depend in general on the wavenumber k in y-direction. Although supersymmetric quantum mechanics allows us to transform the eigenvalue problem of H_m and H_b into two intertwined one-dimensional stationary Schrödinger-like equations, the corresponding auxiliary potentials turn out to be expressed in terms of parameters that are not necessarily linear in k. Moreover, the calculation of this k-dependence in general could be complicated, as it is shown in appendix A. It is worth mentioning that the modification in the momentum induced by the minimal coupling rule causes the inclusion of extra terms in the associated continuity equation with respect to the free case displayed in [Ferreira et al., 2011]. For bilayer graphene this extra term can be expressed as the divergence of a vector function which is included automatically in the current density. On the other hand, for monolayer graphene if the magnetic field is real there is no modification at all, but if it is complex although the current density is not changed with respect to the free case the continuity equation becomes inhomogeneous, see appendix B.

Most of this thesis is focused on bilayer graphene and the use of second-order supersymmetric quantum mechanics to find the solutions of the corresponding eigenvalue problem. To apply this algorithm without restrictions two assumptions were made (see chapter 3) so that we could address three important cases: the case where the auxiliary potentials are shape-invariant in the sense of equation (2.1.23), which is analogous to the monolayer case worked in [Kuru et al., 2009]; the more general case where two consecutive energy levels are chosen as factorization energies (see chapter 4); the confluent case of chapter 5. It is important to note that in contrast to the monolayer case, for bilayer graphene there exists degeneracy in some of the bound state energies. Nevertheless, this degeneracy depends on the election of factorization energies and potential parameters, so it is possible that for a particular choice none of the bound state energies are degenerate. Furthermore, since by construction the wavenumber k is fixed from the very beginning, thus in the non-shape-invariant cases the generated magnetic field will depend on k, consequently if this parameter changes the magnetic field is consistently modified, see sections 4.3 and 5.3.

On the other hand, when we consider a complex magnetic field (chapter 6) the Hamiltonian H_m in equation (6.2.2) is expressed as the sum of a Hermitian term plus an anti-Hermitian one, see equation (6.4.1), the last causing *pseudo-spin* rotations. Despite the complex nature of the

problem, a possible physical interpretation as an effective complex magnetic field (that arises by analogy with the non-uniformly strained graphene) could be that a real magnetic field with the same magnitude as the complex one is applied to graphene, and the angle θ allows us to introduce in the model a term describing the loss or gain of charge carriers, induced by the interaction between the *pseudo-spin* electron and the magnetic field. There are important differences in the behaviour of some physical quantities in the complex case with respect to the real case, as the probability and current densities. In particular, the current density along x-direction becomes non-null, in contrast to the result found in Kuru et al. [2009] for the real case. Furthermore, now the ground state probability density acquires its maximum at the point where the imaginary parts of $eB/\hbar c$ and V^+ turn out to be equal.

Finally, this work has an interesting future outlook:

- The second-order supersymmetric quantum mechanics allow us to choose the factorization energies in many ways that are different from the cases worked here: both can be taken below the ground state energy, between two adjacent energy levels or to be complex in general, see [Fernandez and Fernandez-Garcia, 2005]. For sure they will generate exotic auxiliary potentials (solvable) and associated magnetic profiles.

- A complex magnetic field could be introduced in the bilayer graphene effective Hamiltonian H_b (3.4); this work requires more exploration and analysis.

- The use of supersymmetric quantum mechanics to solve the graphene effective Hamiltonians is not limited to this material. Other 2-D materials described as well by Dirac-like Hamiltonians could be addressed with this technique, and exact analytic solutions could be found.

Appendix A

Relation among the potential parameters and the wavenumber k

The different initial potentials that we have dealt with in this work depend on several parameters; which in this appendix will be denoted as λ. Let us recall that we can determine the supersymmetric partner potentials V_0 and V_2 if we know the key function $\eta(x;\lambda)$, which is related with the magnetic field as follows

$$B(x;\lambda) = \frac{c\hbar}{2e}\eta'(x;\lambda). \tag{A.1}$$

Since in the Landau gauge the associated vector potential is obtained as the integral of the magnetic field,

$$A(x;\lambda) = \int B(x;\lambda)dx, \tag{A.2}$$

when substituting equation (A.1) in the previous expression we get that

$$A(x;\lambda) = \frac{c\hbar}{2e}\left[\eta(x;\lambda) + C(\lambda)\right], \tag{A.3}$$

where $C(\lambda)$ is an integration constant, independent of x. NOte that the vector potential $A(x;\lambda)$, the function $\eta(x;\lambda)$ and the wavenumber k are related through (see equation (3.2)),

$$k = \frac{1}{2}\left(\eta(x;\lambda) - \frac{2e}{c\hbar}A(x;\lambda)\right), \tag{A.4}$$

we can conclude that

$$k \propto C(\lambda). \tag{A.5}$$

This means that we just need to identify the constant $C(\lambda)$ and to obtain then the relation among the potential parameters λ and the wavenumber k. However, in general this is not an easy task because the integral in equation (A.2) cannot be calculated in a simple way.

Appendix B

Continuity equation

Since the effective Hamiltonians for monolayer and bilayer graphene are modified via the minimal coupling rule, thus the corresponding current densities could not have the same form that in the free case discussed in [Ferreira et al., 2011]. Nevertheless, the right expressions can be determined in the standard way, as it is carried out next.

Section B.1

Monolayer graphene

When a complex magnetic field is cosidered (see chapter 6), the minimal coupling rule applied to the monolayer effective Hamiltonian leads to

$$H_m = \hbar v_0 \begin{pmatrix} 0 & -i\partial_x - \partial_y - i\frac{e}{c\hbar}A(x)e^{i\theta} \\ -i\partial_x + \partial_y + i\frac{e}{c\hbar}A(x)e^{i\theta} & 0 \end{pmatrix}, \tag{B.1.1}$$

where $p_j = -i\hbar\partial_j$ and the Landau gauge was taken. Assuming normalized wavevectors $\Psi(x,y) = (\psi^+(x,y), \psi^-(x,y))^T$, with $\psi^{\pm}(x,y)$ being arbitrary wavefunctions, it turns out that

$$H_m\Psi = \hbar v_0 \begin{pmatrix} -i\partial_x\psi^- - \partial_y\psi^- - i\frac{e}{c\hbar}A(x)e^{i\theta}\psi^- \\ -i\partial_x\psi^+ + \partial_y\psi^+ + i\frac{e}{c\hbar}A(x)e^{i\theta}\psi^+ \end{pmatrix}. \tag{B.1.2}$$

On the other hand, the dynamics of the system is ruled by

$$i\hbar\frac{\partial\Psi}{\partial t} = H_m\Psi, \tag{B.1.3}$$

then, the continuity equation is given by

$$\frac{\partial\rho}{\partial t} + \frac{i}{\hbar}\left[\Psi^\dagger\left(H_m\Psi\right) - \left(H_m\Psi\right)^\dagger\Psi\right] = 0. \tag{B.1.4}$$

If we work in more detail the second term of the previous equation, we get that the continuity equation turns out to be

$$\frac{\partial\rho}{\partial t} + v_0\nabla\cdot\left(\Psi^\dagger\boldsymbol{\sigma}\Psi\right) = 2v_0\mathrm{Im}\left(\frac{e}{c\hbar}A(x)e^{i\theta}\right)\Psi^\dagger\sigma_y\Psi, \tag{B.1.5}$$

where $\boldsymbol{\sigma}$ is the vector whose components are the Pauli matrices. We can see that this continuity equation is inhomogeneous, which is due to the Hamiltonian in equation (B.1.1) is non Hermitian. Therefore, the current density takes the form

$$\mathbf{J} = v_0\Psi^\dagger\boldsymbol{\sigma}\Psi. \tag{B.1.6}$$

It is worth noticing that here we have used the Landau gauge, but if an arbitrary gauge is taken (just keeping the magnetic field along z-direction), the operators off the diagonal of H_m will change to $-i\partial_x + (e/c\hbar)A_x - \partial_y - i(e/c\hbar)A_y$ and $-i\partial_x + (e/c\hbar)A_x + \partial_y + i(e/c\hbar)A_y$, with $A_x, A_y \in \mathbb{C}$. Despite the current density remains invariant, the right hand side of equation (B.1.5) will acquire a new term given by $2v_0 \mathrm{Im}\left[(e/c\hbar)A_x\right] \Psi^\dagger \sigma_x \Psi$.

Section B.2

Bilayer graphene

In chapter 3 we made three assumptions allowing us to apply directly the second-order supersymmetric quantum mechanics to bilayer graphene, thus we can write the bilayer Hamiltonian in the following form

$$H_b = -\frac{1}{2m}\begin{pmatrix} 0 & \Pi^2 - \hbar^2 f \\ \left(\Pi^\dagger\right)^2 - \hbar^2 f & 0 \end{pmatrix}, \tag{B.2.1}$$

where $\Pi = p_x - ip_y - i(e/c)A$ and the Landau gauge was taken. Here we will consider that A and f are two real functions depending on both coordinates x, y. Since $p_j = -i\hbar\partial_j$, assuming normalized wavevectors $\Psi(x,y) = (\psi_2(x,y), \psi_0(x,y))$, with $\psi_2(x,y)$, $\psi_0(x,y)$ being arbitrary wavefunctions, we get that

$$\begin{aligned} H\Psi = -\frac{\hbar^2}{2m}\Big(&\partial_x\left(-\partial_x + i\partial_y\right)\psi_0 + \partial_y\left(\partial_y + i\partial_x\right)\psi_0 - 2\frac{eA}{c\hbar}\partial_x\psi_0 + i2\frac{eA}{c\hbar}\partial_y\psi_0 \\ &- \psi_0\partial_x\frac{eA}{c\hbar} + i\psi_0\partial_y\frac{eA}{c\hbar} - \frac{e^2A^2}{c^2\hbar^2}\psi_0 - f\psi_0,\ \partial_x\left(-\partial_x - i\partial_y\right)\psi_2 + \partial_y\left(\partial_y - i\partial_x\right)\psi_2 \\ &+ 2\frac{eA}{c\hbar}\partial_x\psi_2 + i2\frac{eA}{c\hbar}\partial_y\psi_2 + \psi_2\partial_x\frac{eA}{c\hbar} + i\psi_2\partial_y\frac{eA}{c\hbar} - \frac{e^2A^2}{c^2\hbar^2}\psi_2 - f\psi_2\Big)^T. \end{aligned} \tag{B.2.2}$$

The dynamics is once again ruled by equation (B.1.3) but changing H_m by H_b, and the same happens with equation (B.1.4). Thus, the second term of the latter equation in this case turns out to be

$$-\nabla\cdot\frac{\hbar}{m}\left\{\left[\mathrm{Im}\left(\Psi^\dagger j_x\Psi\right) + \frac{eA}{c\hbar}\Psi^\dagger\sigma_y\Psi\right]\mathbf{e}_x + \left[\mathrm{Im}\left(\Psi^\dagger j_y\Psi\right) - \frac{eA}{c\hbar}\Psi^\dagger\sigma_x\Psi\right]\mathbf{e}_y\right\}. \tag{B.2.3}$$

Thus, the current density can be written as

$$\mathbf{J} = -\frac{\hbar}{m}\left[\mathrm{Im}\left(\Psi^\dagger\mathbf{j}\Psi\right) + \frac{eA}{c\hbar}\Psi^\dagger\boldsymbol{\varsigma}\,\Psi\right], \tag{B.2.4}$$

where $j_x = \sigma_x\partial_x + \sigma_y\partial_y$, $j_y = \sigma_y\partial_x - \sigma_x\partial_y$, $\varsigma_l = \varepsilon_{lm}\sigma_m$, $l, m = x, y$, ε_{lm} is the 2-dim Levi-Civita symbol and σ_m are the Pauli matrices.

It is worth noting that, since the Hamiltonian (B.2.1) is quadratic in the momentum, the current density of the last equation is similar to one presented in [Sakurai, 1994]. Furthermore, for an arbitrary gauge the operator Π will change to $p_x + (e/c)A_x - ip_y - i(e/c)A_y$, hence the current density will acquire an extra term given by $(eA_x/c\hbar)\Psi^\dagger\boldsymbol{\sigma}\Psi$.

Bibliography

Andrianov, A., Borisov, N., and Ioffe, M. (1984). The factorization method and quantum systems with equivalent energy spectra. *Phys. Lett. A*, 105(1):19–22.

Andrianov, A., Ioffe, M., Cannata, F., and Dedonder, J. (1995). Second order derivative supersymmetry, q deformations and the scattering problem. *Int. J. Mod. Phys. A*, 10:2683.

Andrianov, A., Ioffe, M., and Spiridonov, V. (1993). Higher-derivative supersymmetry and the Witten index. *Phys. Lett. A*, 174:273.

Aref'eva, I., Fernández, D. J., Hussin, V., Negro, J., Nieto, L. M., and Samsonov, B. F. (2004). Progress in supersymmetric quantum mechanics. *J. Phys. A: Math. Gen.*, 37(43).

Ashcroft, N. and Mermin, N. (1976). *Solid State Physics*. Harcourt College Publishers, USA, college edition.

Bagchi, B. K. (2001). *Supersymmetry in Quantum and Classical Mechanics*. Chapman & Hall/CRC, Boca Raton.

Bermudez, D. (2016). Wronskian differential formula for k-confluent susy qm. *Ann. Phys.*, 364:35–52.

Bermudez, D., Fernández C, D. J., and Fernández-García, N. (2012). Wronskian differential formula for confluent supersymmetric quantum mechanics. *Phys. Lett. A*, 376(5):692–696.

Bermudez, D. and Fernández C., D. J. (2013). Factorization method and new potentials from the inverted oscillator. *Ann. Phys.*, 333:290–306.

Cariñena, J. and Ramos, A. (2000). Riccati equation, factorization method and shape invariance. *Rev. Math. Phys.*, 12:1279.

Castillo-Celeita, M., Díaz-Bautista, E., and Oliva-Leyva, M. (2020). Coherent states for graphene under the interaction of crossed electric and magnetic fields. *Ann. Phys.*, 421:168287.

Castillo-Celeita, M. and Fernández, D. J. (2020). Dirac electron in graphene with magnetic fields arising from first-order intertwining operators. *J. Phys. A: Math. Theor.*, 53:035302.

Compean, C. B. and Kirchbach, M. (2005). The trigonometric Rosen–Morse potential in the supersymmetric quantum mechanics and its exact solutions. *J. Phys. A: Math. Gen.*, 39:547.

Concha, Y., Huet, A., Raya, A., and Valenzuela, D. (2018). Supersymmetric quantum electronic states in graphene under uniaxial strain. *Mat. Res. Express*, 5:065607.

Contreras-Astorga, A. and Fernández C., D. J. (2008). Supersymmetric partners of the trigonometric Pöschl–Teller potentials. *J. Phys. A: Math. Theor.*, 41(47):475303.

Contreras-Astorga, A. and Schulze-Halberg, A. (2015a). The generalized zero-mode supersymmetry scheme and the confluent algorithm. *Ann. Phys.*, 354:353–364.

Contreras-Astorga, A. and Schulze-Halberg, A. (2015b). On integral and differential representations of Jordan chains and the confluent supersymmetry algorithm. *J. Phys. A: Math. Theor.*, 48(31):315202.

Contreras-Astorga, A. and Schulze-Halberg, A. (2017). Recursive representation of wronskians in confluent supersymmetric quantum mechanics. *J. Phys. A: Math. Theor.*, 50(10):105301.

Correa, F., Jakubsky, V., and Plyushchay, M. S. (2015). PT-symmetric invisible defects and confluent Darboux-Crum transformations. *Phys. Rev. A*, 92:023839.

de Juan, F., Mañes, J. L., and Vozmediano, M. A. H. (2013). Gauge fields from strain in graphene. *Phys. Rev. B*, 87:165131.

Díaz-Bautista, E. (2020). Schrödinger-type 2d coherent states of magnetized uniaxially strained graphene. *J. Math. Phys.*, 61(10):102101.

Díaz-Bautista, E. and Fernández, D. J. (2017). Graphene coherent states. *Eur. Phys. J. Plus*, 132:499.

Díaz-Bautista, E., Negro, J., and Nieto, L. M. (2019). Partial coherent states in graphene. *J. Phys.: Conf. Ser.*, 1194:012025.

Dirac, P. A. M. (1958). *Priciples of Quantum Mechanics*. Oxford U.P., Oxford.

DiVincenzo, D. P. and Mele, E. J. (1984). Self-consistent effective-mass theory for intralayer screening in graphite intercalation compounds. *Phys. Rev. B*, 29:1685–1694.

Domínguez-Hernández, S. and Fernández C, D. J. (2011). Rosen–Morse potential and its supersymmetric partners. *Int. J. Theor. Phys.*, 50(7):1993–2001.

Dong, S. (2007). *Factorization Method in Quantum Mechanics*. Springer, Dordrecht.

Fernandez, D. J. (2010). Supersymmetric quantum mechanics. *AIP Conf. Proc.*, 1287:3.

Fernandez, D. J. (2019). Trends in supersymmetric quantum mechanics. *Integrability, Supersymmetry and Coherent States, CRM Series in Mathematical Physics, Springer, Cham*, page 37.

Fernandez, D. J. and Fernandez-Garcia, N. (2005). Higher-order supersymmetric quantum mechanics. *AIP Conf. Proc.*, 744:236.

Fernández C., D. J., García M., J. D., and O-Campa, D. (2020). Electron in bilayer graphene with magnetic fields leading to shape invariant potentials. *J. Phys. A: Math. Theor.*, 53(43):435202.

Fernández C, D. J. and Martínez-Moreno, D. I. (2020). Bilayer graphene coherent states. *Eur. Phys. J. Plus*, 135:739.

Fernández C, D. J. and Roy, B. (2020). Confluent second-order supersymmetric quantum mechanics and spectral design. *Phys. Scr.*, 95(5):055210.

Fernández C, D. J. and Salinas-Hernández, E. (2003). The confluent algorithm in second-order supersymmetric quantum mechanics. *J. Phys. A: Math. Gen.*, 36(10):2537–2543.

Fernández C., D. J. and Salinas-Hernández, E. (2005). Wronskian formula for confluent second-order supersymmetric quantum mechanics. *Phys. Lett. A*, 338(1):13 – 18.

Fernández C, D. J. and Salinas-Hernández, E. (2011). Hyperconfluent third-order supersymmetric quantum mechanics. *J. Phys. A: Math. Gen.*, 44(36):365302.

Fernández C., D. J. and González, J. (2015). Complex oscillator and Painlevé IV equation. *Ann. Phys.*, 359:213–229.

Ferreira, A., Viana-Gomes, J., Nilsson, J., Mucciolo, E. R., Peres, N. M. R., and Castro Neto, A. H. (2011). Unified description of the dc conductivity of monolayer and bilayer graphene at finite densities based on resonant scatterers. *Phys. Rev. B*, 83:165402.

Gangopadhyaya, A., Mallow, J., and Rasinariu, C. (2018). *Supersymmetric Quantum Mechanics*. World Scientific, Singapore, second edition.

Geim, A. and Grigorieva, I. (2013). Van der Waals heterostructures. *Nature*, 499:419–425.

Grandati, Y. and Quesne, C. (2015). Confluent chains of dbt: Enlarged shape invariance and new orthogonal polynomials. *SIGMA*, 11:061.

Gusynin, V. P. and Sharapov, S. G. (2005). Unconventional integer quantum Hall effect in graphene. *Phys. Rev. Lett.*, 95:146801.

Hecht, E. (2002). *Optics*. Pearson Education, USA, fourth edition.

Ince, E. L. (1956). *Ordinary Differential Equations*. Dover Publications, New York.

Infeld, L. and Hull, T. E. (1951). The factorization method. *Rev. Mod. Phys.*, 23:21–68.

Junker, G. (2019). *Supersymmetric Methods in Quantum, Statistical and Solid State Physics*. IOP Publishing Ltd, Bristol, second edition.

Katsnelson, M. (2011). *Graphene: carbon in two dimensions*. Cambridge University Press, Cambridge.

Kuru, S., Negro, J., and Nieto, L. M. (2009). Exact analytic solutions for a Dirac electron moving in graphene under magnetic fields. *J. Phys.: Condens. Matter*, 21:455305.

Le, D., Le, V., and Roy, P. (2018). Conditional electron confinement in graphene via smooth magnetic fields. *Physica E*, 96:17.

Masir, M. R., Vasilopoulos, P., and Peeters, F. M. (2011). Graphene in inhomogeneous magnetic fields: bound, quasi-bound and scattering states. *J. Phys.: Conden. Matter*, 23(31):315301.

Matulis, A., Peeters, F. M., and Vasilopoulos, P. (1994). Wave-vector-dependent tunneling through magnetic barriers. *Phys. Rev. Lett.*, 72:1518–1521.

McCann, E. and Koshino, M. (2013). The electronic properties of bilayer graphene. *Rep. Prog. Phys.*, 76:056503.

Midya, B. and Fernández, D. J. (2014). Dirac electron in graphene under supersymmetry generated magnetic fields. *J. Phys. A: Math. Theor.*, 47:285302.

Mielnik, B. (1984). Factorization method and new potentials with the oscillator spectrum. *J. Math. Phys.*, 25(12):3387–3389.

Mielnik, B., Nieto, L., and Rosas-Ortiz, O. (2000). The finite difference algorithm for higher order supersymmetry. *Phys. Lett. A*, 269(2-3):70–78.

Milpas, E., Torres, M., and Murguía, G. (2011). Magnetic field barriers in graphene: an analytically solvable model. *J. Phys.: Condens. Matter*, 23:245304.

Mostafazadeh, A. (2002a). Pseudo-hermiticity versus PT symmetry: The necessary condition for the reality of the spectrum of a non-hermitian hamiltonian. *J. Math. Phys.*, 43(1):205–214.

Mostafazadeh, A. (2002b). Pseudo-hermiticity versus PT-symmetry. II. A complete characterization of non-hermitian hamiltonians with a real spectrum. *J. Math. Phys.*, 43(5):2814–2816.

Naumis, G. G., Barraza-Lopez, S., Oliva-Leyva, M., and Terrones, H. (2017). Electronic and optical properties of strained graphene and other strained 2d materials: a review. *Rep. Prog. Phys.*, 80(9):096501.

Nieto, M. M. (1984). Relationship between supersymmetry and the inverse method in quantum mechanics. *Phys. Lett. B*, 145(3):208–210.

Novoselov, K. S., Geim, A. K., Morozov, S. V., Jiang, D., Katsnelson, M. I., Grigorieva, I. V., Dubonos, S. V., and Firsov, A. A. (2005). Two-dimensional gas of massless Dirac fermions in graphene. *Nature*, 438(7065):197–200.

Novoselov, K. S., Geim, A. K., Morozov, S. V., Jiang, D., Zhang, Y., Dubonos, S. V., Grigorieva, I. V., and Firsov, A. A. (2004). Electric field effect in atomically thin carbon films. *Science*, 306(5696):666–669.

Oliva-Leyva, M. and Naumis, G. G. (2015). Generalizing the fermi velocity of strained graphene from uniform to nonuniform strain. *Phys. Lett. A*, 379(40):2645 – 2651.

Peng, X., Zhou, H., Wei, B. B., Cui, J., Du, J., and Liu, R.-B. (2015). Experimental observation of Lee-Yang zeros. *Phys. Rev. Lett.*, 114:010601.

Ramezani Masir, M., Vasilopoulos, P., Matulis, A., and Peeters, F. M. (2008). Direction-dependent tunneling through nanostructured magnetic barriers in graphene. *Phys. Rev. B*, 77:235443.

Raza, H. (2012). *Graphene Nanoelectronics: Metrology, Synthesis, Properties and Applications*. Springer-Verlag, Berlin, first edition.

Razado-Colambo, I., Avila, J., Vignaud, D., Godey, S., Wallart, X., Woodruff, D., and Asensio, M. (2018). Structural determination of bilayer graphene on sic(0001) using synchrotron radiation photoelectron diffraction. *Sci. Rep.*, 8(10190).

Ruess, G. and Vogt, F. (1948). Höchstlamellarer kohlenstoff aus graphitoxyhydroxyd. *Monatshefte für Chemie und verwandte Teile anderer Wissenschaften*, 78(1434-4475):222–242.

Saito, R., Dresselhaus, G., and Dresselhaus, M. (1998). *Physical Properties of Carbon Nanotubes*. Imperial College Press, London, first edition.

Saito, R., Fujita, M., Dresselhaus, G., and Dresselhaus, M. S. (1992). Electronic structure of graphene tubules based on c_{60}. *Phys. Rev. B*, 46:1804–1811.

Sakurai, J. J. (1994). *Modern quantum mechanics; rev. ed.* Addison-Wesley, Reading, MA.

Samsonov, B. (1999). New possibilities for supersymmetry breakdown in quantum mechanics and second-order irreducible Darboux transformations. *Phys. Lett. A*, 263:274.

Sandhya, R., Ranjani, S. S., and Kapoor, A. (2015). Shape invariant potentials in higher dimensions. *Ann. Phys.*, 359:125.

Schnez, S., Molitor, F., Stampfer, C., Güttinger, J., Shorubalko, I., Ihn, T., and Ensslin, K. (2009). Observation of excited states in a graphene quantum dot. *App. Phys. Lett.*, 94(1):012107.

Schrödinger, E. (1940). Further studies on solving eigenvalue problems by factorization. *Proc. R. Irish Acad. A: Math. Phys. Sc.*, 46(00358975):183–206.

Schrödinger, E. (1941). The factorization of the hypergeometric equation. *Proc. R. Irish Acad. A: Math. Phys. Sc.*, 47:53–54.

Schulze-Halberg, A. and Roy, P. (2017). Construction of zero-energy states in graphene through the supersymmetry formalism. *J. Phys. A: Math. Theor.*, 50(36):365205.

Schulze-Halberg, A. and Yesiltas, O. (2018). The generalized confluent supersymmetry algorithm: Representations and integral formulas. *J. Math. Phys.*, 59(4):043508.

Schütt, M., Ostrovsky, P. M., Gornyi, I. V., and Mirlin, A. D. (2011). Coulomb interaction in graphene: Relaxation rates and transport. *Phys. Rev. B*, 83:155441.

Semenoff, G. W. (1984). Condensed-matter simulation of a three-dimensional anomaly. *Phys. Rev. Lett.*, 53:2449–2452.

Sukumar, C. V. (1985). Supersymmetric quantum mechanics and the inverse scattering method. *J. Phys. A: Math. Gen.*, 18(15):2937–2955.

Sukumar, C. V. (1985a). Supersymmetric quantum mechanics of one-dimensional systems. *J. Phys. A: Math. Gen.*, 18(15):2917–2936.

Sukumar, C. V. (1985b). Supersymmetry, factorisation of the Schrödinger equation and a hamiltonian hierarchy. *J. Phys. A: Math. Gen.*, 18(2):L57–L61.

Sukumar, C. V. (1986). Supersymmetry, potentials with bound states at arbitrary energies and multi-soliton configurations. *J. Phys. A: Math. Gen.*, 19(12):2297–2316.

Sukumar, C. V. (1987). Supersymmetry and potentials with bound states at arbitrary energies II. *J. Phys. A: Math. Gen.*, 20(9):2461–2481.

Wallace, P. R. (1947). The band theory of graphite. *Phys. Rev.*, 71:622–634.

Wang, S., Yata, S., Nagano, J., Okano, Y., Kinoshita, H., Kikuta, H., and Yamabe, T. (2000). A new carbonaceous material with large capacity and high efficiency for rechargeable li-ion batteries. *J. Electrochem. Soc.*, 147(7):2498.

Wang, X., Chen, Y. P., and Nolte, D. D. (2008). Strong anomalous optical dispersion of graphene: complex refractive index measured by picometrology. *Opt. Express*, 16(26):22105–22112.

Witten, E. (1981). Dynamical breaking of supersymmetry. *Nucl. Phys. B*, 188(3):513–554.

Wu, S., Killi, M., and Paramekanti, A. (2012). Graphene under spatially varying external potentials: Landau levels, magnetotransport, and topological modes. *Phys. Rev. B*, 85:195404.

Zhang, Y., Tan, Y. W., and Stormer, H. L. (2005). Experimental observation of the quantum Hall effect and Berry's phase in graphene. *Nature*, 438(7065):201–204.